UNIVERSIDADE FEDERAL DE SÃO CARLOS
CENTRO DE CIÊNCIAS EXATAS E DE TECNOLOGIA
PROGRAMA DE PÓS-GRADUAÇÃO EM CIÊNCIA E ENGENHARIA DE MATERIAIS

ANALYSIS OF CRACK PROPAGATION IN THE WEDGE SPLITTING TEST VIA DIGITAL IMAGE CORRELATION AND FINITE ELEMENT ANALYSES

Rafael Vargas Maginador

São Carlos
2019

UNIVERSIDADE FEDERAL DE SÃO CARLOS
CENTRO DE CIÊNCIAS EXATAS E DE TECNOLOGIA
PROGRAMA DE PÓS-GRADUAÇÃO EM CIÊNCIA E ENGENHARIA DE MATERIAIS

ANALYSIS OF CRACK PROPAGATION IN THE WEDGE SPLITTING TEST VIA DIGITAL IMAGE CORRELATION AND FINITE ELEMENT ANALYSES

Rafael Vargas Maginador

Dissertação apresentada ao Programa de Pós-Graduação em Ciência e Engenharia de Materiais como requisito parcial à obtenção do título de MESTRE EM CIÊNCIA E ENGENHARIA DE MATERIAIS

Orientador: Dr. Rodrigo Bresciani Canto
Coorientador: Dr. José de Anchieta Rodrigues
Agência Financiadora: Fapesp - Processo: 2017/05678-6

São Carlos
2019

VITAE DO CANDIDATO

Bacharel em Engenharia de Materiais pela UFSCar (2016).

UNIVERSIDADE FEDERAL DE SÃO CARLOS

Centro de Ciências Exatas e de Tecnologia
Programa de Pós-Graduação em Ciência e Engenharia de Materiais

Folha de Aprovação

Assinaturas dos membros da comissão examinadora que avaliou e aprovou a Defesa de Dissertação de Mestrado do candidato Rafael Vargas Maginador, realizada em 19/02/2019:

Prof. Dr. Rodrigo Bresciani Canto
UFSCar

Prof. Dr. Marco Aurelio Liutheviciene Cordeiro
UFSCar

Prof. Dr. François Hild
CNRS

Prof. Dr. Ricardo Afonso Angélico
USP

ACKNOWLEDGMENTS

I would like to thank CNPq that funded the very beginning of this Master's project (grant #132573/2017-2) and FAPESP for funding the most of it (grant #2017/05678-6, São Paulo Research Foundation (FAPESP)[1]), even allowing an enriching internship abroad (grant #2017/20911-9). This study was financed in part by the Coordenação de Aperfeiçoamento de Pessoal de Nível Superior - Brasil (CAPES) - Finance Code 001.

I am especially grateful to Anchieta, Rodrigo, François, and Jan. The amount I learned with each of them, scientifically and for my personal growth, surpasses any expectation that I could have before this project.

This work would not be possible without the friends from the research group, that collaborated on the daily struggles and learning in the lab, and that shared their knowledge and experience, always in a positive mood that allowed us to grow as a team.

My gratitude to all the friends and familiars that directly or indirectly helped me to remain on the right path, with a word of wisdom or an incentive when I needed the most.

A special thanks must be directed to my grandmother that always prioritized education in the family, and to my mother and sister that were always present and supportive in the everyday challenges throughout this whole time.

At last, I am grateful to my fiancee Dani, for believing in my potential, understanding the non-linear path of the academic career, and always supporting me with care and love.

[1] As opiniões, hipóteses e conclusões ou recomendações expressas neste material são de responsabilidade do autor e não necessariamente refletem a visão da FAPESP.

ABSTRACT

Castable refractories are applied in dangerous environments in which it is unpractical to avoid crack initiation. Therefore, their microstructure is usually complex in order to hinder crack propagation by toughening mechanisms. One way to quantify such mechanisms is calculating the work of fracture via the so-called Wedge Splitting Test (WST), which allows for stable crack growth. However, this method is experimentally laborious and the usual result is only one parameter per test. The stability of the propagating crack leads to opportunities for additional analyses to better understand the fracture process. The present work focuses on extracting more information from one single WST. Parameters relevant to linear elastic fracture mechanics (*i.e.,* crack tip positions during the propagation, stress intensity factors, and T-stress) and insight into the Fracture Process Zone (FPZ) described by various cohesive zone models were sought as well. Three different numerical methodologies are compared on the same experiment, namely integrated digital image correlation, and two finite element model updating methods. The first one uses analytical fields accounting for the presence of a crack in an elastic medium. The second and third ones consist in updating finite element models using cost functions on the displacement fields and on the experimental force, respectively. Slightly different crack tip positions were found by the three methods. Stress intensity factors and T-stresses were also calculated. Using cohesive elements, it was possible to further analyze the FPZ length, which was found not to be fully developed in the test studied herein. This result proves that the examined material has the ability of bridging rather long cracks.

Keywords: wedge splitting test; digital image correlation; finite element model updating; crack propagation; cohesive elements; fracture process zone

RESUMO

Análise da propagação de trincas no método da cunha via correlação de imagens digitais e análise de elementos finitos

Concretos refratários são utilizados em ambientes com alta periculosidade nos quais é inviável impedir a iniciação de trincas. No entanto, sua microestrutura é usualmente complexa de forma a dificultar a propagação de trincas por mecanismos de tenacificação. Uma maneira de quantificá-los é calculando a energia de fratura através do método da cunha, que permite uma propagação estável de trincas. Entretanto, este método é trabalhoso e geralmente resulta em apenas um parâmetro por teste. A estabilidade da propagação da trinca permite análises adicionais para melhor compreensão do processo de fratura. O foco do presente trabalho é na extração de mais informações de um único teste pelo método da cunha. Parâmetros relevantes para a mecânica da fratura linear elástica (*i.e.,* posição da ponta da trinca durante a propagação, fatores de intensidade de tensão e a tensão T) e uma melhor compreensão sobre a região de processo de fratura descrita por vários modelos de zona coesiva também foram investigados. Três diferentes metodologias numéricas são comparadas para o mesmo experimento, sendo elas a correlação de imagens integrada, e dois métodos de atualização de modelo de elementos finitos. A primeira usa campos analíticos que consideram a presença de uma trinca em um meio elástico. A segunda e a terceira consistem na atualização de modelos de elementos finitos com funções erro baseadas nos campos de deslocamentos e na carga medida no experimento, respectivamente. Posições de ponta de trinca ligeiramente diferentes foram encontradas pelos três métodos. Fatores de intensidade de tensões e tensões T também foram calculadas. O uso de elementos coesivos permitiu uma análise sobre o tamanho da região do processo de fratura, o qual não estava totalmente desenvolvido no experimento aqui analisado. Este resultado prova que o material examinado tem a habilidade de tenacificação pelo mecanismo de *bridging* e com trincas consideravelmente longas.

Palavras-chave: método da cunha; correlação de imagens digitais; atualização de modelo de elementos finitos; elementos coesivos; zona do processo de fratura

PUBLICATIONS

VARGAS, R.; RODRIGUES, J. A.; CANTO, R. B.; NEGGERS, J.; HILD, F.
On the importance of analyses of two opposite faces for wedge splitting tests with DIC. In: 10th European Solid Mechanics Conference (ESMC2018). Bologna, Italy; 2018, p.53.

VARGAS, R.; NEGGERS, J.; CANTO, R. B.; RODRIGUES, J. A.; HILD, F.
Comparison of two full-field identification methods for the wedge splitting test on a refractory. In: Journal of the European Ceramic Society 2018; 38(16):5569–5579.
DOI: `https://doi.org/10.1016/j.jeurceramsoc.2018.07.039`

VARGAS, R.; NEGGERS, J.; CANTO, R. B.; RODRIGUES, J. A.; HILD, F.
Analysis of a castable refractory using the wedge splitting test and cohesive zone model. In: Journal of the European Ceramic Society 2019; 39(13):3903–3914.
DOI: `https://doi.org/10.1016/j.jeurceramsoc.2019.03.009`

x

CONTENTS

LIST OF TABLES

LIST OF FIGURES

LIST OF ABREVIATIONS

AZS - Alumina-Zirconia-Silica

BLTS - Bi-Linear Traction Separation law for cohesive elements

CDP - Concrete Damaged Plasticity law, built-in Abaqus™

CZM - Cohesive Zone Model

DIC - Digital Image Correlation

FE - Finite Element

FEM - Finite Element Method

FEMU - Finite Element Model Updating

FEMU-F - Finite Element Model Updating based on load measurements

FEMU-U - Finite Element Model Updating based on displacement measurements

FPZ - Fracture Process Zone

I-DIC - Integrated Digital Image Correlation

LEFM - Linear Elastic Fracture Mechanics

PPR - Park-Paulino-Roesler model

ROI - Region of Interest

SIF - Stress Intensity Factor

T3-DIC - Digital Image Correlation performed with three-noded triangular elements

TS - T-stress, a stress parallel to the crack front

WST - Wedge Splitting Test

LIST OF SYMBOLS

A - Surface area of the crack

BC_c - Parameter related to a correction of the Boundary Condition in FEMU-F

c - Crack length

d - Crack tip shift estimation

E - Young's modulus

f - Image of the reference configuration

F_c - Calculated reaction forces

F_h - Horizontal force

F_m - Measured experimental forces

F_v - Vertical force

g - Image of the deformed configuration

G_c - Critical energy release rate for brittle fracture (fracture energy)

$\{\mathbf{h}\}$ - Right hand member for the identification method in FEMU-F

$[\mathbf{H}]$ - Hessian matrix for the identification method in FEMU-F

J_c - Fracture energy for the cohesive models

K_I - Stress Intensity Factor in mode I loading (opening)

K_{Ic} - Critical Stress Intensity Factor in mode I loading (opening)

K_{II} - Stress Intensity Factor in mode II loading (in-plane shear)

K_{IR} - Critical Stress Intensity Factor in mode I loading, function of the crack length

n_t - Number of time steps

$\{\mathbf{p}\}$ - Column vector with the materials parameters in FEMU-F methodology

$\{\mathbf{p_0}\}$ - Column vector with the initial materials parameters in FEMU-F methodology

p_i - Truncation for the first term used in Williams Series

p_f - Truncation for the last term used in Williams Series

r - distance from the crack tip (used in I-DIC)

R - Crack propagation resistance

S_F - Load sensitivity used in FEMU-F

t - Time steps

$\mathbf{u}$ - Displacement vector

U_m - Elastic energy stored in the testing machine

U_s - Elastic energy stored in the specimen

V_d - Function to correct vector directions in Williams Series

W - Total work performed by the testing machine

$\mathbf{x}$ - Arbitrary position in the specimen

Y - Geometric factor

$\mathbf{z}$ - Vector in the complex plane

α - Wedge angle

γ_{wof} - Work of fracture

Δh - Vertical actuator displacement

$\Delta\delta$ - Splitting displacement averaged in both faces of the sample

θ - Angular position

κ - Dimensionless parameter dependent on Poisson's ratio

μ - Lamé's modulus

ν - Poisson's ratio

ν_i - Amplitude for the chosen fields $\mathbf{\Psi}_i$

σ - Remote stress

σ_c - Critical remote stress

σ_F - Standard load uncertainty

σ_{max} - Cohesive strength for the cohesive models

σ_R - Critical remote stress during stable crack propagation

ϕ - Error minimized for measuring displacement fields by Digital Image Correlation

ϕ_u - Displacement error minimized in the FEMU-U case

χ_F - Normalized cost function using forces for FEMU-F

$\boldsymbol{\psi}_n^j$ - Vector fields for the Williams Series

$\mathbf{\Psi}_i$ - Chosen fields to parameterize the displacement field

ω_n^j - Amplitudes used in Williams Series

1 INTRODUCTION

Castable refractories are utilized for the production of steel, glass and oil derivatives, among others. They are found as coatings and as lining in containers for many transformation processes, especially when high temperatures and corrosive environments are involved. Optimizing these materials may not only diminish their application and maintenance costs, but also improve their efficiency and lifetime. This would lead to smaller energetic consumption, and economic, environmental and social gains by reducing the risks involved.

The high temperatures involved and many variables of these processes highlight the importance of understanding the mechanisms that drive the fracture of these materials. This knowledge allows the development of new compositions and microstructures along with supporting the proper material selection for given applications.

Many standardized tests (*e.g.,* 3 or 4-point bending tests, with and without notch) may be used to obtain important properties of these materials such as resistance and damage by thermal shocks, fracture energy and strength [1]. However, all these experiments often yield only a few data per test. As another example, the Wedge Splitting Test (WST) is mostly used to evaluate solely the fracture energy of castable refractories [2]. Such technique is usually applied to relatively voluminous specimens, and its setup may be laborious. If more information could be extracted from every single WST, not only an improved analysis would be possible but also the time and resources spent on it would become more profitable.

Part of this challenge is addressed herein thanks to full-field measurements instead of point data, by using Digital Image Correlation (DIC). This measurement technique allows localized phenomena to be quantified, *e.g.,* crack wake effects and the fracture process zone on crack propagation in concrete-like materials, which would hardly be visible and quantifiable by other techniques [3]. Another selected tool is numerical simulations of this test using the Finite Element Method (FEM). By using comercial codes (*e.g.,* Abaqus™), analyses with cohesive zone models are possible. Furthermore, these techniques may be coupled, using DIC to validate FE results or as input Boundary Conditions (BC) for the Finite Element (FE) models.

In the work presented hereafter, three different techniques, namely integrated-DIC, FE analyses and Finite Element Model Updating (FEMU), are applied to the same WST. The main goal of this Master thesis is to compare what can be obtained with each methodology and to discuss its advantages and disadvantages, providing which information and insight each of them brings about the fracture process in the material.

2 BIBLIOGRAPHIC REVIEW

2.1 Castable refractories

Castable refractories are ceramics utilized for the fabrication of materials under high temperatures. In general, they are composed of big aggregates bonded by a fine (usually porous) matrix. Their main usage is as coatings of furnaces, cauldrons, and containers that are directly in contact with corrosive elements at high temperatures. For this application to be possible, these materials should retain their needed properties (*e.g.,* mechanical, chemical, physical) in acceptable levels even in these aggressive environments. Among all refractories, castable refractories are classified as monolithic, since a pre-form is not necessary (*e.g.,* brick shape). This allows for a faster, easier and cheaper installation, and also guarantees fewer joints susceptible to corrosion [4].

The raw material components (*i.e.,* aggregates, matrix components, binders) are selected in order to obtain adequate phases and microstructure for the desired application. One should also consider the material processing route, which may be affected if the raw material is changed. In this way, the distribution of sizes and average diameters of particles, the additives, and their actions, such as chemical reactions and related kinetics, become crucial for the understanding and development of new materials [5]. The development of castable refractories is intimately coupled with the demand for oil, glass and base material (*e.g.,* steel, metal and other alloys) industries. Thus, new ways to improve process efficiency, equipment lifetime and predictability of failures are addressed since the beginning of the 20-th century given the high risks involved in these processes [6].

Some important findings in that area are the increased refractoriness with the alumina content, as can be deduced from the binary phase diagram Al_2O_3-SiO_2, and also the improvement of analysis techniques such as Scanning Electron Microscopy (SEM), which helped for the understanding of the microstructure of these materials. New materials were also developed aiming to improve refractory properties [7]. An important example is the AZS (Alumina-Zirconia-Silica or Al_2O_3-ZrO_2-SiO_2) case, in which the eutectic composition leads to a specific microstructure shown in Figure 2.1. The AZS system brought significant gains

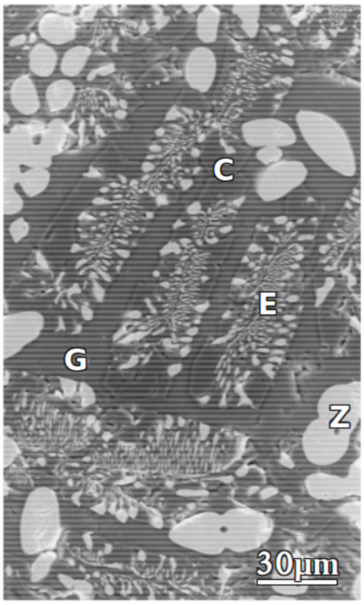

Figure 2.1: SEM image of an AZS microstructure obtained by melting. In the image, E denotes Alumina-Zirconia with eutectic structure, C for corundum (an Al_2O_3 phase), Z for zirconia dendrites, and G an aluminosilicate glass that contains Zirconia. Adapted from Ref. [7].

for glass industries by diminishing the corrosion of containers in which glass is molten. Another point to be considered is the need for different refractories in the same application. Depending on the step of the process, different thermochemical loadings occur. The understanding of the material properties is needed for the correct selection and application of refractories [7].

The ongoing search for innovation by industries to distinguish themselves in the market also spurs the development of non-conventional materials. For example, there are studies about the usage of nanomaterials or the assembly of composites with new (or little-explored) combinations of raw materials and processing. The high superficial area in nanoparticles guarantees higher reactivity, which may facilitate chemical reactions to occur at lower temperatures, for instance, increasing the energy efficiency of the process [5]. Another source of innovation is the mimicking of natural microstructures [8]. An important example is the laboratory production of microstructures that may increase to even one order of magnitude the toughness of the composite when compared to the raw materials [9], which are based on synergistic mechanisms observed in nacre.

2.2 Mechanical properties of ceramics

Some general and important properties of ceramic materials are their high resistance to abrasion, high refractoriness, high hardness and Young's modulus, low thermal conductivity, thermal and chemical stability, among others [10, 11]. These properties are related to their strong atomic bonds, predominantly iono-covalent and to their crystalline structure, even if their atomic packing is less dense than metals. The lower packing of ceramic crystals leads to a high activation energy for dislocation motions, and to the presence of few sliding planes, which explains the brittle behavior, usually with the absence of plasticity at room temperature. The complexity of the atomic packing leads to amorphization after melting and cooling, and thus other processing routes are needed for producing crystalline ceramics. The processing of castables, as discussed in this dissertation, brings inherent porosity and the presence of aggregates in the final microstructure.

The brittle fracture of these materials makes it necessary to fully understand their mechanical behavior, due to the possibility of catastrophic failure (*e.g.,* to avoid accidents). The lifetime of equipments may be augmented by engineering the microstructure in order to minimize crack propagation caused by thermal shocks, which also diminishes randomness about various properties, reducing costs and risks for such applications.

The porosity, heterogeneities and microcracks can be considered as defects in a homogeneous material. In such approach, the Linear Elastic Fracture Mechanics (LEFM) provides a framework for such analysis. When analyzing different loading conditions, it is common practice to consider a "mode," mode I is related to opening, mode II to in-plane shear, and mode III to tearing (*i.e.,* out-of-plane shear). For a crack propagation analysis, the most important condition is mode I (although mixed-mode occurs), since it opens the crack faces, and therefore the energy is used to create more cracked surfaces, while mode II and III loadings may dissipate energy through friction instead of opening the crack [12].

Let us consider a sharp defect of size $2c$ in a very thin plate, which will be considered as an infinite medium in 2D. If it is loaded in every direction, the stresses at the defect tip will be very high, but very difficult to calculate since closed-form expressions exhibit discontinuities and singularities [12]. If only the opening load is considered, we can define the Stress Intensity Factor (SIF) in mode I, K_I, as

$$K_I = \sigma Y \sqrt{c} \tag{2.1}$$

where σ is the remotely applied stress, and Y a geometric factor. The K_I SIF relates the size of the defect with the applied stresses, and consequently, for brittle materials it is hard to define a single maximum tensile stress (since c is a random variable). However, for a given defect size, we can define the critical condition

$$K_{Ic} = \sigma_c Y \sqrt{c} \tag{2.2}$$

where σ_c is the remote stress at failure, and K_{Ic} a material property, the critical SIF in mode I for a crack to propagate catastrophically, also known as fracture toughness.

The investigation of tests with stable crack propagation is useful to better understand the mechanisms of fracture and quantify relevant mechanical parameters. Let us consider a system with the testing machine and the specimen for the wedge splitting test (WST), W denotes the total work. For quasi-static propagation, the stability condition for stable crack growth is given by

$$-\frac{d}{dA}(U_s + U_m) \leq \frac{dW}{dA} \tag{2.3}$$

where A is the surface area created by the crack, U_s the elastic energy stored in the specimen, and U_m the elastic energy stored in the testing machine [13]. Equation (2.3) may be interpreted as the need for the release of the stored elastic energy of the system be less than the derivative of the dissipated energy related to the creation of new surfaces in order to achieve stable propagation. When this inequality is not satisfied, crack propagation will be accompanied by a sudden release of elastic energy that will cause catastrophic failure.

Two main mechanisms may lead to an increase of the energy consumption for the crack to propagate in castable refractories [14], which can mitigate issues associated with catastrophic failures. The first is known as crack deflection and occurs when part of the energy is dissipated by changes in the direction of the propagation caused by material heterogeneities. The second is called crack tip shielding, which occurs when compressive stresses are induced in the vicinity of the crack tip, thereby hindering propagation. The shielding mechanism may occur because of microcracks, phase changes (*e.g.,* presence of non-stabilized Zirconia in Alumina matrices), bridging between aggregates and the matrix, glassy phases between two crack surfaces, and ramifications. Some of these mechanisms are schematically represented in Figure 2.2.

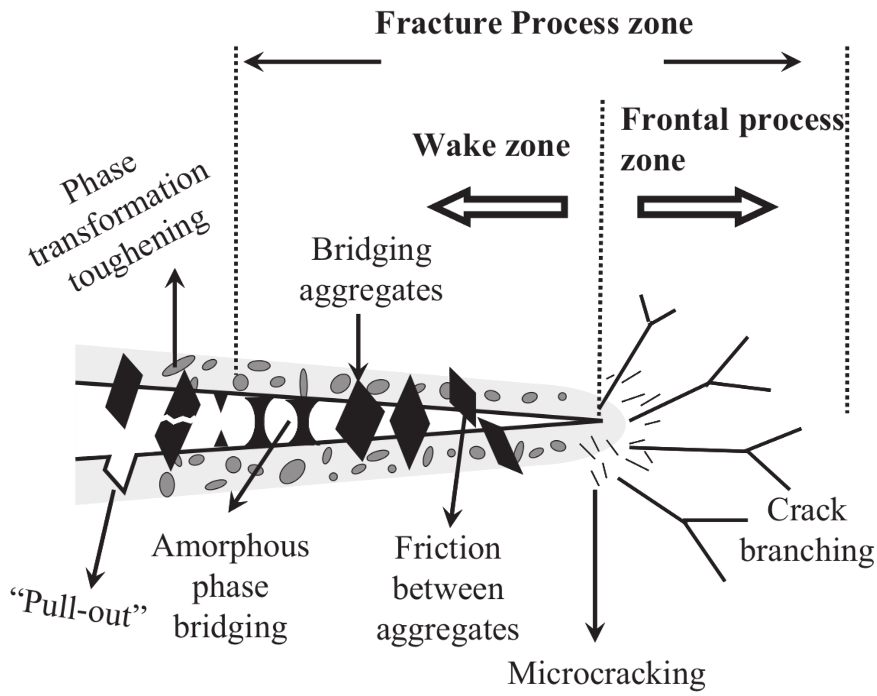

Figure 2.2: Some possible toughening mechanisms for fracture in castable refractories. Adapted from Ref. [15].

Measuring SIFs for different crack lengths is one way to quantify the effect of such mechanisms. Considering a stable crack propagation, the change of SIF as a function of the increase of the crack length shows how much the stress must be intensified to continue the propagation. In such cases, the fracture toughness is not constant and K_{IR} should be considered, as the mode I SIF now depends on the defect (or crack) length. This effect is known as the R-curve behavior and is commonly used to quantify fracture mechanisms [16–19]. It also allows one to compare compositions [20] and to check the toughness of newly developed microstructures [21]. Once these toughening mechanisms are well understood, insight into how to develop new materials are provided in order to create outstanding materials with high strength and toughness [22–25]. It is especially important to quantify the toughness of materials related to crack propagation instead of their initiation [9]. In general, the difficulty of determining the R-curve for castable refractories is related to achieving a stable propagation due to its inherent brittleness.

One of the usual ways of obtaining the R-curve, which means how much energy is dissipated for each increment of crack propagation, consists in applying the theory of the Linear Elastic Fracture Mechanics (LEFM) onto standardized tests. In this case, K_{IR}, is given by

$$K_{IR}(c) = \sigma_R(c) Y \sqrt{c} \tag{2.4}$$

which is similar to Equation (2.1), but with a dependence on the defect size, and where σ_R is the remote stress applied during propagation. For a plane strain state (as in WSTs), the fracture toughness K_{Ic} is related to the fracture energy

$$K_{Ic} = \sqrt{\frac{E\mathcal{G}_c}{1-\nu^2}} \tag{2.5}$$

where E is the Young's modulus, $\mathcal{G}_c$ the fracture energy, and ν the Poisson's ratio. In a stable crack propagation regime, the crack propagation resistance, R, takes the same value of $\mathcal{G}_c$ during its propagation. Therefore, using Equations (2.4) and (2.5)

$$R = \frac{K_{IR}^2(c)(1-\nu^2)}{E} = \frac{\sigma_R^2(c) Y^2 (1-\nu^2) c}{E}. \tag{2.6}$$

By using Equation (2.6), it is possible to evaluate the R-curve during any test for which stable propagation occurs. Expressions of Y are known for simple geometries [26, 27] such as 3-point bend tests (although it is difficult to achieve stable propagation in this case). For cases like the WST, the configuration complicates this expression. Attempts and proposals to solve or simplify the analysis were made, for example by Guinea et al. [28], in which a binary approach with intact material or fully separated parts was used for the WST to numerically calculate the SIFs, and obtain Y with an inverse analysis. By this approach, using a single-parameter (K_I) analysis is insufficient for application in many cases of quasi-brittle fracture [29], and higher order terms must be used [30, 31].

2.3 Wedge Splitting Test

The Wedge Splitting Test (WST) is a mechanical test performed to obtain stable crack propagation (*i.e.,* a smooth softening of the load after its peak was reached) even for brittle materials such as castable refractories [2]. It allows the calculation of the work of fracture γ_{wof} of the material, which is dissipated by creating new surfaces, thus avoiding that much of the stored energy be dissipated in other forms like heat or sound waves. Introduced in the 1990s [2, 32, 33], it is based on the idea of decreasing the elastic energy stored in the testing machine by a wedge and rollers, as schematically drawn in Figure 2.3, which transmit the vertically applied force, F_v, as a horizontal (splitting) loading of the specimen, F_h, in a mode I (opening) regime. The horizontal force is related to the vertical load

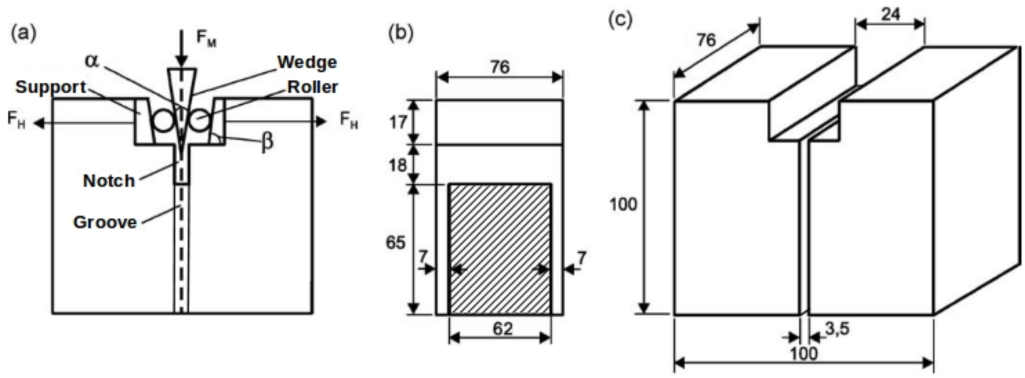

Figure 2.3: Geometry used in the WST. (a) Frontal view with schematic of the parts used in the test. (b) Transverse section passing through the surface in which the crack propagates. (c) Isometric view with typical dimensions of the specimen. Adapted from Ref. [34].

by

$$F_h = \frac{F_v}{2\tan\alpha} \tag{2.7}$$

where α denotes the angle of the wedge, usually varying between 10 and 15°. Once α becomes less than 5°, experimental difficulties arise. Conversely, a much higher α value is less effective for stability purposes [2].

In this test, control must be performed through the actuator displacement or, preferably, by extensometers measuring the crack mouth opening displacement [2]. In the case of a force control mode, the test would only be possible until the maximum load. One of the greatest advantages of extensometry consists in measurements made directly on the specimen, not considering the compliance of the testing machine. However, if the surface of the crack propagation remains free for observation, one may follow crack propagation with optical techniques for visual analyses with a lens or any suitable full-field measurement technique.

The main goal of the WST is to calculate the work of fracture or the fracture energy as discussed above. The global curve F_v vs. actuator displacement is integrated through the whole test, and the energy obtained is then divided by the projected crack propagation area to obtain the work of fracture. This approach presents uncertainties since the elastic energy stored in the testing machine is considered. This value of γ_{wof} can be used as an upper bound for the real γ_{wof} [35]. When extensometry is used (or DIC, for instance), it is more precise to integrate the splitting F_h vs. notch opening to evaluate the work applied forces to the specimen.

The geometry used in the WST is especially suitable for materials such as castable refractories with big aggregates, due to its high ratio between the fractured area and the volume of the specimen, thereby increasing the representativity of the results. To ensure that the crack is maintained in the central plane, grooves can be cut on the two opposite faces of the specimen (Figures 2.3) to guide its propagation. Another advantage is the possibility of producing the specimen in the different geometries shown in Figure 2.4, in which Figure 2.4(a), used in this project, is especially useful for molded castables, while Figures 2.4(b-c) show specimens that can be easily drilled out of real structures, and Figure 2.4(d) shows that the test can be made with any geometry, as long as it is possible to create the pre-crack.

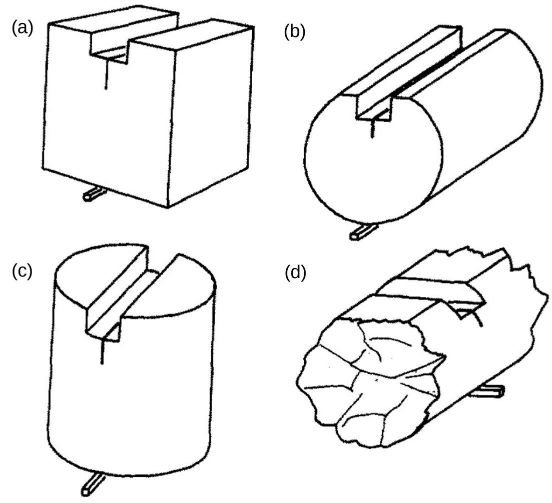

Figure 2.4: Possible geometries for the WST. Adapted from Ref. [14].

More details on the specimen geometry and involved parts (*e.g.,* rollers, blocks, wedge) can be found in Ref. [36]. The correlations between processing temperatures and obtained microstructures with the material properties (*e.g.,* maximum force, fracture energy) measured by the WST are discussed by Ribeiro and Rodrigues [34].

2.4 Digital Image Correlation

The measurement technique known as DIC has been used successfully to analyze crack propagation [37–41]. It consists in using images to measure the motion of points of the specimen, which can occur, for instance, as the result of a mechanical loading [42]. These images can be 2D or 3D, and the scale of the displacements depends on the acquisition device, which allows the pixel (or voxel) to represent physical dimensions ranging from a few nanometers to some kilometers [43]. The growth of DIC popularity is associated not only with the development of image acquisition devices with ever-increasing resolutions and more accessible prices, but also to the constant development of DIC algorithms and to the possibility of full-field measurements (*i.e.,* displacements) instead of point-data like conventional extensometry.

Considering a 2D case, f is the image of the reference configuration, and g of the deformed specimen, both in gray levels. In the absence of acquisition noise, the gray level conservation reads

$$f(\mathbf{x}) = g(\mathbf{x} + \mathbf{u}(\mathbf{x})) \tag{2.8}$$

once that the gray level of any material point $\mathbf{x}$ [1] of f inside the Region Of Interest (ROI) will be equal to the gray level of the same material point in g, but now will be located at $\mathbf{x}+\mathbf{u}(\mathbf{x})$, where $\mathbf{u}$ is the displacement vector of this point. An exact correlation of the gray levels is not feasible since acquisition noise is always present. To deal with such noise, the sum of the quadratic differences is minimized in the ROI

$$\phi = \sum_{ROI} (f(\mathbf{x}) - g(\mathbf{x} + \mathbf{u}(\mathbf{x})))^2 \tag{2.9}$$

with respect to the chosen parameterization of the displacement field. This approach is optimal for a white, Gaussian and homogeneous noise [43].

Since one pixel has only one gray level value, trying to measure its displacements in two directions is an ill-posed problem by itself, *i.e.,* with no guarantee of a unique solution since many pixels may present the same brightness, even without considering the contribution of noise. This problem is commonly solved by using discretizations that add constraints to the system to better condition it. In this case, the constraint is chosen as a way to express how a group of pixels should move together, instead of letting their displacements free.

The parameterized displacement field with a finite number of field $\mathbf{\Psi}_i$ with unknown amplitudes υ_i reads

$$\mathbf{u}(\mathbf{x}) = \sum_i \upsilon_i \mathbf{\Psi}_i(\mathbf{x}) \tag{2.10}$$

so that ϕ now depends on the column vector $\{\boldsymbol{\upsilon}\}$ gathering all amplitudes υ_i. Without previous knowledge of the system kinematics, the best alternative is choosing a robust $\mathbf{\Psi}_i$ that works for the majority of the cases like a finite element discretization [44]. In this work, T3-DIC is used with three-noded triangle elements with linear interpolations [45, 46].

[1] Vectors are in bold. In this way, $\mathbf{x}$ represents the coordinates (x_1,x_2), for instance.

It is also possible to improve this choice disconnecting nodes of the finite element mesh when the crack path is known (*e.g.,* by the DIC residual [46]), choosing enriched kinematics [47], or choosing closed-form solutions for the test [48] in which υ_i provide directly the desired mechanical parameters instead of nodal displacements. In an elastic loading with the presence of a crack, the fields $\mathbf{\Psi}_i$ have known solutions for plane stress or strain cases. When they are used directly in so-called Integrated-DIC (I-DIC [40, 48, 49]), it is not necessary to post-process displacement fields in order to obtain fracture mechanics parameters (*e.g.,* crack tip position, K_I, K_{II}, T-stress [2]).

2.5 Finite Element Method

Many engineering problems like stress analyses, heat transfer, magnetic fluxes or fluid mechanics can be described with partial differential equations, which many times do not present simple (or even possible) closed-form solutions. The FEM is a numerical methodology that allows the approximate solution to these equations to be computed robustly and allowing analyses or complex geometries [50].

The basic idea of the FEM is dividing the geometry into generally small elements connected by nodes, as exemplified in Figure 2.5. The physical problem is then decomposed in a linear system of equations with the number of unknowns equal to the degrees of freedom, which result in approximations of the desired variable (*e.g.,* temperature in a thermal analysis, or applied force in a mechanical problem) in the nodal positions. Computers are generally used since the precision of results tends to increase with the number of nodes, and usually hundred of thousands or even hundreds of millions of nodes are used in engineering analyzes [50].

The FEM was developed in the aerospace industry in the fifties, and the paper by Turner et al. [51] is considered one starting point. An interesting point of view about the beginning of its development and the context of that time can be read in Clough [52], from the same author that introduced the terminology “Finite Elements” in the sixties. It is worth noting that similar methods were already

[2]Stress parallel to the propagation direction.

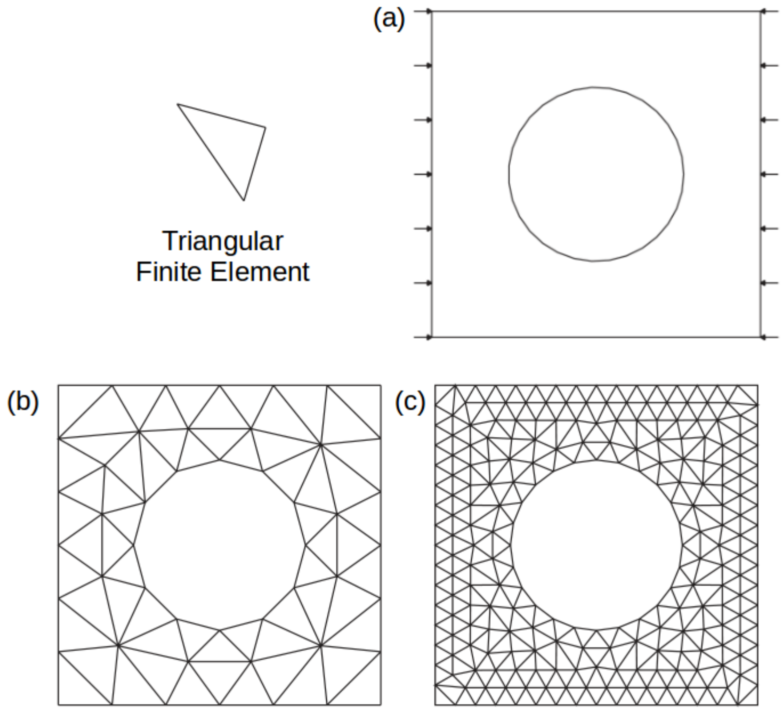

Figure 2.5: Discretization of a plate with a circular hole with triangular finite elements. (a) Desired geometry. (b) Coarse mesh. (c) Refined mesh. In this case, the more refined the mesh, the closer to the circular geometry. Adapted from Ref. [50].

used in applied mathematics a few years before [53], and at the end of the sixties it was mathematically proven that the increase of the number of elements led to convergence to the exact solution to the partial differential equation for linear problems [50].

The fast development of the FEM is related to the increase of speed and the reduction of cost of computers, both exponentially, which allowed the solution to even more complex problems to be obtained in a more efficient and faster approach [50]. Nowadays, there are plenty of commercial softwares, namely, NaStran™ that started at NASA, ANSYS™ that was initially formulated for analyzing nuclear reactors, and Abaqus™ which allows user implementations and is used in this project.

As an example of usage of FEM in the context of this work, an approach to identify the R-curve was derived from Mathieu et al. [54], which consisted first in determining the crack length during the test with the displacement field measured by DIC using the software Correli-Q4™ [44]. After that, these data were used in

Abaqus™ [55] to calculate K_I by numerical methods. A similar approach is applied to the WST [35] (see Section 3.3.2), with few modifications like the geometry and the constitutive model to better represent refractories.

Jin et al. [56] presented a methodology for obtaining the Young's modulus, the fracture energy and the fracture stress by inverse analysis of the WST. A trilinear law was selected for the stress to simulate the crack wake effect, and the parameters were obtained through nonlinear least-squares minimization. With this approach, with only one test, it is possible to estimate other parameters related to the mechanical properties of the studied refractory. The procedure was repeated for three samples and the results were consistent. This paper is a recent example of the importance of the development of couplings between the WST and its simulation to obtain material properties.

2.6 Cohesive Elements

In 1976, Hillerborg et al. [57] proposed a cohesive model that is not only suitable for FE analyses of concrete but also represents damage in castables during the fracture process. It assumes that the tractions are related to the crack mouth opening. The advantage of this type of element is that after a given load is reached, its rigidity decays with a pre-defined law, as exemplified in Figure 2.6. It is one way to represent damage in materials that remain with some cohesion between the newly created surfaces by a propagating crack, which can be related to adhesives in some applications or to the crack wake effect for castable refractories.

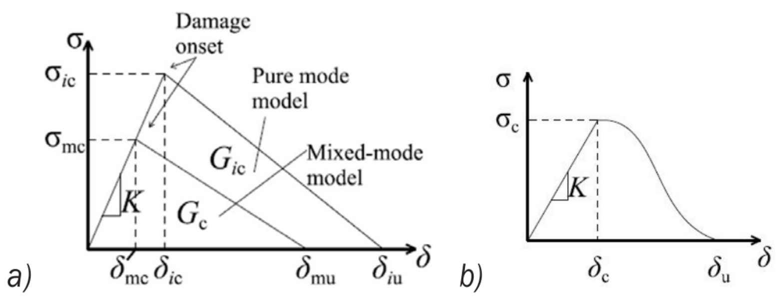

Figure 2.6: Two types of traction-separation laws, with some indicated parameters. (a) Triangular (or bilinear) law. (b) So-called modified PPR model. Adapted from Ref. [58].

Elices et al. [59] discussed many characteristics of cohesive elements and exemplified its usage in three different materials, *i.e.,* castable, polymethyl-methacrylate (PMMA), and steel, to demonstrate the potential and relevance of these types of models. The authors show how to define some cohesive properties and how useful they are to mixed-mode loadings (*e.g.,* mode I and II), even if the properties were obtained for mode I fracture. They also checked that two out of the four parameters of one of the cohesive laws needed stable crack propagation in order to be calibrated.

Moslemi and Khoshravan [58] studied the differences between a bilinear model and the modified Park-Paulino-Roesler (PPR) model, as shown in Figure 2.6. They also estimated the cohesive zone size and its discretization, reporting where care should be taken on the used mesh. Aure and Ioannides [60] used the cohesive elements implemented in the commercial software Abaqus™ to demonstrate how to model cracks in concrete, by comparing the results reported in the literature. The simulation properties were given through the thickness of the cohesive elements, with some characteristics that influence the results, *e.g.,* that usual Newton-Raphson routines should not be used in such cases. In the end, they checked that the traction-separation laws were the more suitable for concrete among those implemented in Abaqus™.

Evangelista et al. [61] reported a new formulation of cohesive elements to be used in Abaqus™ to analyze concrete fracture. The traction-separation of the element was developed based on damage mechanics, and conventional experiments were conducted to calibrate the parameters with physical meaning, and considering the irreversible mechanisms that occur during fracture. The proposed formulation uses zero thickness elements. Besides, they also discussed the stability of the obtained model by using a Riks algorithm instead of the standard Newton-Raphson scheme in Abaqus™ and about the robustness for cyclic loading, which is usually problematic for cohesive elements.

Some studies with DIC to calibrate CZM parameters were reported in the literature. For example, Ferreira et al. [62] used the Boundary Element Method coupled with DIC to identify elastic properties and proved that a linear cohesive law was suitable for concrete. Even with small displacements in comparison to measurement uncertainties, the use of measured displacement fields allowed for parameter identification of the studied model.

Shen and Paulino [63] used DIC coupled with FE analyses for parameter identification. A 4-point bend test and a Newton-Raphson routine were used to obtain the elastic properties. For the cohesive model, a pre-notched 3-point bend test was selected, and the Nelder-Mead optimization procedure was used due to difficulties to obtain initial guesses for derivative-based methods such as Newton-Raphson schemes.

The sensitivity to the parameter identification of cohesive properties using full-field measurements was also reported by Alfano et al. [64]. The authors discussed how separating the data throughout the test can improve the identification process. For instance, the cohesive strength is better identified with images before the peak load of the test, while the cohesive energy should be identified after the peak.

Su et al. [65] modeled static and dynamic crack propagation in 3D analyses using cohesive elements. One of the examples cited in this paper is the WST in which the crack wake effect in refractories was simulated by cohesive elements driven by a traction-separation law. The authors discussed which type of element was used and which parameter was set, besides the comparison of the experimental loading curves to simulated ones. Last, in a very recent paper, Ruybalid et al. [66] calibrated a mixed-mode CZM using only micrographs, without coupling force data.

This analysis shows the importance of calibrating these models, which is still an active research field.

2.7 Conclusion of the review

From the presented bibliographic review, it was highlighted that castable refractories are extremely important for many industries. Owing to their applications, certain properties are important such as resistance to thermal shock, and to damage by thermal shock. The brittleness of these materials implies the necessity of specific experiments to obtain their properties (*e.g.,* WSTs if stable crack propagation is desired and to calculate the fracture energy).

DIC may be applied to crack propagation tests such as the WST, to allow displacement fields to be measured in a way to ensure experimental insight into the fracture wake zone that would not be possible using common extensometry. The DIC measurements can be used as input in FE analyses, and also for validating their results. Moreover, FE analyses facilitate the stress analysis and allow the original geometry to be modeled even with its complexities such as grooves in WSTs.

Last, cohesive elements are suitable to simulate cracks in concrete since they allow cohesion to be kept during crack propagation, as a consequence, say, of toughening mechanisms. Thus, cohesive elements can simulate the crack wake effect, and once calibrated, allow measurements and comparisons about the development of this process zone, the R-curve of the material (*e.g.,* obtained by I-DIC). They give access to parameters related to the crack wake region length and provide a tool to better compare and select materials with high resistance to crack propagation.

3 MATERIAL AND METHODS

3.1 Material

The chosen material is a class C, anti-erosive commercial castable refractory classified as ultra-low cement type (*i.e.,* 0.2 < wt% CaO < 1.0 %), with 45 wt% Al_2O_3, 1.2 wt% Fe_2O_3, 50 wt% of SiO_2 for its chemical composition [49]. The typical mineralogical composition of the material consists of quartz (SiO_2), mullite ($Al_6Si_2O_{13}$), kyanite (Al_2SiO_5), β-cristoballite (SiO_2) and alumina (Al_2O_3) [67]. With a firing at temperatures around 540°C there is no expansive phase transformation from α-quartz to β-quartz, but anisotropic phases could cause thermal mismatch that initiates and propagates cracks in the specimen [68]. These microcracks along with some weakly bonded grains on the matrix could debond and lead to an R-curve behavior. Water was added to the mixture up to 8.5 wt% of concrete. Drying was performed for 48 h in a humid environment at room temperature followed by 24 h at 110°C. A heat treatment was performed with a 1°C/min rate and kept at 500°C for 24 h [35]. For the mechanical properties, the Young's modulus is equal to 17 GPa and the Poisson's ratio to 0.2 [49].

3.2 Experiment

A single WST (performed in previous work [49]) is analyzed herein using DIC. The sample geometry is shown in Figure 3.1, in which it is possible to see the contour of the sample of size $100 \times 100 \times 72.5$ (thickness) mm^3, and the loading device (*i.e.,* wedge, rollers, and blocks). Two grooves (*i.e.,* vertical notches, see dashed line in Figure 3.1) were machined on two opposite faces of the sample to reduce the local thickness and guide the crack propagation vertically, thereby allowing the methodologies discussed in Section 3.3 to be applied.

Two Canon T5 cameras with 28-135 mm lenses were used to acquire a total of 313 pictures for both faces of the specimen simultaneously, waiting for 8 s between each image. The illumination was provided by LEDs, and the 16-bit images had approximately 60,000 different gray levels. The picture definition is 2601 × 1733 pixels, in which each pixel corresponds to a physical size of 62 μm. In order to improve the contrast, a random speckle pattern was sprayed onto the

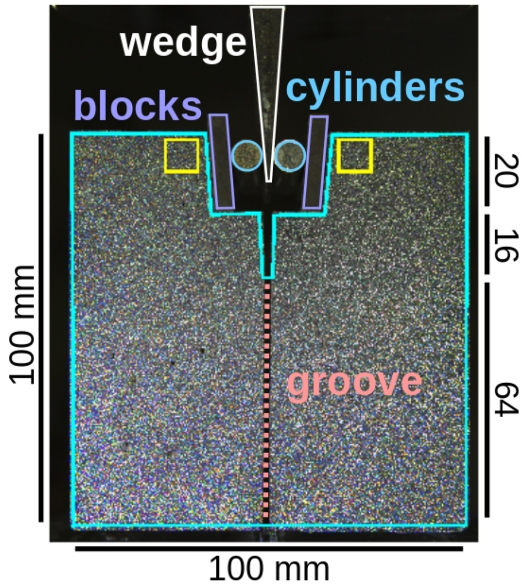

Figure 3.1: Detailed geometry of the wedge splitting test setup. The contour of the sample, including the pre-notch, is shown in cyan. The wedge, rollers and blocks used to apply the load are highlighted in white, blue and purple, respectively. The vertical groove guiding the crack vertically is shown as the dashed red line. The thickness of the specimen is 72.5 mm. All dimensions are expressed in mm. The yellow squares show the region used to measure the opening caused by the horizontal load and calculate the fracture energy in Ref. [35].

specimen surfaces that were photographed. The test was performed in an MTS 810 (controller TestStar IIs) and was driven by the displacement of the machine actuator with a velocity set to 1.3 μm/s. The loading curve of the experiment, *i.e.,* the vertical force F_v vs. vertical actuator displacement Δh, is shown in Figure 3.2. The experiment consisted of 5 cycles, two before the maximum load, and two after, with the unloading of the third cycle being close to the peak and the final unloading starting approximately at 70 % of the maximum load. Further information on this test can be found in Refs. [35, 49, 69], and the characterization of the studied material, processing and microstructure in Refs. [67, 68].

3.3 Methodologies

The three methodologies that were applied to the analysis of WST are discussed hereafter. It is worth noting that, although they may be extended for other cases, all of them consider a straight crack path. For the analyzed WST, this was ensured by the lateral grooves to guide crack propagation. However, one step of the methodology was to check this hypothesis, which can be a strong assumption

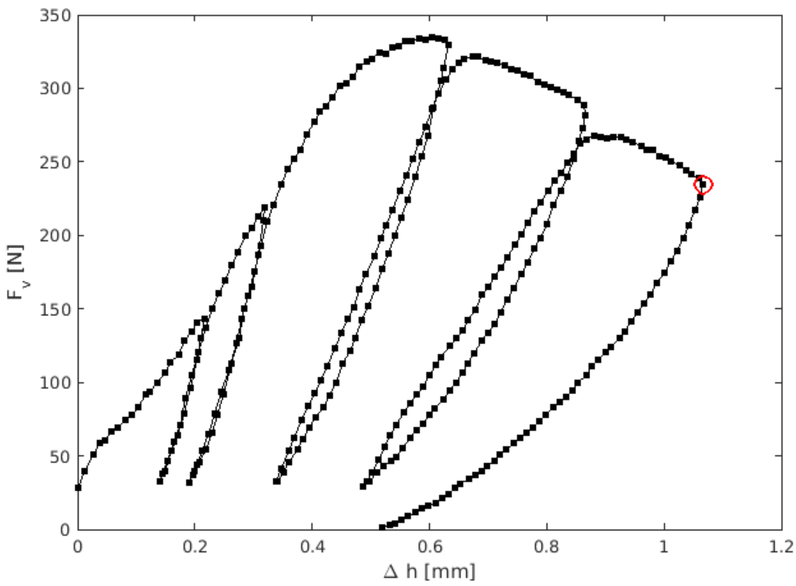

Figure 3.2: Loading history for the test analyzed in Section 4. Each point represents two image acquisitions (one per face, out of 312) performed during the test for DIC analyses. The red circle depicts the picture acquisitions used to evaluate the strain fields shown in Figure 3.3. After Ref. [35].

keeping in mind the heterogeneous nature of the material.

Figure 3.3 shows the maximum principal strain field at the end of the test [35]. It proves that the propagation was straight along the vertical direction in both analyzed faces.

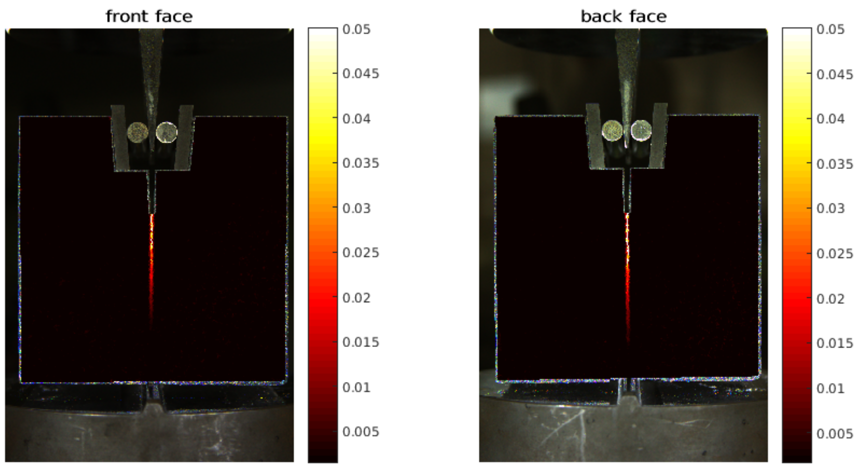

Figure 3.3: Maximum principal strain fields for both analyzed faces for the image before the 5-th unloading. No macrocrack branches are seen. The hypothesis of straight crack propagation guided by the groove can be made. After Ref. [35].

3.3.1 Integrated-DIC

The main scope of usual DIC is to obtain nodal displacements as discussed in Section 2.4. By defining the fields $\mathbf{\Psi}_i$ (introduced in Equation (2.10)) differently, it is possible to obtain directly mechanical parameters that correspond to those found in Williams' series [70] using the same DIC framework (*i.e.,* Correli 3.0 [71]). Considering the origin at the crack tip with the cracked surface on the negative x-axis, the displacements fields are written as [40]

$$\mathbf{u}(\mathbf{z}) = \sum_{j=I}^{II} \sum_{n=p_i}^{p_f} \omega_n^j \boldsymbol{\psi}_n^j(\mathbf{z}) \tag{3.1}$$

where the vector fields are defined in the complex plane

$$\mathbf{z} = x + yi = r \exp(i\theta) \tag{3.2}$$

and $j = I$ is related to mode I (opening) regime, and $j = II$ to mode II (shearing). The corresponding fields are described by [35]

$$\boldsymbol{\psi}_n^I = \frac{V_d(n)}{2\mu\sqrt{2\pi}} r^{n/2} \left[\kappa \exp\left(\frac{in\theta}{2}\right) - \frac{n}{2} \exp\left(\frac{i(4-n)\theta}{2}\right) + \left((-1)^n + \frac{n}{2}\right) \exp\left(-\frac{in\theta}{2}\right) \right] \tag{3.3}$$

and

$$\boldsymbol{\psi}_n^{II} = \frac{iV_d(n)}{2\mu\sqrt{2\pi}} r^{n/2} \left[\kappa \exp\left(\frac{in\theta}{2}\right) + \frac{n}{2} \exp\left(\frac{i(4-n)\theta}{2}\right) + \left((-1)^n - \frac{n}{2}\right) \exp\left(-\frac{in\theta}{2}\right) \right] \tag{3.4}$$

where κ is equal to $(3-\nu)/(1+\nu)$ for plane stress states or $3-4\nu$ for plane strain states (used herein), ν the Poisson's ratio, r the distance from the crack tip, θ the angular position and A(n) defined by

$$V_d(n) = \cos\left(\frac{n\pi}{2}\right)^2 + \sin\left(\frac{n\pi}{2}\right) \tag{3.5}$$

Equations (3.3) and (3.4) provide the sensitivity fields that after being multiplied by the amplitudes ω_i^j, which have a mechanical meaning, provide the sought displacement fields. Equation (3.5) inputs consistent vector directions (for mode I and mode II) in the vicinity of the crack tip for the fields related to odd values of n, and is equal to 1 or -1 for integer values of n. The amplitudes ω_1^I and ω_1^{II} give access to SIFs for mode I (K_I) and mode II (K_{II}), respectively. Figure 3.4 shows the two fields associated with mode I and mode II SIFs. For mode I fracture, the displacement perpendicular to the crack direction is discontinuous across the crack face. The crack tip is considered in the middle of the figures, and the cracked face at its left (*i.e.,* as crack propagation goes from the left to the right part of the image). Similarly, for mode II (shearing) cracking, the displacement parallel to the crack direction is discontinuous across the crack face.

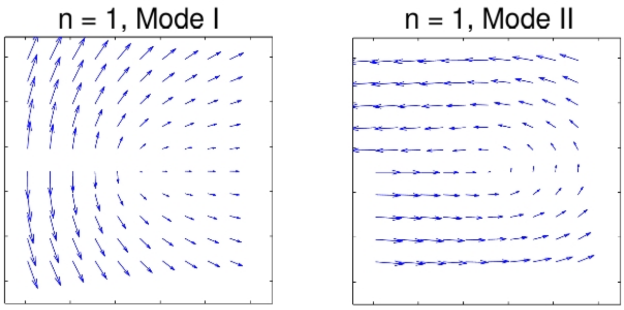

Figure 3.4: Displacement fields ψ_1^I (K_I) and ψ_1^{II} (K_{II})

The amplitude ω_2^I provides the so-called T-stress, ω_2^{II} the rigid body rotation as shown in Figure 3.5. Higher order fields are related to various boundary conditions and account for deviations from the theoretical assumption of an infinite medium. Note that for $n = 2$ the unitary sensitivity field is related to compression (see Figure 3.5), *i.e.,* a positive T-stress is compressive.

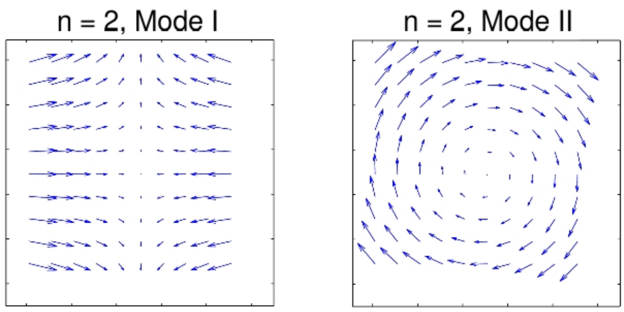

Figure 3.5: Displacement fields ψ_2^I (T-stress) and ψ_2^{II} (rotation)

With the use of two additional terms in the series, namely using $p_i = 0$, ω_0^I and ω_0^{II} are related to rigid body translations, and are depicted in Figure 3.6.

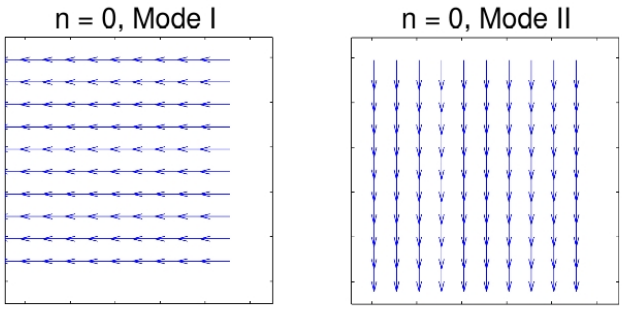

Figure 3.6: Displacement fields ψ_0^I and ψ_0^{II} related to rigid body translations

Although not usual, negative values of p_i can help to account for nonlinearities [54, 72]. It can be seen in Equations (3.3) and (3.4) that for negative values of n, super-singular solutions arise near the crack tip ($r = 0$). Considering a straight crack propagation along the x-axis the displacement related to a mispositioned crack tip by a small amplitude d reads [73]

$$\mathbf{u}(\mathbf{z} + d) = \mathbf{u}(\mathbf{z}) + d\frac{\partial \mathbf{u}(\mathbf{z})}{\partial \mathbf{z}} \tag{3.6}$$

and it can be noted that

$$-\frac{\partial \psi_n^j}{\partial x} = \frac{n}{2}\psi_{n-2}^j \tag{3.7}$$

Equation (3.1) can be substituted in Equation (3.6), in addition to the property shown in Equation (3.7) to obtain

$$\tilde{w}_n^j = w_n^j - d\frac{w_{n+2}^j(n+2)}{2} \tag{3.8}$$

where $\tilde{w}_n^j$ is the amplitude of the series after the shift and w_n^j before. Because of the singular character for $n = -1$ when $r = 0$, $\tilde{w}_{-1}^I$ should cancel out

$$d = \frac{2w_{-1}^I}{w_1^I} \tag{3.9}$$

which provides an estimation of the crack tip shift to find the correct solution. Although detailed in Ref. [49], the developed methodology to obtain the crack tip position consists of a sequence of actions that are briefly summarized:

1. Image acquisitions of the specimen during the mechanical test;

2. Consider a straight line as the crack propagation path, in the specimen vertical groove (see Figure 3.3);

3. Consider an initial crack tip position based on the maximum principal strain fields;

4. Define the parameters of Williams' Series, *i.e.,* its truncation;

5. Perform I-DIC to measure the amplitudes of the series for a selected crack tip position;

6. Update the crack tip position based on a recursive property of the series (see Equation (3.9));

7. Repeat steps 5 and 6 until convergence.

3.3.2 FEMU-U

The basic idea of Finite Element Model Updating (FEMU) using displacements in the error function (*i.e.,* FEMU-U) is described hereafter. To exemplify, a schematic representation is shown in Figure 3.7 [35]. First, T3-DIC is performed to measure displacement fields in a ROI chosen to monitor all the propagation region (middle of Figure 3.7). The same ROI is then considered in an FE model, and measured displacements (from DIC) are only applied to the outer contour (green box in Figure 3.7). A crack is considered (dashed red line in Figure 3.7) for a given tip position. The inner displacements from the FE analysis (*i.e.,* the ones that were not prescribed) allow for comparisons with DIC results in order to create an error function associated with the crack tip location. Several crack tip positions are tested and the one that provides the smallest displacement difference is considered as the actual crack tip position.

In order to build the FEMU-U error function, the FE displacement fields are interpolated onto the T3-DIC mesh. Then, the cost function is considered as the RMS difference between measured and computed displacement fields

$$\phi_u^2 = \sum_{i=1}^{N} \left(\upsilon_i^{\text{FE}} - \upsilon_i^{\text{DIC}} \right)^2 , \tag{3.10}$$

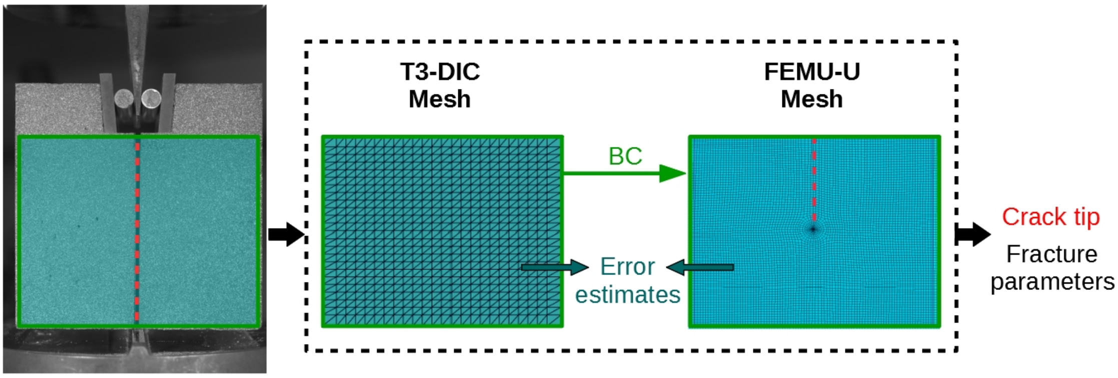

Figure 3.7: Left: DIC mesh used for measuring the displacement fields. Middle: acquired reference image showing the considered regions. Right: mesh used for the FEMU-U analysis. After Ref. [35].

in which v_i are nodal displacements components. The superscript indicates if the displacements are obtained from FE or T3-DIC analyses. The tested crack tip position that provides the minimum ϕ_u^2 is considered as the actual location, and the fracture parameters are then calculated for this geometry since the FE code also gives access to SIFs (*i.e.*, K_I and K_{II}) and the T-stress. It is worth noting that such analysis is performed for every image of the test. Further information about the methodology can be found in Ref. [35] (Appendix A).

Even though ϕ_u^2 is considered for crack tip identification, the gray level residual $\rho_{\text{FEMU-U}}$ can be computed, to compare the results directly at the image level, using the nodal displacements of the FE model $\{\boldsymbol{\upsilon}_{\text{FE}}\}$

$$\rho_{\text{FEMU-U}} = f(\mathbf{x}) - g\left(\mathbf{x} + \boldsymbol{\Psi}_{\text{FE}}(\mathbf{x}, \{\boldsymbol{\upsilon}_{\text{FE}}\})\right), \tag{3.11}$$

where $\boldsymbol{\Psi}_{\text{FE}}$ is the vector containing the shape functions converting nodal to pixel displacements, which is linearly dependent on the measured degrees of freedom $\{\boldsymbol{\upsilon}_{\text{FE}}\}$.

3.3.3 FEMU-F

In order to calibrate a cohesive law that describes as best as possible the mechanical behavior of the material, an approach is proposed and summarized in Figure 3.9. The DIC displacements are prescribed as Dirichlet BCs in the region where the force is applied to the specimen (red circles in Figure 3.9). The corner node is not used since it is related to higher uncertainties [74]. The groove is considered with smaller thickness, and in the middle of it a very thin cohesive element line is added (see Figure 3.9). The mesh is generated with GMSH [75]. Apart from the cohesive elements, the remaining part of the specimen is modeled with a linear elastic behavior.

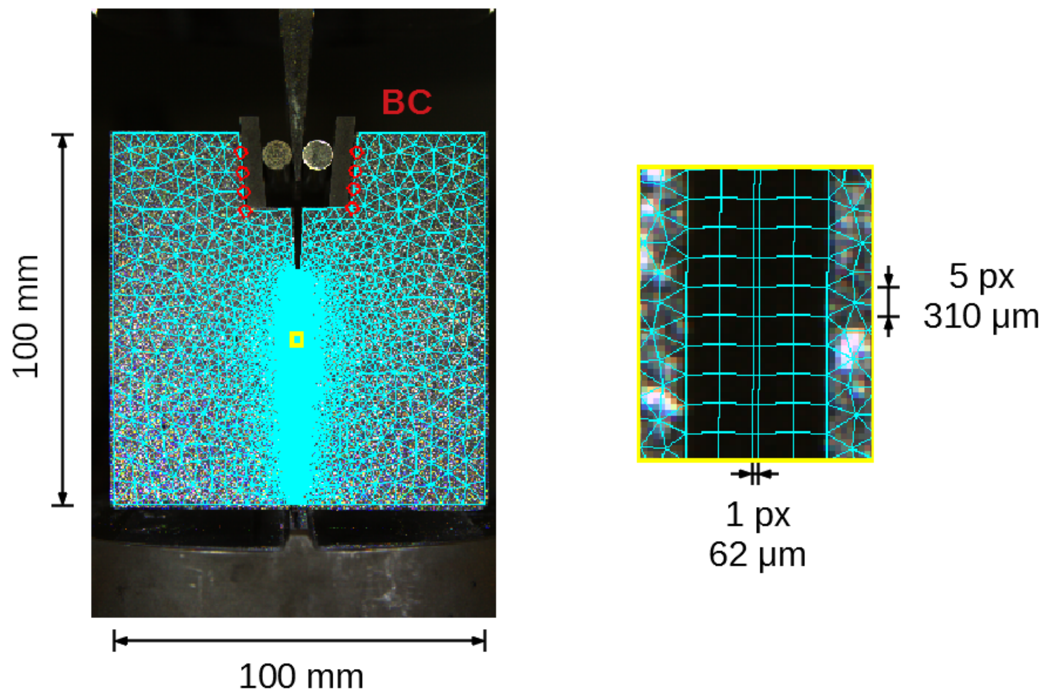

Figure 3.8: Sample geometry with the superimposed FE mesh (left). The loading parts are visible at the top. Red circles mark the nodes where BCs are applied. The yellow box is zoomed (right), showing the mesh aligned with the groove edges. Triangular elements are used out of the groove, and Q4 quadrilaterals inside. The thin strip of elements in the middle of the groove shows the cohesive elements.

Three CZMs are tested in this work, namely, a bilinear traction-separation (BLTS) model [57], a Concrete Damaged Plasticity (CDP) model [76], and the so-called Park-Paulino-Roesler (PPR) model [77]. The first one consists of a built-in option of Abaqus, using 4-noded quadrilateral elements (COH2D4 [55, 76]). The second one is a continuum, plasticity-based damage model [76], which is another built-in option of Abaqus and can also be used for cyclic cases (not considered herein). It was chosen not to use damage for the CDP model since it would not be distinguishable from plasticity with no unloading and the parameters of the plasticity model are considered the same as in Ref. [78]. The PPR model is a potential-based cohesive law [77, 79]. It was considered since the built-in cohesive models may give unrealistic responses for mixed mode propagations [80]. It is implemented in Abaqus with a User ELement (UEL) subroutine [79] [1].

The parameters of the three CZMs are taken to consider a bilinear traction-separation law, as shown in Figure 3.9, in order to be comparable. All the CZMs consider a linear elastic behavior until the peak load, σ_{max}, followed by a linear decrease of the traction in relation to the separation. The softening behavior is defined by the fracture energy parameter J_c, that bounds the maximum energy that can be dissipated in each element. A pure mode I regime is considered [35, 49], and care is taken so that the mode II properties would not disturb the results.

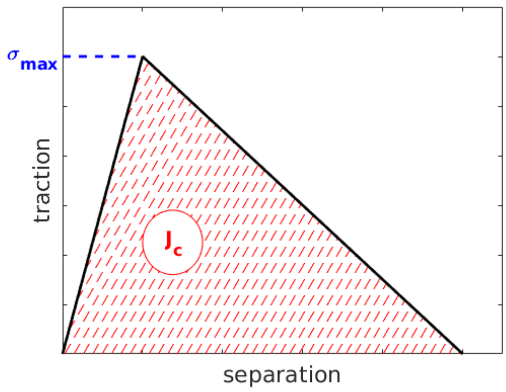

Figure 3.9: Schematic of the traction-separation law for the three CZMs.

Another parameter is added in the identification scheme since the reference image was acquired when the sample was pre-loaded. Since the unloaded state is unknown, this parameter compensates the displacement field related to this initial elastic loading, namely, from the unloaded state to the reference state and will be considered as a fraction of the displacement field of image 24 of the envelope response, *i.e.,* image 39 of the full history, represented by a blue square in Figure 3.10. This image (acquired at 50 % of the peak load) is believed to present a good trade-off between displacements significantly higher than the measurement uncertainty, while still being in the elastic regime. This parameter will be called

[1] The UEL code and some examples can be found at PPR UEL and Tutorial

BC_c, after Boundary Condition correction. It is formulated such that no correction corresponds to $BC_c = 1$. When $BC_c > 1$, an opening displacement correction is considered while $BC_c < 1$ is related to a correction with closing displacement fields. Further details on the implementation are given in Ref [69] (Appendix B).

Identification strategy

The chosen identification scheme is based upon Finite Element Model Updating (FEMU [81]). It is chosen to update the material parameters by reducing the difference between the calculated reaction force F_c and the experimentally measured force F_m (FEMU-F). It is worth noting that unloadings and elastic reloadings of the cycles are not used herein and only the envelope of the curve is kept (*i.e.,* 100 out of the 312 images for which the crack is propagating, see Figure 3.10). The envelope is chosen to have a continuous displacement of the actuator.

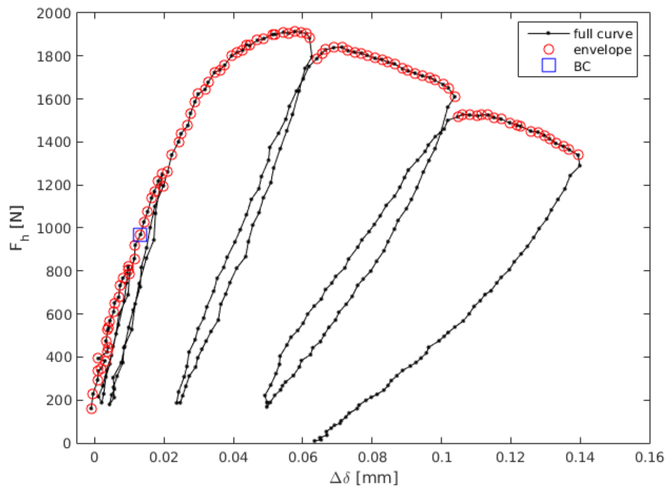

Figure 3.10: Horizontal force (*i.e.,* 5.715 times the vertical force) versus splitting displacement $\Delta\delta$ averaged on both sides of the sample. The 100 images corresponding to the displacement envelope used in the identification are marked with red circles. Image no. 39 (24 in the envelope set) used for the BC_c parameter as explained in Section 3.3.3 is shown as a blue square.

The identification methodology consists in a nonlinear least squares minimization of χ_F^2

$$\chi_F^2(\{\mathbf{p}\}) = \frac{1}{n_t \sigma_F^2} \sum_t (F_m(t) - F_c(t, \{\mathbf{p}\}))^2 , \tag{3.12}$$

in which σ_F is the standard load uncertainty (on F_m), n_t the number of time steps, and F_c is the computed resultant of the reaction forces, which depends on unknown material parameters gathered in the column vector $\{\mathbf{p}\}$. If the only difference between the measured load levels $F_m(t)$ and $F_c(t,\{\mathbf{p}\})$ is acquisition noise, then χ_F is equal to 1. Conversely, if there is a model error, then $\chi_F > 1$. By considering a given starting set of parameters $\{\mathbf{p}_n\}$ at iteration n, the minimization is performed by evaluating the correction $\{\delta\mathbf{p}\}$ on the linearized F_c

$$F_c(t,\{\mathbf{p}_n\}+\{\delta\mathbf{p}\}) \approx F_c(t,\{\mathbf{p}_n\}) + \frac{\partial F_c}{\partial\{\mathbf{p}\}}(t,\{\mathbf{p}_n\})\{\delta\mathbf{p}\}, \tag{3.13}$$

about the current estimate $\{\mathbf{p}_n\}$ of the sought parameters. The minimized quantity then becomes

$$\frac{1}{n_t\sigma_F^2}\sum_t\left(F_m(t) - F_c(t,\{\mathbf{p}_n\}) - \frac{\partial F_c}{\partial\{\mathbf{p}\}}(t,\{\mathbf{p}_n\})\{\delta\mathbf{p}\}\right)^2. \tag{3.14}$$

In Equation (3.14), the quantity to be minimized is quadratic in terms of $\{\delta\mathbf{p}\}$. Its minimization with respect to $\{\delta\mathbf{p}\}$ then leads to a linear system

$$[\mathbf{H}]\ \{\delta\mathbf{p}\} = \{\mathbf{h}\} \tag{3.15}$$

where $[\mathbf{H}]$ is the Hessian

$$[\mathbf{H}] = \sum_t\left(\frac{\partial F_c}{\partial\{\mathbf{p}\}}(t,\{\mathbf{p}_n\})\right)^{\top}\frac{\partial F_c}{\partial\{\mathbf{p}\}}(t,\{\mathbf{p}_n\}) \tag{3.16}$$

and $\{\mathbf{h}\}$ the right hand side member

$$\{\mathbf{h}\} = \sum_t\left(F_m(t) - F_c(t,\{\mathbf{p}_n\})\right)\frac{\partial F_c}{\partial\{\mathbf{p}\}}(t,\{\mathbf{p}_n\}). \tag{3.17}$$

The convergence criterion is based on the maximum relative variation of each sought parameters that is less than 10^{-2}. The sensitivity fields $\frac{\partial F_c}{\partial\{\mathbf{p}\}}$ are computed via finite differences in which the perturbation with respect to each parameter is set to 1 %. The framework of the identification methodology may be further discussed by the sensitivity analysis presented in Section 4.2.1 using the Hessian $[\mathbf{H}]$.

4 RESULTS AND DISCUSSIONS

This master thesis continues the work reported in Ref. [49], which used integrated DIC (Section 3.3.1). The same experiment was considered in the present analyses for comparison purposes. The first part of the results obtained during the master period is reported in Ref. [35], which uses the methodology explained in Section 3.3.2 and compares the results with those from Ref. [49]. The paper (Ref. [35]) is reproduced in Appendix A. The results for the second analysis (Section 3.3.3) are reported in Ref. [69], and the final version of the paper is reproduced in Appendix B. In this Section, the three different methodologies applied to the same test are compared in order to discuss the benefits of each technique.

4.1 FEMU-U analyses

Both I-DIC and FEMU-U analyses discussed herein give access to the same fracture mechanics parameters, *i.e.,* crack lengths, SIFs and T-stress. However, it is not straightforward to check which one was more trustworthy. For answering this question, a virtual experiment was first performed. The summary is presented in Figure 4.1 [35]. A 3D FE simulation of the WST was performed with a *known* crack tip position in a linear elastic specimen. Considering a plane strain hypothesis, the resulting displacements of the middle plane (red box in Figure 4.1) is used to numerically deform one reference image. Then, this deformed image is analyzed with both techniques in order to check if they provided similar parameters to the ones originally calculated in the FE model.

From the analysis of the virtual experiment (see Ref. [35], Appendix A), it was concluded that I-DIC achieves results closer to the 3D FE model for the crack length and K_I, but FEMU-U gives a closer T-stress. The K_{II} levels were very small as expected from a pure mode I propagation condition, and was considered to be of the order of the uncertainty level for both methods.

When both methodologies were applied to the experiment introduced in Section 3.2, they exhibited consistent results. Figure 4.2 shows the comparison between the I-DIC and the FEMU-U results. The smoothness of the I-DIC results in comparison to FEMU-U can also be related to the identification of the crack

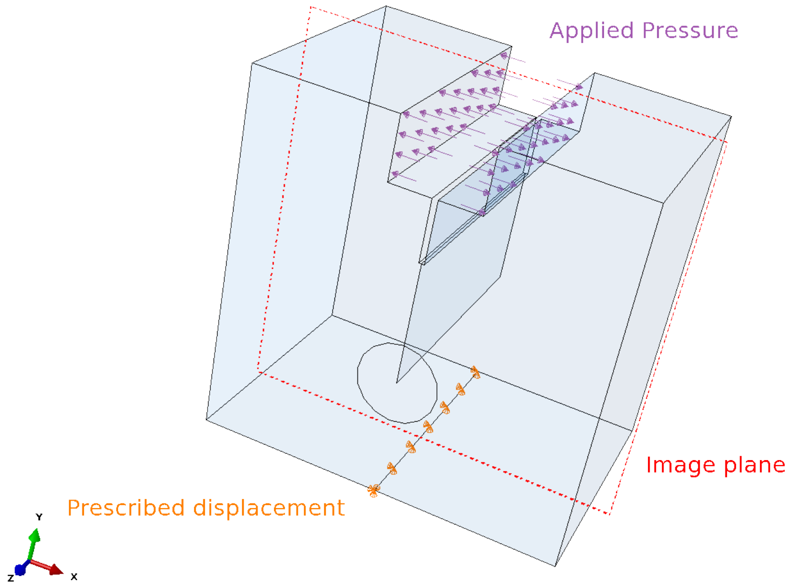

Figure 4.1: 3D Abaqus™ model showing the applied pressure and the prescribed displacements. It is also possible to see the partition lines in the middle of the crack propagation path. After Ref. [35].

tip. A range of imposed crack tip positions was tested for FEMU-U, restraining the solution in comparison to I-DIC. However, this discretization is fine, thus not significantly changing the obtained results. The determined fracture mechanics parameters lie in the same range, yet significant differences arise. It is interesting to note that FEMU-U yielded smaller crack lengths and higher K_I levels in comparison with I-DIC.

Even though the virtual experiment provided insight into which method would be more suitable for each sought parameter, two further validations were performed. The first one is related to gray level residuals, which were compared with conventional DIC residuals to check the validity of the results. For this analysis, special care must be taken [35]. Second, an energetic evaluation was performed by calculating the fracture energy with the loading history and the opening displacements (calculated at the yellow squares shown in Figure 3.1). The fracture energy was then compared with the mean value of the R-curve calculated with the SIFs and crack lengths. Both gray level residuals and the fracture energy analysis proved I-DIC to be more trustworthy for the studied experiment. Further details on the FEMU-U analyses are given in Appendix A.

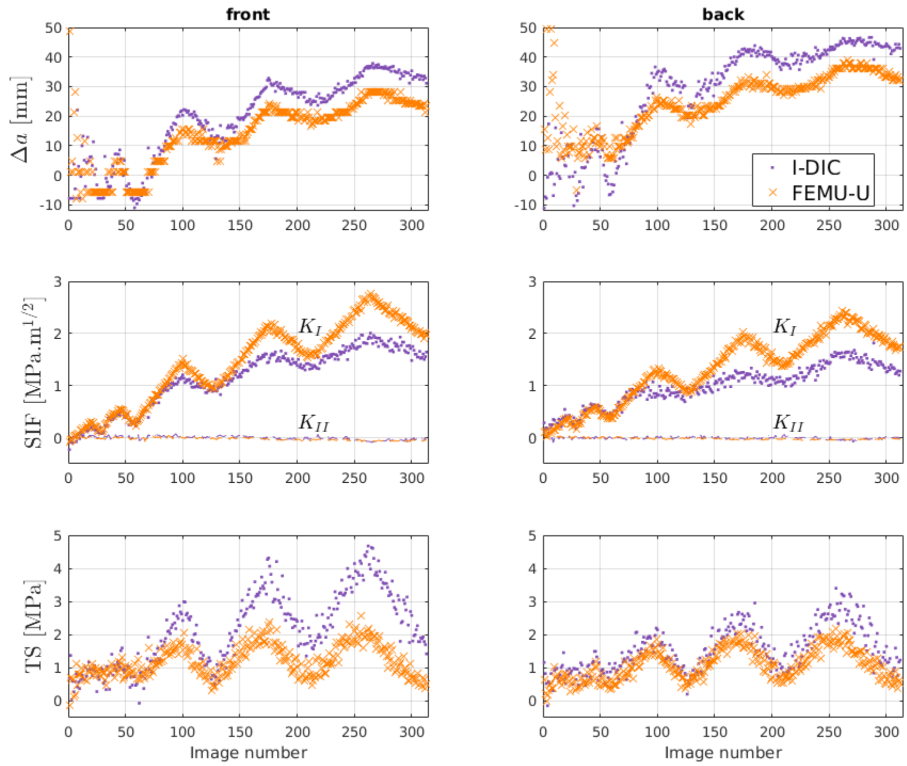

Figure 4.2: Summary of the results presented in Ref. [35]. The column on the left is related to the analysis of the front face of the specimen, and the column on the right is related to the back side. The first row shows the crack length for each analyzed image. The second row presents the SIFs, with markers for K_I and in dashed lines (close to zero) for K_{II}. Last, T-stresses are shown.

4.2 FEMU-F analyses

As will be shown in Figures 4.6 and 4.7, the studied CZMs are not suitable to analyze the full loading/unloading cycles. Therefore, this section aims to compare the three methodologies only using the images of the envelope of the loading curve.

4.2.1 Calibration results

Initial parameters

The properties used for initializing the identification scheme are listed in Table 4.1. The cohesive strength σ_{max} was selected as the maximum T-stress measured in Ref. [35] with the method that provided more trustworthy results for the T-stress (*i.e.,* FEMU). The initial fracture energy J_c corresponds to its estimate based upon Integrated-DIC results [35]. The last parameter, BC_c, has its initial value set to one (*i.e.,* no BC correction would be needed).

Table 4.1: Initial parameters for the identification scheme.

σ_{max} [MPa]	J_c [J/m^2]	BC_c [-]
2	68	1

Sensitivity analysis

Before calibrating the material parameters, a sensitivity analysis is performed [82]. The load sensitivities are defined as

$$S_F(t, \{\mathbf{p}_0\}) = \frac{\partial F_c}{\partial \{\mathbf{p}\}}(t, \{\mathbf{p}_0\}), \tag{4.1}$$

and computed for a perturbation factor $\epsilon = 10^{-2}$ of each parameter. Figure 4.3 shows the load sensitivity S_F calculated for the BLTS model. For the other models, S_F is not shown since it is very close and would not lead to qualitative differences. The image number on the x-axis is directly related to the time steps. The influence of the parameter BC_c is very important at the beginning of the test since the overall displacements are very small and the effect of this offset is important. The peak influence of the cohesive strength σ_{max} occurs in the middle of the sequence of images, which is related to the part of the test where the measured force is high. The fracture energy J_c has a higher sensitivity at the end of the test which is to be expected since the crack has propagated a significant distance [35, 49]. For all parameters, the load sensitivities are significant (in comparison with the load uncertainty) for a one percent variation of each parameter. These results indicate that the parameters are expected to be identifiable with the considered test and identification procedure since all the parameters show high sensitivities and the peaks are located in different time steps.

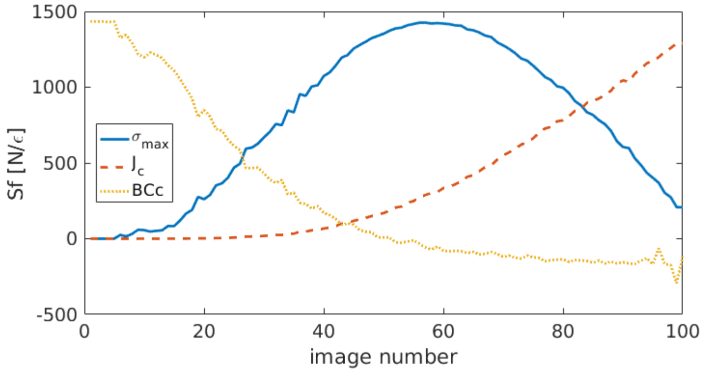

Figure 4.3: Force sensitivity to the parameters of the BLTS case. The blue solid line is the sensitivity to the cohesive strength σ_{max}, with a maximum sensitivity close to the middle of the test, *i.e.,* near the maximum splitting load. The red dashed line is related to the fracture energy J_c with a maximum sensitivity to the end of the test, after many elements are already damaged. The yellow dotted line corresponds to the BC correction BC_c, with maximum sensitivity at the beginning of the test where the displacements are very small.

Figure 4.4(a) shows the decimal logarithm of the values of the 3×3 Hessian ($[\mathbf{H}]$, see Equation (3.16)). The diagonal terms indicate the sensitivity to each property considered independently, and the off-diagonal members the cross influences between parameters. In the case of fully independent parameters, only the diagonal terms would be different from zero. As expected from the previous analysis, all parameters have very high sensitivities, and the conditioning of the system is very good (*i.e.,* less than 10). From this sensitivity analysis, it is confirmed that all parameters can be calibrated with the selected test and identification procedure.

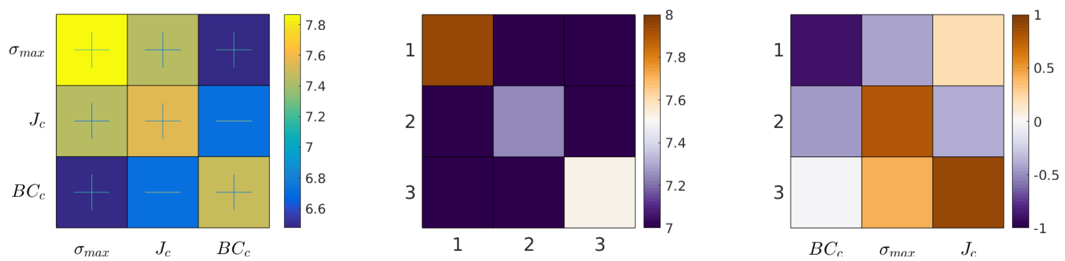

(a) (b) (c)

Figure 4.4: (a) Hessian of the identification procedure for the BLTS case shown as decimal logarithm. The diagonal terms show the sensitivity of each independent parameter. The off-diagonal terms show the cross influence between the parameters. (b) Decimal logarithm of the diagonalized Hessian. (c) Eigen column vectors associated with the diagonalization of the Hessian.

The decimal logarithm of the diagonalized Hessian is shown in Figure 4.4(b). The first value is dominant in BC_c and is almost independent of the other parameters. The second and the third eigen values are dominant in σ_{max} and J_c, in the same order of magnitude, showing that they are more correlated. Such conclusion is drawn from the eigen vectors reported in Figure 4.4(c).

Calibrated parameters

Following the FEMU-F procedure with the initial parameters gathered in Table 4.1, the identification converged in about 5 iterations. Figure 4.5 shows the loading curve for the experiment and for each analyzed CZM. Little differences are seen between the three models. The mean error between the numerical and experimental loading curves is of the order of twice the uncertainty of the load cell of the testing machine[1]. This very low level validates the three models for the selected part of the loading curve.

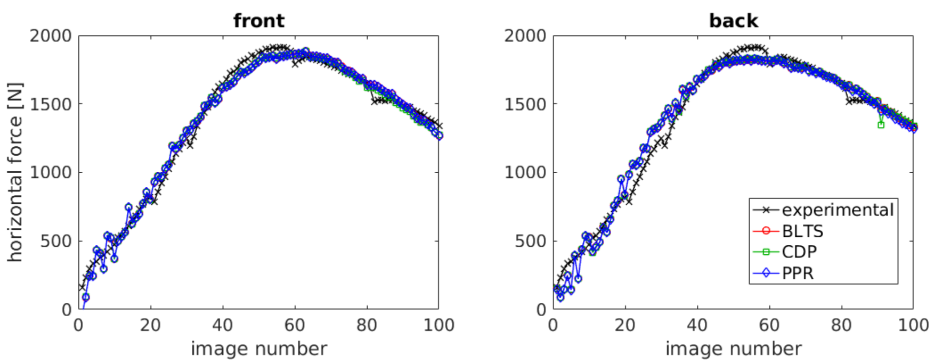

Figure 4.5: Splitting force for each analyzed image of the envelope. In black, the experimental data and in other colors the predictions of the three calibrated CZMs.

The converged parameters are summarized in Table 4.2. It is worth noting that very similar levels were obtained for the three cases when each face was considered separately. Only the fracture energy J_c has a factor 2 difference due to its implementation in Abaqus™ (CDP model).

[1]The load uncertainty is considered as 0.1 % of the 5 kN load cell capacity, *i.e.,* 5 N for the vertical force. Thereby, approximately 30 N for the horizontal force.

Table 4.2: Converged parameters of the FEMU-F scheme for the three studied CZMs.

face	model	σ_{max} [MPa]	J_c [J.m^{-2}]	BC_c [-]
front	BLTS	1.81	81.8	1.314
front	CDP	1.82	175 (2 × 87.5)	1.315
front	PPR	1.79	81.7	1.314
back	BLTS	1.59	89.9	0.899
back	CDP	1.60	194 (2 × 97.0)	0.898
back	PPR	1.58	88.7	0.897

4.2.2 Full loading history

In this section, all three CZMs are discussed considering the whole loading history. One of the biggest difference among the CZM usage from the fracture mechanics analysis (*i.e.,* with SIFs) is that the cohesive models response at each time step depends upon the previous steps. Although the kinematics depends on the load history, for I-DIC and FEMU-U, the load step is analyzed independently from the other ones and thus it is not affected by the previous results.

Considering this difference in procedures, the first result shown in Figure 4.6 is the full loading curve obtained with the cohesive models using the parameters calibrated with the loading envelope. The first two cycles are correctly described by the three models. Conversely, in the last three cycles, only the peak levels is in agreement with experimental observations. More complex CZMs would be needed to successfully describe the unloading and reloading phases. It is interesting to note how close the BLTS and PPR models are, and that both keep some tractions even for the most unloaded states between cycles. For the CDP case, a compressive state is seen at full unloading because the CDP model accounts only for plasticity and not for damage.

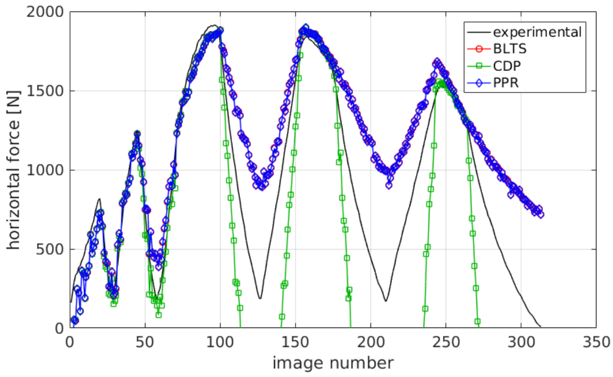

Figure 4.6: Splitting force for each analyzed image. In black, the experimental data and in other colors the predictions of the three CZMs calibrated with the envelope curve.

For better visualization of the differences observed in Figure 4.6, Figure 4.7 shows the absolute difference between the measured and predicted splitting forces normalized by the load cell uncertainty. Low error is seen until the maximum load, close to image 100, and then degrades beyond this level. A maximum error of the order of 25 is seen for the BLTS and PPR models, whereas the CDP error keeps increasing until a maximum of about 200 for the last image.

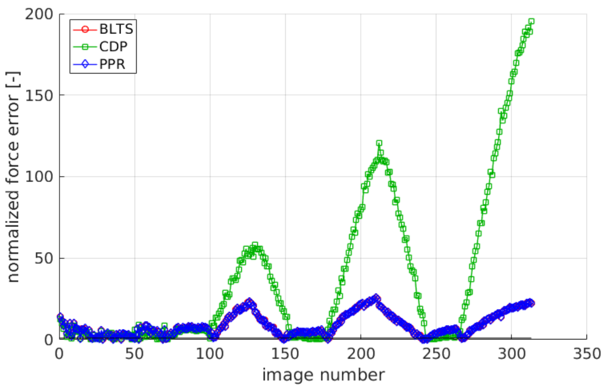

Figure 4.7: Absolute force error (see Figure 4.6) normalized by the machine load cell uncertainty.

4.3 Crack lengths and fracture energies

Since the methodologies do not give the exact same parameters, the results are converted into comparable quantities. First, the crack length is assessed (Figure 4.8). The I-DIC and FEMU-U methodologies yield the crack length as a direct output. For FEMU-F, the crack length is considered as the last element that has already initiated damage in a given time step (*i.e.,* it has enough opening to reach the cohesive strength σ_{max}). The cohesive zone approach results into longer cracks. I-DIC crack lengths lie between FEMU-F (BLTS, CDP and PPR) and FEMU-U results.

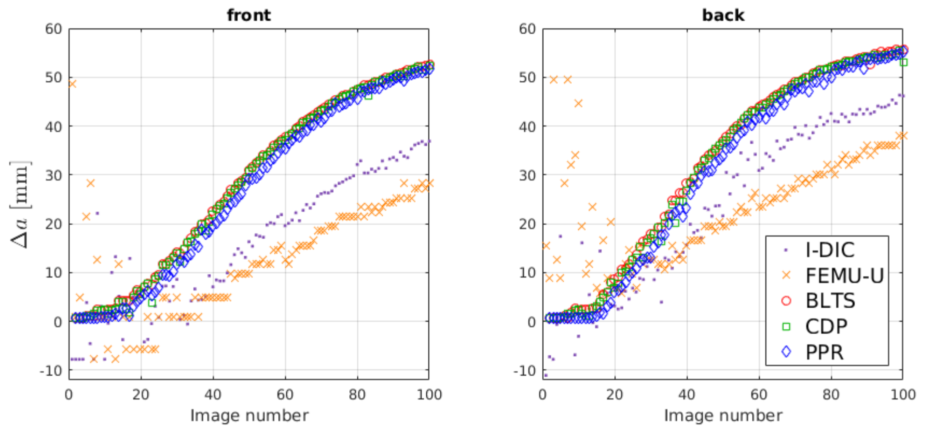

Figure 4.8: Cack length Δa for each analyzed image of the envelope for all the methodologies discussed in Section 3.3.

The R-curves are calculated for each case. For I-DIC and FEMU-U, linear elastic fracture mechanics equations are used [35] (Appendix A). For FEMU-F, the energy dissipated at each time step is integrated, and its derivative to the newly created cracked area gives access to the energy release rate, which is considered to be equal to its critical value [69] (Appendix B). Figure 4.9 shows the R-curves for each case. It is interesting to note that in I-DIC and FEMU-U cases, a noticeable difference was observed between the front and the back faces [35, 83]. It is not the case for FEMU-F. This difference is related to the correction for the pre-load state in the FEMU-F procedure. Such corrections are not straightforward for I-DIC and FEMU-U. It is possible to conclude that both I-DIC and FEMU-U are over-predicting the fracture energy for the front face and under-predicting for the back face in comparison with FEMU-F.

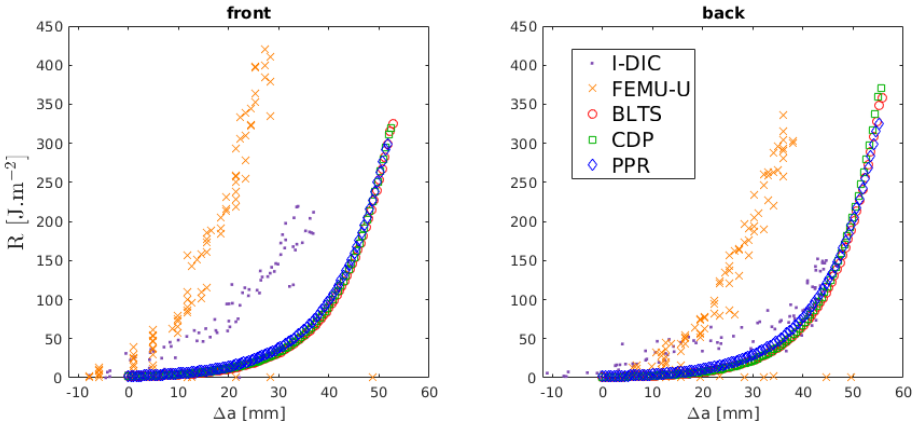

Figure 4.9: R-curves for each analyzed case by all the methodologies discussed in Section 3.3.

Although the R-curves themselves present good qualitative comparisons, the average fracture energy $\overline{R}$ is calculated for each case reported in Figure 4.9 and shown in Table 4.3. On average they remain close, especially when I-DIC is compared with FEMU-F. This last result validates the FEMU-F procedure and allows conclusions to be drawn on the material features associated with the reported R-curve behavior.

Table 4.3: Average fracture energy $\overline{\mathcal{G}}_c$ expressed in J/m^2 for the three CZMs applied to the back and front faces separately. These predictions are compared with earlier results obtained by two independent approaches (*i.e.,* integrated DIC [49] and FEMU-U [35]).

model	front face	back face
BLTS	60.9	60.6
CDP	60.9	61.9
PPR	61.3	62.4
IDIC$^\sharp$	84	52
FEMU-U$^\sharp$	162	97

$^\sharp$ according to Refs. [35, 49]

5 CONCLUSIONS AND PERSPECTIVES

Three different methodologies were applied to the same WST, namely, I-DIC, FEMU-U and FEMU-F. I-DIC provided more trustworthy crack lengths, SIFs and fracture energies, while FEMU-U resulted in a T-stress closer to the proposed virtual experiment. Both methodologies globally describe a crack propagating in an elastic medium. In the analyzed experiment, K_{II} SIFs are believed to be below the uncertainty range for both techniques. Every calculation with these two methods were independent for each image.

FEMU-F is the only one of the three proposed methods using cohesive elements and depends on the whole analyzed history. It proved to be suitable to model the WST. Although the unloading and reloading steps of each cycle were not yet fully analyzed, the envelope of the curve was well described by the simulation results with three different CZMs showing very low residuals in force, and also in terms of displacement and gray level residuals. The calculated fracture energy was in the same range as the previous two methods. A correction for the pre-loaded reference state was used to deal with the experimentally inherent misalignment of the wedge, and significantly reduced the differences of crack length and energy dissipation between both analyzed faces of the sample. Insights into the FPZ length were possible by calculating the so-called Hillerborg length and comparing it with space-time histories of tractions and damage.

Last, the present work highlighted the fact that one must not define a single crack tip position since it depends on the measurement method and the hypothesis considered. Information on how it was measured should always come with the crack lengths (*e.g.,* numerically, analytically, or optically) in order to properly analyze the results. All the methodologies enabled a lot more information to be extracted from a single test, apart from the usual work of fracture.

The material studied herein showed an FPZ length of the order of the sample size, and possibly longer had the sample being taller. The identified properties are compatible with the material, its microstructure, and processing, which helped to validate the proposed methodologies. The low-temperature firing led to weakly bonded aggregates that contributed for a low cohesive strength. As crack initiation is facilitated, bridging of the aggregates through the crack faces dissipates part of the energy by interface friction. Since the FPZ is not fully developed, these effects lead to an ever-increasing R-curve behavior.

As perspectives, several topics could not be tackled due to the length of this master project, coupled with the learning process of the student. The first and more logical way to proceed such study experimentally would be to analyze more samples using the same methodology, to compare different materials. Besides, even though the test that was stopped at 70 % of the peak load helped in many points, some questions arose that could possibly be answered by the analysis of a full propagation test.

Since all the methodologies described herein studied both external faces of the sample separately, another point worth of studying is their coupled analysis. 3D analyses would be carried out to check the crack profile within the sample. For validation of such procedures, a promising technique consists in performing in-situ WST via X-ray tomography. The use of 3D reconstructed images instead of 2D images for the crack propagation analysis could give further insight into the material and its toughening mechanisms.

Another challenging follow-up is to perform such tests at higher temperatures for which refractories are utilized. Challenges about image acquisition, heat haze effects, viscous effect on the mechanical behavior of the material, among many others, would need to be addressed. However, once dealt with, the fracture process of refractories at higher temperatures could be further understood and would presumably lead to new formulations and optimization to even higher efficiency thresholds than used nowadays.

6 BIBLIOGRAPHY

[1] Hasselman, D.P.H.. Unified theory of thermal shock fracture initiation and crack propagation in brittle ceramics. Journal of the American Ceramic society 1969;52(11):600–604.

[2] Brühwiler, E., Wittmann, F.H.. The wedge splitting test, a new method of performing stable fracture mechanics tests. Engineering Fracture Mechanics 1990;35(1-3):117–125.

[3] Wu, Z., Rong, H., Zheng, J., Xu, F., Dong, W.. An experimental investigation on the FPZ properties in concrete using digital image correlation technique. Engineering Fracture Mechanics 2011;78(17):2978 – 2990.

[4] Lee, W.E., Vieira, W., Zhang, S., Ghanbari Ahari, K., Sarpoolaky, H., Parr, C.. Castable refractory concretes. International Materials Reviews 2001;46(3):145–167.

[5] Luz, A.P., Braulio, M.A.L., Pandolfelli, V.C.. Refractory Castable Engineering; vol. 1. 1 ed.; São Carlos, SP: Göller Verlag; 2015.

[6] Wachtman, J.. Materials and Equipment - Whitewares - Refractory Ceramics - Basic Science: Ceramic Engineering and Science Proceedings, Volume 16. No. 1 in Ceramic Engineering and Science Proceedings; Wiley; 2009. ISBN 9780470316306.

[7] Lee, W.E., Moore, R.E.. Evolution of in situ refractories in the 20th century. Journal of the American Ceramic Society 1998;81(6):1385–1410.

[8] Studart, A.R.. Bioinspired ceramics: Turning brittleness into toughness. Nature materials 2014;13(5):433–435.

[9] Launey, M.E., Ritchie, R.O.. On the fracture toughness of advanced materials. Advanced Materials 2009;21(20):2103–2110.

[10] Callister, W.D., Rethwisch, D.G.. Materials Science and Engineering - An Introduction. 8 ed.; 2009.

[11] Barsoum, M.. Fundamentals of ceramics. CRC press; 2002.

[12] Roesler, J., Harders, H., Baeker, M.. Mechanical behaviour of engineering

materials: metals, ceramics, polymers, and composites. New York: Springer Berlin Heidelberg; 2007.

[13] Peret, C.M., Rodrigues, J.A.. Stability of crack propagation during bending tests on brittle materials. Cerâmica 2008;54:382–387.

[14] Steinbrech, R.W.. R-curve behavior of ceramics. In: Bradt, R., Hasselman, D., Munz, D., Sakai, M., Shevchenko, V., editors. Fracture Mechanics of Ceramics; vol. 9 of *Fracture Mechanics of Ceramics*. Springer US. ISBN 978-1-4613-6477-1; 1992, p. 187–208.

[15] Miyaji, D.Y., Tonnesen, T., Rodrigues, J.A.. Fracture energy and thermal shock damage resistance of refractory castables containing eutectic aggregates. Ceramics International 2014;40(9, Part B):15227–15239.

[16] Chantikul, P., Bennison, S.J., Lawn, B.R.. Role of grain size in the strength and r-curve properties of alumina. Journal of the American Ceramic Society 1990;73(8):2419–2427.

[17] Vekinis, G., Ashby, M.F., Beaumont, P.W.R.. R-curve behaviour of Al_2O_3 ceramics. Acta metallurgica et Materialia 1990;38(6):1151–1162.

[18] Steinbrech, R.W., Reichl, A., Schaarwächter, W.. R-Curve Behavior of Long Cracks in Alumina. Journal of the American Ceramic Society 1990;73(7):2009–2015.

[19] Kruzic, J.J., Satet, R.L., Hoffmann, M.J., Cannon, R.M., Ritchie, R.O.. The utility of R-curves for understanding fracture toughness-strength relations in bridging ceramics. Journal of the American Ceramic Society 2008;91(6):1986–1994.

[20] Mazzei, A.C., Rodrigues, J.A., Pandolfelli, V.C.. Alumina-mullite-zirconia composites obtained by reaction sintering Part II. R-Curve behavior. Journal of Materials Science 2000;35(11):2815–2824.

[21] Li, C.W., Yamanis, J.. Super-Tough Silicon Nitride with R-Curve Behavior. In: A Collection of Papers Presented at the 13th Annual Conference on Composites and Advanced Ceramic Materials: Ceramic Engineering and Science Proceedings. Wiley Online Library; 1989, p. 632–645.

[22] Wegst, U.G.K., Bai, H., Saiz, E., Tomsia, A.P., Ritchie, R.O.. Bioinspired structural materials. Nature materials 2015;14(1):23.

[23] Munch, E., Launey, M.E., Alsem, D.H., Saiz, E., Tomsia, A.P., Ritchie, R.O.. Tough, bio-inspired hybrid materials. Science 2008;322(5907):1516–1520.

[24] Ritchie, R.O.. The conflicts between strength and toughness. Nature materials 2011;10(11):817.

[25] Demetriou, M.D., Launey, M.E., Garrett, G., Schramm, J.P., Hofmann, D.C., Johnson, W.L., et al. A damage-tolerant glass. Nature materials 2011;10(2):123.

[26] Sih, G.C.. Handbook of stress-intensity factors. Lehigh University, Institute of Fracture and Solid Mechanics; 1973.

[27] Tada, H., Paris, P.C., Irwin, G.R.. The stress analysis of cracks. Handbook, Del Research Corporation 1973;.

[28] Guinea, G.V., Elices, M., Planas, J.. Stress intensity factors for wedge-splitting geometry. International Journal of Fracture 1996;81(2):113–124. doi:10.1007/BF00033177.

[29] Seitl, S., Veselỳ, V., Řoutil, L.. Two-parameter fracture mechanical analysis of a near-crack-tip stress field in wedge splitting test specimens. Computers & Structures 2011;89(21-22):1852–1858.

[30] Karihaloo, B.L., Xiao, Q.Z.. Higher order terms of the crack tip asymptotic field for a wedge-splitting specimen. International Journal of Fracture 2001;112(2):129–137.

[31] Karihaloo, B.L., Abdalla, H., Xiao, Q.Z.. Coefficients of the crack tip asymptotic field for wedge splitting specimens. Engineering Fracture Mechanics 2003;70(17):2407–2420.

[32] Tschegg, E.. Prüfeinrichtung zur Ermittlung von bruchmechanishen Kennwerten sowie hiefür geeignete, Prüfkörper, Austrian Pat. AT 390328B, registered. 1986.

[33] Harmuth, H.. Stability of crack propagation associated with fracture energy

determined by wedge splitting specimen. Theoretical and Applied Fracture Mechanics 1995;23:103–108.

[34] Ribeiro, S., Rodrigues, J.A.. The influence of microstructure on the maximum load and fracture energy of refractory castables. Ceramics International 2010;36(1):263–274.

[35] Vargas, R., Neggers, J., Canto, R.B., Rodrigues, J.A., Hild, F.. Comparison of two full-field identification methods for the wedge splitting test on a refractory. Journal of the European Ceramic Society 2018;38(16):5569 – 5579.

[36] Ribeiro, S., Exposito, C.C.D., Rodrigues, J.A.. Projeto, adaptação, instalação e testes preliminares para um sistema de medida de energia de fratura de materiais cerâmicos pelo método da cunha. Cerâmica 2008;54:418–426.

[37] McNeill, S., Peters, W., Sutton, M.. Estimation of stress intensity factor by digital image correlation. Engineering Fracture Mechanics 1987;28(1):101–112.

[38] Abanto-Bueno, J., Lambros, J.. Investigation of crack growth in functionally graded materials using digital image correlation. Engineering Fracture Mechanics 2002;69:1695–1711.

[39] Forquin, P., Rota, L., Charles, Y., Hild, F.. A method to determine the toughness scatter of brittle materials. International Journal of Fracture 2004;125(1):171–187.

[40] Mathieu, F., Hild, F., Roux, S.. Identification of a crack propagation law by digital image correlation. International Journal of Fatigue 2012;36(1):146–154.

[41] Saracura, R.G.M., Canto, R.B., Pandolfelli, V.C., Schmitt, N., Hild, F.. Surface crack network detection on MgO-based refractory castable by digital image correlation. China's Refractories 2015;24(1):32–37.

[42] Sutton, M.A.. Computer vision-based, noncontacting deformation measurements in mechanics: A generational transformation. Applied Mechanics Reviews 2013;65(AMR-13-1009, 050802).

[43] Hild, F., Roux, S.. Digital Image Correlation. Weinheim (Germany): Wiley-VCH; 2012, p. 183–228.

[44] Besnard, G., Hild, F., Roux, S.. "Finite-Element" displacement fields analysis from digital images: Application to Portevin-Le Chatelier bands. Experimental Mechanics 2006;46(6):789–803.

[45] Leclerc, H., Périé, J., Roux, S., Hild, F.. Integrated digital image correlation for the identification of mechanical properties; vol. LNCS 5496. Berlin (Germany): Springer; 2009, p. 161–171.

[46] Roux, S., Hild, F., Leclerc, H.. Mechanical assistance to dic. In: Espinosa, H., Hild, F., editors. Full field measurements and identification in Solid Mechanics; vol. Procedia IUTAM, 4. Elsevier; 2012, p. 159–168.

[47] Réthoré, J., Hild, F., Roux, S.. Extended digital image correlation with crack shape optimization. International Journal for Numerical Methods in Engineering 2008;73(2):248–272.

[48] Roux, S., Hild, F.. Stress intensity factor measurements from digital image correlation: post-processing and integrated approaches. International Journal of Fracture 2006;140(1-4):141–157.

[49] Vargas, R., Neggers, J., Canto, R.B., Rodrigues, J.A., Hild, F.. Analysis of wedge splitting test on refractory castable via integrated DIC. Journal of the European Ceramic Society 2016;36(16):4309–4317.

[50] Fish, J., Belytschko, T.. A first course in finite elements. John Wiley & Sons Limited; 2007.

[51] Turner, M.J., Clough, R.W., Martin, H.C., Topp, L.J.. Stiffness and deflection analysis of complex structures. Journal of the Aeronautical Sciences 1956;23(9):805–824.

[52] Clough, R.W.. Early history of the finite element method from the view point of a pioneer. International Journal for Numerical Methods in Engineering 2004;60(1):283–287.

[53] Courant, R.. Variational methods for the solution of problems of equilibrium and vibrations. Bulletin of the American Mathematical Society 1943;49(1):1–

23.

[54] Mathieu, F., Aimedieu, P., Guimard, J.M., Hild, F.. Identification of interlaminar fracture properties of a composite laminate using local full-field kinematic measurements and finite element simulations. Composites Part A: Applied Science and Manufacturing 2013;49:203–213.

[55] Hibbitt, , Karlsson, . Sorensen, Inc. ABAQUS Theory Manual. 2000.

[56] Jin, S., Gruber, D., Harmuth, H.. Determination of Young's modulus, fracture energy and tensile strength of refractories by inverse estimation of a wedge splitting procedure. Engineering Fracture Mechanics 2014;116:228 – 236.

[57] Hillerborg, A., Modéer, M., Petersson, P.E.. Analysis of crack formation and crack growth in concrete by means of fracture mechanics and finite elements. Cement and Concrete Research 1976;6(6):773–782.

[58] Moslemi, M., Khoshravan, M.. Cohesive zone parameters selection for mode-I prediction of interfacial delamination. Strojniski Vestnik/Journal of Mechanical Engineering 2015;61(9):507–516.

[59] Elices, M., Guinea, G., Gómez, J., Planas, J.. The cohesive zone model: advantages, limitations and challenges. Engineering Fracture Mechanics 2002;69:137–163.

[60] Aure, T., Ioannides, A.. Simulation of crack propagation in concrete beams with cohesive elements in abaqus. Transportation Research Record: Journal of the Transportation Research Board 2010;(2154):12–21.

[61] Evangelista, F., Roesler, J.R., Proença, S.P.. Three-dimensional cohesive zone model for fracture of cementitious materials based on the thermodynamics of irreversible processes. Engineering Fracture Mechanics 2013;97:261–280.

[62] Ferreira, M., Venturini, W., Hild, F.. On the analysis of notched concrete beams: From measurement with digital image correlation to identification with boundary element method of a cohesive model. Engineering Fracture Mechanics 2011;78(1):71 – 84.

[63] Shen, B., Paulino, G.H.. Identification of cohesive zone model and elastic parameters of fiber-reinforced cementitious composites using digital image correlation and a hybrid inverse technique. Cement and Concrete Composites 2011;33(5):572–585.

[64] Alfano, M., Lubineau, G., Paulino, G.H.. Global sensitivity analysis in the identification of cohesive models using full-field kinematic data. International Journal of Solids and Structures 2015;55:66–78.

[65] Su, X., Yang, Z., Liu, G.. Finite Element Modelling of Complex 3D Static and Dynamic Crack Propagation by Embedding Cohesive Elements in Abaqus. Acta Mechanica Solida Sinica 2010;23(3):271 – 282.

[66] Ruybalid, A.P., Hoefnagels, J.P.M., van der Sluis, O., van Maris, M.P.F.H.L., Geers, M.G.D.. Mixed-mode cohesive zone parameters from integrated digital image correlation on micrographs only. International Journal of Solids and Structures 2018;.

[67] Miyaji, D.Y., Otofuji, C.Z., Cabrelon, M.D., Medeiros, J., Rodrigues, J.A.. The coke effect on the fracture energy of a refractory castable for the petrochemical industry. In: Proceedings of the Unified International Technical Conference on Refractories (UNITECR 2013). Wiley Online Library; 2014, p. 1111–1116.

[68] Pereira, A.H.A., Miyaji, D.Y., Cabrelon, M.D., Medeiros, J., Rodrigues, J.A.. A study about the contribution of the α-β phase transition of quartz to thermal cycle damage of a refractory used in fluidized catalytic cracking units. Cerâmica 2014;60:449–456.

[69] Vargas, R., Neggers, J., Canto, R.B., Rodrigues, J.A., Hild, F.. Analysis of a castable refractory using the wedge splitting test and cohesive zone model. Journal of the European Ceramic Society 2019;39(13):3903–3914.

[70] Williams, M.L.. On the stress distribution at the base of a stationary crack. Journal of Applied Mechanics 1957;24(1):109–114.

[71] Leclerc, H., Neggers, J., Mathieu, F., Roux, S., Hild, F.. Correli 3.0. 2015. IDDN.FR.001.520008.000.S.P.2015.000.31500.

[72] Henninger, C., Roux, S., Hild, F.. Enriched kinematic fields of cracked structures. International Journal of Solids and Structures 2010;47(24):3305–3316.

[73] Roux, S., Réthoré, J., Hild, F.. Digital image correlation and fracture: An advanced technique for estimating stress intensity factors of 2D and 3D cracks. Journal of Physics D: Applied Physics 2009;42:214004.

[74] Hild, F., Roux, S.. Comparison of local and global approaches to digital image correlation. Experimental Mechanics 2012;52(9):1503–1519.

[75] Geuzaine, C., Remacle, J.F.. Gmsh: A 3D finite element mesh generator with built-in pre-and post-processing facilities. International Journal for Numerical Methods in Engineering 2009;79(11):1309–1331.

[76] Abaqus 6.14 Documentation. Dassault Systèmes Simulia Corp.; Providence, RI, USA.; 2014.

[77] Park, K., Paulino, G.H., Roesler, J.R.. A unified potential-based cohesive model of mixed-mode fracture. Journal of the Mechanics and Physics of Solids 2009;57(6):891–908.

[78] Jankowiak, T., Lodygowski, T.. Identification of parameters of concrete damage plasticity constitutive model. Foundations of civil and environmental engineering 2005;6(1):53–69.

[79] Park, K., Paulino, G.H.. Computational implementation of the PPR potential-based cohesive model in ABAQUS: educational perspective. Engineering Fracture Mechanics 2012;93:239–262.

[80] Park, K., Choi, H., Paulino, G.H.. Assessment of cohesive traction-separation relationships in ABAQUS: A comparative study. Mechanics Research Communications 2016;78:71–78.

[81] Pagnacco, E., Caro-Bretelle, A.S., Ienny, P.. Parameter Identification from Mechanical Field Measurements using Finite Element Model Updating Strategies; chap. 9. Wiley-Blackwell; 2012, p. 247–274.

[82] Fedele, R., Raka, B., Hild, F., Roux, S.. Identification of adhesive properties in GLARE assemblies using digital image correlation. Journal of the

Mechanics and Physics of Solids 2009;57(7):1003–1016.

[83] Vargas, R., Rodrigues, J.A., Canto, R.B., Neggers, J., Hild, F.. On the importance of analyses of two opposite faces for wedge splitting tests with DIC. In: 10th European Solid Mechanics Conference (ESMC2018). Bologna, Italy; 2018, p. 53.

APPENDIX A: comparison of FEMU-U and I-DIC (Section 3.3.2)

Comparison of two full-field identification methods for the wedge splitting test on a refractory

R. Vargas[a,], J. Neggers[b], R. B. Canto[a], J. A. Rodrigues[a], F. Hild[b]

[a]*DEMa - UFSCar, Rodovia Washington Luis, km 235, 13565-905 São Carlos-SP, Brazil*
[b]*Laboratoire de Mécanique et Technologie (LMT)*
ENS Paris-Saclay, CNRS, Université Paris-Saclay
61 avenue du Président Wilson, 94235 Cachan, France

Abstract

Two full-field identification methods are applied to the Wedge Splitting Test (WST) to obtain crack tip positions, stress intensity factors (SIFs) and T-stress. The first method is based on Finite Element Model Updating (FEMU), and the second is integrated digital image correlation (IDIC). Both are applied to a simplified virtual experiment and then to a cyclic WST. The gray level residuals are used to assess which results are more trustworthy. Fracture energy analyses are performed to validate the estimated R-curves.

Keywords: Crack tip position, digital image correlation, finite element model updating, stress intensity factors, virtual test, crack propagation

[*]Corresponding author
Email address: `hild@lmt.ens-cachan.fr` (F. Hild)

1. Introduction

Refractory castables are ceramics that enable functional properties to be maintained in aggressive applications, generally at high temperatures [1]. Not only the chemical composition but also raw material characteristics should be considered when designing new formulations since they affect the resulting phases, microstructures and thermomechanical properties [2]. Different compositions may be needed for the same application because of several thermomechanical loading steps during industrial processes [3], which spur innovations to improve performance such as increasing reactiveness during processing by using nanomaterials [2] or mimicking microstructures observed in nature [4]. In high risk applications, the material and mechanical properties should be well understood to better predict failures and thereby prevent accidents, while maximizing efficiency and lifetime [5].

The Wedge Splitting Test (WST) is a mechanical experiment allowing crack propagation to be assessed in (quasi)brittle materials [6, 7]. It leads to stable crack propagation by decreasing the elastic energy stored in the machine using a wedge and cylinders to apply the load [8]. A high fractured-area to volume ratio leads to achieving representative results for coarser microstructures at laboratory scales [7]. The classical goal of WSTs is to obtain the fracture energy, by integrating the load vs. displacement curve and dividing by the projected fractured area [7]. Although important, the fracture energy itself is not the only information that can be extracted from WSTs. Recently, it is becoming common practice to seek more data from each of these tests to better understand the fracture process. Relationships between WST measurements with microstructures can be obtained [9], and various works have shown how different compositions affect crack propagation (with the WST) for magnesia-spinel [10], Al_2O_3-C [11], Al_2O_3-MgO-CaO [12], and MgO-C [13, 14] systems. It is also possible to identify fracture properties using measured load data and compare them with numerical simulations of the WST [15].

More experimental data can be acquired from WSTs via full-field measurements. Among them, Digital Image Correlation (DIC) enables displacement fields to be measured [16], and has been successfully used in crack propagation analyses [17, 18, 19, 20, 21, 22]. DIC was already applied to WSTs to analyze the strain fields for microcrack formation in magnesia refractories, when a spinel phase was added [23]. Similar ideas were used to quantify the fracture process zone of magnesia refractories, and highlight how microcracks tend to decrease the strength but increase the fracture energy [24], and to estimate the crack growth resistance [25]. Another interesting approach is to measure crack propagation while checking the discontinuities in the displacement field [26]. An integrated-DIC (IDIC) scheme to measure the R-curve behavior was also proposed [27] by considering closed-form solutions of one propagating crack in an elastic medium [28].

The aforementioned test [27] will be considered herein in order to compare two different approaches for estimating fracture mechanics parameters using full-field measurements. It is important to note that the hypothesis of one straight crack is reasonable in experiments with the presence of a groove on the propagating faces, as commonly used for the WST to ensure more straight crack propagation [29]. However, crack branches may occur in the WST [25] and it should be checked for each test. With both approaches investigated herein, this check is part of the methodology.

In this paper, a procedure based on the methodology used in Ref. [30] is applied to the WST. By using the outer measurements from DIC analyses as Boundary Conditions (BC) for a Finite Element (FE) analysis and using internal nodes for error estimators, it is possible to determine the crack tip position and calculate Stress Intensity Factors (SIFs), *i.e.,* K_1 and K_2, and the T-stress. It will then be compared with IDIC. First, the experiment, the DIC principles and both methodologies that will be compared are introduced. It is followed by an analysis of a virtual experiment. Then an experimental study is performed to compare both methods.

2. Methods

The two methods studied herein are summarized hereafter. Both of them were used independently to analyze various experiments with cracks [30, 31, 20, 27]. However, they were never compared with the same data set, be they synthetic or from an actual experiment. The first method couples FE analyses and DIC measurements in order to determine the crack tip position, stress intensity factors and T-stresses [30]. It belongs to the class of finite element model updating techniques [32]. The second approach corresponds to integrated DIC [20], which is a standalone technique in comparison with the previous framework when applied to the analysis of cracked samples. Augmented Williams' series [28] are used, in particular, for the determination of the crack tip position [33, 34].

2.1. Experiment

The WST analyzed herein was performed on a class C, anti-erosive commercial refractory, with ultra low cement content, whose typical mineralogical composition consists of quartz, mullite, kyanite, β-cristoballite and alumina [27]. Water was added to the mixture up to 8.5 wt% of concrete. Drying was performed for 48h in humid environment at room temperature followed by 24h at 110°C. A heat treatment was performed with a 1°C/min rate and kept at 500°C for 24h. The detailed chemical composition and the treatment of the material are reported in Ref. [27]. Its processing and microstructure may lead to an increasing R-curve behavior, with weakly bonded grains and initiated microcracks due to anisotropic phases and differential thermal expansions.

The sample size is 100 mm in length, 100 mm in height and 72.5 mm in thickness. The geometry is shown in Figure 1, in which it is possible to see the contour of the sample and the loading devices (wedge, cylinders and blocks). Two grooves (*i.e.,* lateral notches, see dashed line in Figure 1) are machined on two opposite faces of the sample to reduce the local thickness and guide the crack propagation vertically. The two zones where the splitting displacement is evaluated via DIC are also shown in Figure 1 as yellow boxes. Considering δ as the initial distance between both zones, the horizontal displacements measured on these regions are averaged and their difference accounts for the splitting displacement $\Delta\delta$, which will be reported in Section 4.

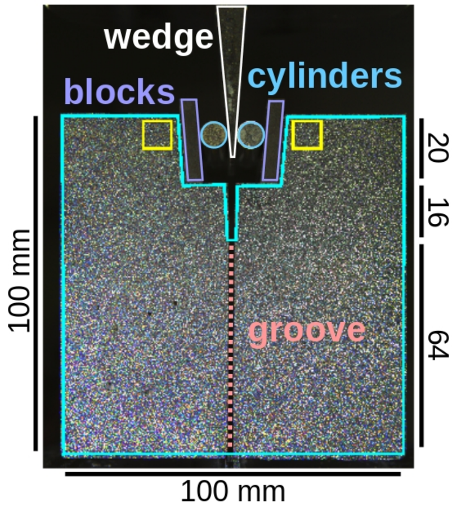

Figure 1: Detailed geometry of the wedge splitting test. The contour of the sample, including the pre-notch, is shown in cyan. The wedge, cylinders and blocks used to apply load are highlighted in white, blue and purple, respectively. The vertical groove in order to guide the crack vertically is shown with the dashed red line. The splitting displacement $\Delta\delta$ corresponds to the difference of the mean displacement of the two yellow boxes. The thickness of the specimen is 72.5 mm. All dimensions are expressed in mm.

The Young's modulus (E) and Poisson's ratio used for the investigated methods are equal to 17 GPa (measured by the bar resonance method [35]) and 0.2, respectively. The test was driven by setting the velocity of the machine actuator to 1.3 μm/s, and 313 pictures were taken for both faces of the specimen at a rate of one picture each 8 s. The images were simultaneously acquired with two Canon T5 cameras with 28-135 mm lenses, with the illumination provided by LEDs. The 16-bit picture definitions are 2601 $\times$ 1733 pixels, with a dynamic range of approximately 60,000 gray levels. The imaged physical size of one pixel was 62 μm. A random speckle pattern was sprayed onto the specimen surfaces to increase the image contrast and improve the DIC resolutions.

The 5-cycle loading curve of the experiment, which corresponds to the vertical force F_v vs. vertical actuator displacement Δh, is shown in Figure 2. Further information on this test can be found in Ref. [27], and further characterization of the studied material, processing and microstructure in Refs. [36, 37].

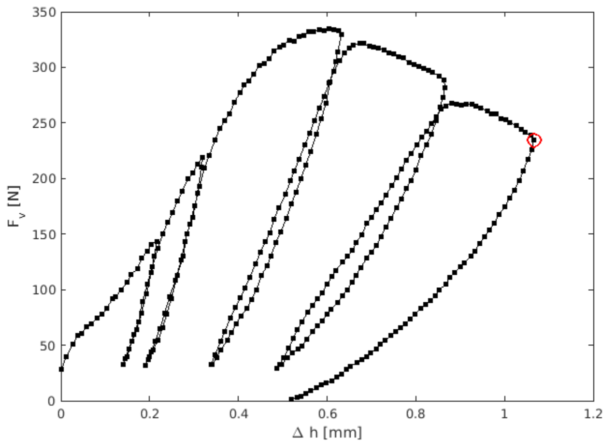

Figure 2: Loading history for the test analyzed in Section 4. Each point represents two image acquisitions (one per face) performed during the test for DIC analyses. The red circle depicts the picture acquisitions used to evaluate the strain fields shown in Figure 3.

2.2. Digital Image Correlation

In global DIC, the displacement fields $\mathbf{u}(\mathbf{x})$ are measured by minimizing the L2-norm of the gray level residuals, ϕ^2, between the image of the reference state f, and at the deformed state g

$$\phi^2 = \sum_{\text{ROI}} \left[f(\mathbf{x}) - g(\mathbf{x} + \mathbf{u}(\mathbf{x}))\right]^2 . \tag{1}$$

Searching for displacements at the pixel level is an ill-posed problem [38]. Parameterizations of the sought displacement $\mathbf{u}$ are used to regularize this problem and render the solution less affected by the acquisition noise

$$\mathbf{u}(\mathbf{x}) = \sum_{i=1}^{N} \upsilon_i \boldsymbol{\Psi}_i(\mathbf{x}), \tag{2}$$

in which υ_i are the degrees of freedom, and $\boldsymbol{\Psi}$ shape functions (*i.e.,* vector fields) that combine the displacement of a group of pixels in order to make the problem well-posed. The solution becomes

$$\{\boldsymbol{\upsilon}_{\text{DIC}}\} = \arg\min_{\{\boldsymbol{\upsilon}\}} \phi^2(\{\boldsymbol{\upsilon}\}), \tag{3}$$

where $\{\upsilon_{\text{DIC}}\}$ is the column vector gathering all amplitudes υ_i. If the actual kinematics of the problem is not well known a priori, $\boldsymbol{\Psi}_i$ can be chosen as finite element shape functions [39]. In the present case, the DIC procedure is performed with 3-noded linear elements based on finite element discretization [40] and will be referred as T3DIC. In global approaches, the quality of the registration can be evaluated pixel-wise by computing the gray level residuals

$$\rho_{\text{T3}} = f(\mathbf{x}) - g\left(\mathbf{x} + \boldsymbol{\Psi}_{\text{T3}}(\mathbf{x}, \{\boldsymbol{\upsilon}_{\text{T3}}\})\right), \tag{4}$$

where $\boldsymbol{\Psi}_{\text{T3}}$ is the vector containing the shape functions converting nodal to pixel displacements, which depends linearly on the amplitude $\{\boldsymbol{\upsilon}_{\text{T3}}\}$. In the present case, the T3DIC mesh is composed of 3-noded elements whose average edge length is equal to 58 pixels (or 3.6 mm).

In the following, the global residual of DIC approaches will be compared. It is defined as the root-mean-square (RMS) gray level residual over the considered ROI

$$\overline{\rho}_{\text{T3}} = \frac{RMS(\rho_{\text{T3}})}{\Delta f}, \tag{5}$$

where Δf is the dynamic range of the picture of the reference configuration

$$\Delta f = \max_{\text{ROI}} f - \min_{\text{ROI}} f \approx 60,000 \text{ gray levels.} \tag{6}$$

The first step of any of the methods presented hereafter is to run T3DIC. It provides displacement fields that can be compared with FE analyses, but also allows the crack path to be chosen for integrated DIC [27]. The maximum *eigen* strain field is selected in order to check the validity of the straight crack propagation assumption and the presence of a single macro-crack. The two faces of the sample are analyzed with a very fine mesh of average element length of 8.5 pixels (or 530 μm). Figure 3 shows the results for both faces for the last image before the final unloading (Figure 2). The standard uncertainty of the maximum eigen strain is of the order of 3×10^{-4} and the minimum strain level in the color bars of Figure 3 is set to 3 times this value. It was determined by correlating the two pictures shot for the reference configuration on each face. Only one unique macro-crack is observed (guided by the groove).

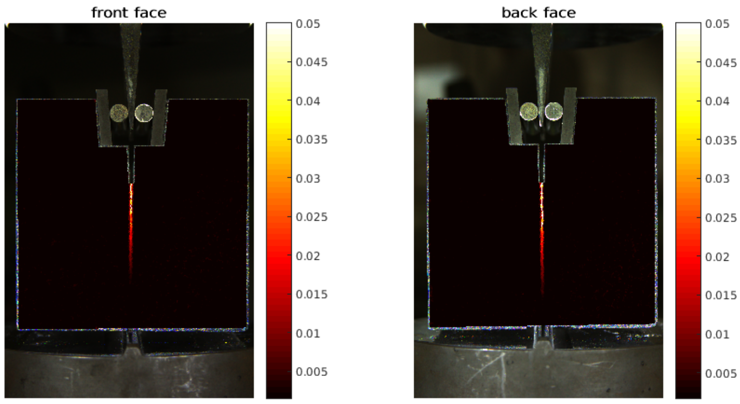

Figure 3: Maximum eigen strain fields for both analyzed faces for the image before the 5th unloading. No macro-crack branches are seen and consequently, the hypothesis of a straight crack propagation guided by the groove can be made.

2.3. Method 1: Finite Element Model Updating

The methodology described in this section is an adaptation of that proposed in Ref. [30] to the WST. DIC results are taken as Dirichlet boundary conditions and FE formulation computes the displacement field over the considered surface. The crack tip position is identified as the one that provides the best fit between the simulated and measured displacement fields. The main idea of the method is schematically shown in Figure 4, where the outer contour of T3DIC measurements, represented in green, are prescribed to the FE model, and internal nodes (blue region) are used for comparison with FE analyses. Several crack tip positions are tested along the groove region (red dashed line), and the one that gives the least root mean squared displacement gap is considered the best estimate and thus, chosen as the crack tip position for the considered image. The method is then repeated for every image taken during the test. It will be referred to as FEMU henceforth.

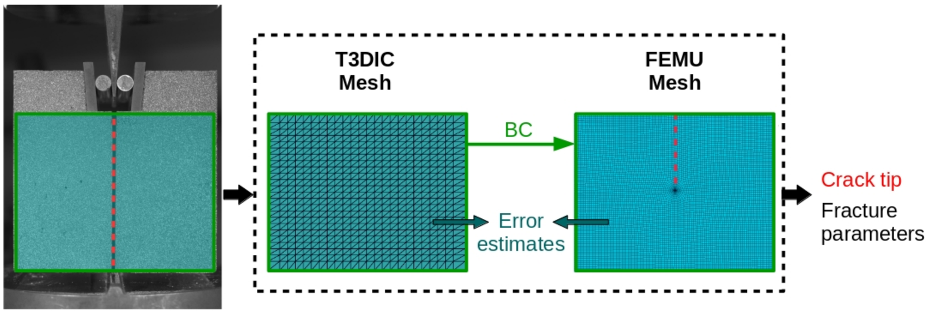

Figure 4: Adaptation of methodology introduced in Ref. [30] to the WST. An area around the propagation path is chosen and the displacements measured by T3DIC at the outer boundaries (green) are used as boundary conditions. The internal measured displacements (blue) are used for comparison with FE outputs, and the crack tip position is tested in the groove region (red).

It is important to highlight that such a procedure is run for *each* image taken during the experiment, so that one crack tip position is obtained for each considered step time. Within an FE code, it is generally possible to calculate quantities such as the mode I and II SIFs K_I, K_{II}, and the T-stress [41]. Thus the change of these fracture mechanics parameters is evaluated for each analyzed crack length. Given the thickness of the sample, a plane strain hypothesis is considered in this paper for all the reported analyses.

The FEMU displacements and mesh are exported and interpolated onto the T3DIC mesh. The nodal displacement difference between T3DIC and FE analyses is computed, and the displacement gap consists in the RMS difference

$$\phi_u^2 = \sum_{i=1}^{N} \left(\upsilon_i^{\text{FEMU}} - \upsilon_i^{\text{T3}}\right)^2 , \tag{7}$$

in which υ_i are nodal displacements. The superscript indicates if the displacements are obtained from FEMU or T3DIC analyses. It is worth noting that the gap estimate proposed in Equation (7) considers the same influence from every considered node. This definition may be improved using the T3DIC Hessian to augment the weight on nodes with respect to lower measurement uncertainties [42]. Once different crack positions are tested, the one that provides the minimum ϕ_u is taken as the estimated crack tip position, and the fracture mechanics properties are assessed with this configuration.

Although ϕ_u^2 is considered for crack tip identification, the gray level residual ρ_{FEMU} can be computed using the nodal displacements of the FE model $\{\boldsymbol{\upsilon}_{\text{FE}}\}$

$$\rho_{\text{FEMU}} = f(\mathbf{x}) - g\left(\mathbf{x} + \mathbf{\Psi}_{\text{FE}}(\mathbf{x}, \{\boldsymbol{\upsilon}_{\text{FE}}\})\right), \tag{8}$$

where $\mathbf{\Psi}_{\text{FE}}$ is the vector containing the shape functions converting nodal to pixel displacements, which is linearly dependent on the measured degrees of freedom $\{\boldsymbol{\upsilon}_{\text{FE}}\}$. The corresponding global residual reads

$$\overline{\rho}_{\text{FEMU}} = \frac{RMS(\rho_{\text{FEMU}})}{\Delta f}. \tag{9}$$

It will be compared with T3DIC results and the following integrated method.

2.4. Method 2: Integrated DIC

This section summarizes the methodology used to analyze a wedge splitting test with Integrated-DIC [27] using a closed-form solution. Williams' series [28] describe the kinematics in this case, and the gray level residual is minimized (Equation 1), instead of the displacement gap for FEMU (Equation (7)). The sought displacement field reads

$$\mathbf{u}(\mathbf{z}) = \sum_{j=I}^{II} \sum_{n=p_i}^{p_f} \omega_n^j \boldsymbol{\psi}_n^j(\mathbf{z}), \tag{10}$$

where the vector fields are defined in the complex plane

$$\mathbf{z} = (x - x_c) + (y - y_c)i = r\exp(i\theta), \tag{11}$$

where (x_c, y_c) are the coordinates of the crack tip position, $j = I$ is related to the mode I (opening) regime and $j = II$ to mode II (shearing). The amplitudes ω_n^j become the unknown kinematic degrees of freedom of IDIC. The corresponding displacement fields are described by

$$\boldsymbol{\psi}_n^I = \frac{A(n)}{2\mu\sqrt{2\pi}} r^{n/2}\left[\kappa\exp\left(\frac{in\theta}{2}\right) - \frac{n}{2}\exp\left(\frac{i(4-n)\theta}{2}\right) + \left((-1)^n + \frac{n}{2}\right)\exp\left(-\frac{in\theta}{2}\right)\right], \tag{12}$$

and

$$\boldsymbol{\psi}_n^{II} = \frac{iA(n)}{2\mu\sqrt{2\pi}} r^{n/2}\left[\kappa\exp\left(\frac{in\theta}{2}\right) + \frac{n}{2}\exp\left(\frac{i(4-n)\theta}{2}\right) + \left((-1)^n - \frac{n}{2}\right)\exp\left(-\frac{in\theta}{2}\right)\right], \tag{13}$$

where κ is equal to $(3-\nu)/(1+\nu)$ for plane stress states or $3-4\nu$ for plane strain states, ν the Poisson's ratio and $A(n)$ is defined by

$$A(n) = \cos\left(\frac{n\pi}{2}\right)^2 + \sin\left(\frac{n\pi}{2}\right). \tag{14}$$

The amplitude ω_1^j gives access to Stress Intensity Factors (SIFs), the amplitude ω_2^I provides the T-stress (positive in compressive) and ω_2^{II} the rigid body rotation. Higher order fields account for deviations from the theoretical assumption of an infinite medium [34]. With the use of two additional terms in the series, namely using $p_i = 0$, ω_0^I and ω_0^{II} are related to rigid body translations.

Although not usual, negative values of p_i can help to account for nonlinearities [34, 30]. It can be seen from Equations (12) and (13) that for negative values of n, super-singular solutions arise near the crack tip ($r = 0$). They are also important to locate the crack tip position, especially ω_{-1}^I. With the assumption that the crack tip is perturbed by a small distance d, along with some recursive properties of the Williams' series [33], it is possible to derive the offset

$$d = \frac{2\omega_{-1}^I}{\omega_1^I}, \tag{15}$$

which provides an estimation of crack tip shift to find the correct solution. In the sequel, $p_i = -3$ is taken to account for nonlinearities [34]. The maximum value $p_f = 8$ is chosen after a convergence analysis [27]. A normalization of $\mathbf{\Psi}$ is also performed in order to decrease floating point rounding errors.

The pacman-like ROI used for IDIC[1] is shown in Figure 5. An opening of 40 pixels (pacman mouth) is taken in order not to consider the cracked mouth. The Williams' series are projected onto an FE mesh to allow the use of the same FE-DIC code as used in the previous section. This mesh is chosen sufficiently fine not to influence the results. (A convergence study was performed to check this statement.)

[1]This ROI is always centered about the evaluated crack tip position

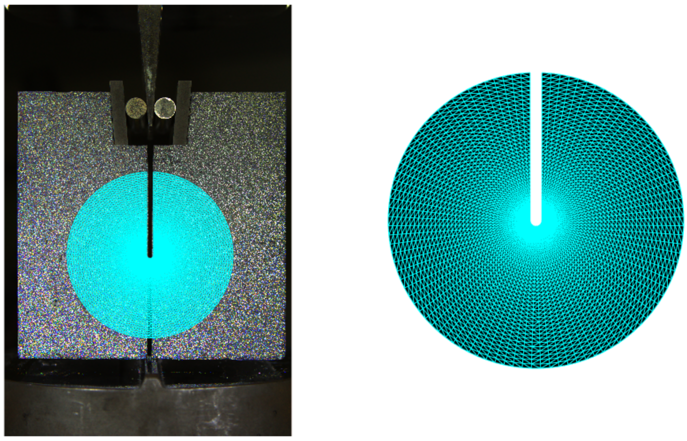

Figure 5: Example of the pacman-like mesh used in IDIC analyses.

The procedure to find the crack tip positions and the mechanical parameters of the fracture process can be summarized in the present steps:

1. A crack path is first defined as a straight line, in the groove region of the photographed sample face (Figure 4), as proved by the analysis of the maximum eigen strain fields (Figure 3);
2. The parameters defining the truncation of Williams' series are chosen, *i.e.,* $p_i = -3$, $p_f = 8$, the radius for normalization and mesh parameters;
3. The calculation is initialized for the crack position assumed to be located at the notch root;
4. An optimization algorithm evaluates the amplitudes $\{\boldsymbol{\omega}\}$ that decrease the global gray level residual [20];
5. The crack tip position is updated using Equation (15);
6. Steps 4 and 5 are repeated until convergence (*i.e.,* $d < 0.1$ pixel).

After convergence, the corresponding gray level residual field is stored

$$\rho_{\text{IDIC}} = f(\mathbf{x}) - g\left(\mathbf{x} + \boldsymbol{\Psi}_{\text{IDIC}}(\mathbf{x}, \{\boldsymbol{\omega}\})\right), \tag{16}$$

where $\{\boldsymbol{\omega}\}$ gathers all converged ω_n^j amplitudes (see Equation (10)), and $\boldsymbol{\Psi}_{\text{IDIC}}$ are the shape functions described in Equations (12) and (13) evaluated for each pixel position $\mathbf{x}$. From this information, the global IDIC residual becomes

$$\overline{\rho}_{\text{IDIC}} = \frac{RMS(\rho_{\text{IDIC}})}{\Delta f}. \quad (17)$$

This methodology will be referred to as IDIC in Section 4.

3. Analysis of a virtual experiment

First, a virtual experiment is considered to test both approaches on a configuration for which the exact solution is known. It is discussed how to deform a reference image with displacements obtained from numerical simulations (*e.g.,* *Abaqus*^{TM}). In the sequel, this virtually deformed image is then analyzed using the previous two methods. This virtual experiment will be referred to as VE in Section 3.2

3.1. Virtual experiment

A sketch following the instructions from Ref. [9] (width = 100 mm and height = 100 mm) is performed in *Abaqus*^{TM}, with some adjustments such as the depth of the extrusion set to 72.5 mm related to the sample geometry [27]. The numerical model is presented in Figure 6. Normal pressure was applied to the vertical faces onto which the rollers would apply the load. The line at the bottom of the sample does not move in the x and y-directions. In the z-direction, one single point has no motion. A straight crack is added and its tip is located in the middle of the crack propagation path of the sample (*i.e.,* only one loading step is considered). The mesh is refined around the crack tip. A 2D mesh is extracted from the image plane presented in Figure 6 to consider a plane strain state. K_I, K_{II}, and the T-stress measurements at this plane are considered.

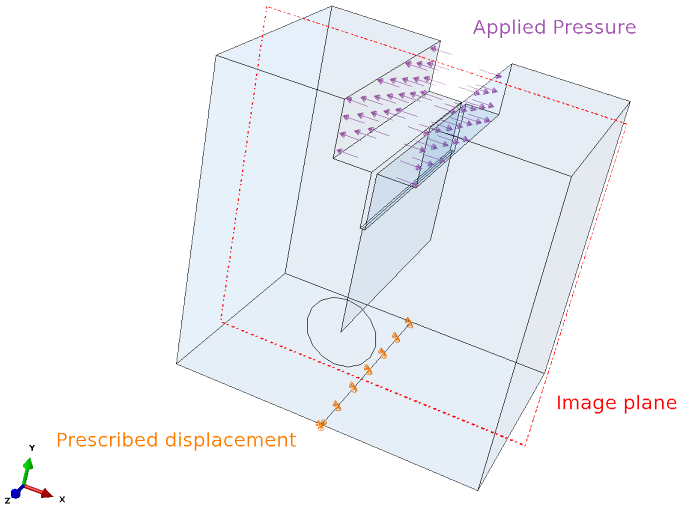

Figure 6: 3D $Abaqus^{TM}$ model showing the applied pressure and the prescribed displacements. It is also possible to see the partition lines in the middle of the crack propagation path. The used image plane is also shown.

For the present study, a reference image is also required. An *actual* image that shows the whole sample surface [27] is used in the sequel. The 2D mesh is extracted and interpolated onto pixel coordinates such that it fits the sample in the image, as shown in Figure 7.

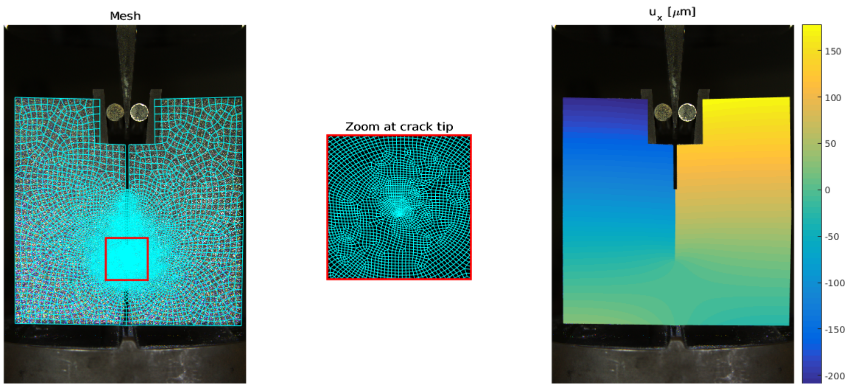

Figure 7: Superposition of 2D mesh extracted from the 3D $Abaqus^{TM}$ mesh for the reference image (on the left), with a zoom about the crack tip (on the middle). Horizontal displacements u_x (expressed in μm) (on the right) in the virtual experiment.

Once the displacement field for each pixel is known, the deformed image is created. In DIC the gray level conservation reads

$$f(\mathbf{x}) = g(\mathbf{x} + \mathbf{u}(\mathbf{x})), \tag{18}$$

in which $\mathbf{x}$ contains integer pixel coordinates in the reference image. However the position $\mathbf{x}+\mathbf{u}(\mathbf{x}) = \boldsymbol{\theta}(\mathbf{x})$ is not necessarily an integer. The evaluation of $g(\boldsymbol{\theta}(\mathbf{x}))$, which corresponds to the picture of the deformed configuration corrected by the displacement field $\mathbf{u}$, requires an interpolation scheme of the gray levels. In the present case, an inverse mapping is required, namely, integer valued positions $\mathbf{x}_g$ are sought to construct the picture in the deformed configuration g. Consequently, the position $\boldsymbol{\theta}^{-1}(\mathbf{x}_g)$ has to be determined for computing the gray level $f(\boldsymbol{\theta}^{-1}(\mathbf{x}_g))$, which also requires an interpolation scheme [43].

To be more representative of a real experiment, it is chosen to add real noise to the deformed image. The gray level residual from T3DIC results for the first deformed image of the front face is added to the artificially deformed image. The global residual is equal to 0.57%. This residual at the beginning of the test is considered to be a good approximation of the noise during the test since the load was small and no crack propagation had yet occurred.

3.2. Results

The results obtained from the VE analysis with different methods are gathered in Table 1. The global residuals, $\overline{\rho}_{\text{method}}$, in which *method* is replaced by VE, FEMU or IDIC, are assessed by correcting the image in the deformed configuration g with the corresponding displacement fields (see Section 3.1, Equations (8) and (16), respectively). For consistency along the discussion, all the reported residuals are calculated in a pacman-shaped area centered about the crack tip position for the discussed *method* (see Figure 5).

Table 1: Virtual experiment results. Calibrated fracture mechanics parameters and corresponding global gray level residuals.

	Δa [mm]	K_I [MPa$\sqrt{\text{m}}$]	K_{II} [MPa$\sqrt{\text{m}}$]	T-stress [MPa]	$\overline{\rho}_{\text{method}}$ [$\%\Delta f$]	$\overline{\rho}^{\text{T3}}_{\text{method}}$ [$\%\Delta f$]	$\Delta\overline{\rho}^{\text{T3}}_{\text{method}}$ [$\%\Delta f$]
VE (Sect. 3.1)	36.0	3.8	3×10^{-4}	6.4	1.68	2.45	-0.77
FEMU (Sect. 2.3)	38.9	3.1	3×10^{-3}	7.8	2.52	2.46	0.06
IDIC (Sect. 2.4)	36.4	3.9	-6×10^{-2}	8.8	2.48	2.45	0.03

The fact that the residuals for the exact solution are not vanishing is due to the added noise to g and gray level interpolation inaccuracies. Consequently, $\overline{\rho}_{\text{VE}}$ defines the minimum level that can be achieved. Both methodologies (*i.e.,* FEMU and IDIC) are consistent with the exact (*i.e.,* VE) solution since the gray level residuals ($\overline{\rho}_{\text{FEMU}}$ and $\overline{\rho}_{\text{IDIC}}$) are only 1.5 times higher than the minimum level ($\overline{\rho}_{\text{VE}}$), and that their difference is very small with a value that is slightly lower for IDIC. The later better predicts the crack tip position (Δa in Table 1) and mode I SIF for an elastic body with a single crack, while the usage of the FEMU procedures provides T-stress levels more accurately. Mode II SIF is believed to be close to the resolution for both methods.

Since the exact solution is known in the present case, the discussion could stop here. However, in an actual experiment, the exact solution is unknown. Since the ROIs of each method are not located at the same position in the reference image, the crack tip locations predicted by both methods are expected to be different. T3DIC will thus be used to independently assess global residuals computed over the same ROI as those in the considered *method*s. Since in T3DIC no mechanics-based assumptions are made on the displacement fields apart from their continuity,[2] the global residuals $\overline{\rho}^{\text{T3}}_{\text{method}}$ for the same ROI of each *method* are also evaluated. The difference in global residuals

$$\Delta\overline{\rho}^{\text{T3}}_{\text{method}} = \overline{\rho}_{\text{method}} - \overline{\rho}^{\text{T3}}_{\text{method}} \tag{19}$$

[2]Note that the cracked area is masked by the pacman mouth (Figure 5)

then assesses the overall identification quality (*i.e.,* $\overline{\rho}^{\mathrm{T3}}_{\mathrm{method}}$ is thus taken as the reference) and the smaller $\overline{\rho}^{\mathrm{T3}}_{\mathrm{method}}$, the better the identification result.

Table 1 shows that $\overline{\rho}^{\mathrm{T3}}_{\mathrm{method}}$ is virtually identical for the three methods. This is expected since this virtual case only involves noise and gray level interpolation inaccuracies. The fact that $\overline{\rho}^{\mathrm{T3}}_{\mathrm{VE}}$ is greater than $\overline{\rho}_{\mathrm{VE}}$ is due to the T3DIC mesh that is rather coarse. This choice was made since very small displacements are sought (see below) and a finer mesh would have induced higher measurement uncertainties [44]. This choice also explains why $\Delta\overline{\rho}^{\mathrm{T3}}_{\mathrm{VE}} < 0$. Had a finer mesh been used, T3DIC would be expected to be closer to the VE solution. Furthermore, $\overline{\rho}^{\mathrm{T3}}_{\mathrm{FEMU}}$ is slightly higher than $\overline{\rho}^{\mathrm{T3}}_{\mathrm{IDIC}}$, and more importantly, IDIC is closer to T3DIC than FEMU (*i.e.,* $\Delta\overline{\rho}^{\mathrm{T3}}_{\mathrm{IDIC}} = 0.03\%$ in comparison with $\Delta\overline{\rho}^{\mathrm{T3}}_{\mathrm{FEMU}} = 0.06\%$). The difference between both methods remains very small, which validates both procedures. However, IDIC slightly outperformed FEMU in the present analysis.

4. Experimental study

The two methodologies described in Sections 2.3 and 2.4 are now applied to one wedge splitting test. Figure 8 shows the crack tip position for the first part of the experiment during which the crack has propagated. $\Delta a = 0$ considers the crack tip to be located at the pre-notch root. Both methodologies have high uncertainties for the first two cycles, which are related to very small displacement ranges (*i.e.,* 0.15 pixel, or 9 μm at the most). It is observed that FEMU identifies smaller crack lengths than IDIC. It is worth noting that both methodologies predict different crack propagation histories on the two analyzed faces and that, in the end, the crack propagated farther on the back face (Figure 3).

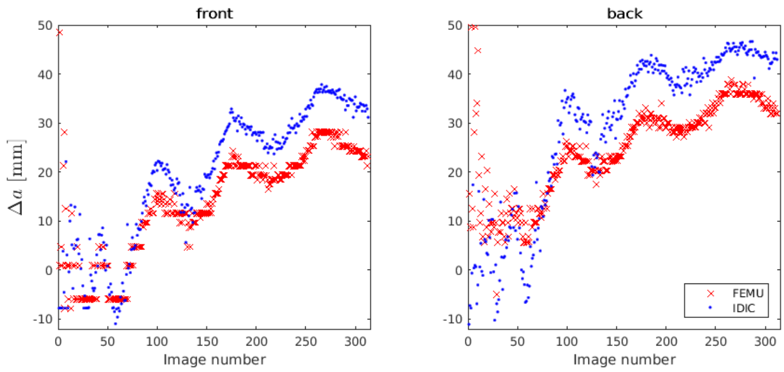

Figure 8: Crack tip position for front and back faces with both methodologies for the first 312 images acquired during the analyzed wedge splitting test.

Two features in Figure 8 need to be further commented. First, the negative values of Δa at the beginning of the experiment, namely, a crack tip position out of the sample, and second, the crack closure in the unloading phase of each cycle. These observations do not mean that crack healing occurs in the present case. It is believed that the negative values are due to the uncertainties associated with crack tip positioning when the displacement levels are very small (*i.e.,* at the beginning of the experiment). The crack tip itself is a feature associated with the considered fracture mechanics model (here defined with Williams' series or finite element simulations). Although the main conclusions of this work will not be affected, physically, crack propagation is believed to be stopped during unloading phases, and restarts once it reached a critical SIF level in the subsequent loading cycle.

The SIFs are reported in Figure 9. For this case in which a single macro-crack propagates guided by the groove (Figure 3), pure mode I is expected and is confirmed by both approaches. As K_{II} is close to zero, it can be used as an evaluation of the resolution for SIF evaluations. The RMS of K_{II} values measured by both methodologies and at both faces is of the order of 3×10^{-2} MPa$\sqrt{\text{m}}$. The general tendency observed for K_I is opposite in comparison with estimates of crack tip positions, namely, lower K_I levels and larger crack lengths are reported by IDIC in comparison to FEMU results. However, crack tip positions and SIFs values obtained by both techniques are of the same order of magnitude.

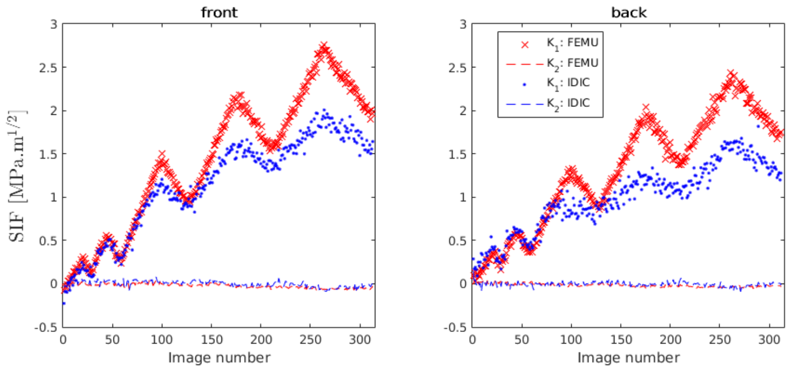

Figure 9: Mode I and II SIF histories for both faces with both approaches.

The T-stress histories are shown in Figure 10. The levels obtained via IDIC are generally higher, predominantly after the second cycle and for the front face. For the back face, the values are closer. The fluctuations could be related to mechanical features since some fluctuation were also observed on the load vs. crack mouth opening displacement curve for this test [27], but further studies are needed to confirm this hypothesis.

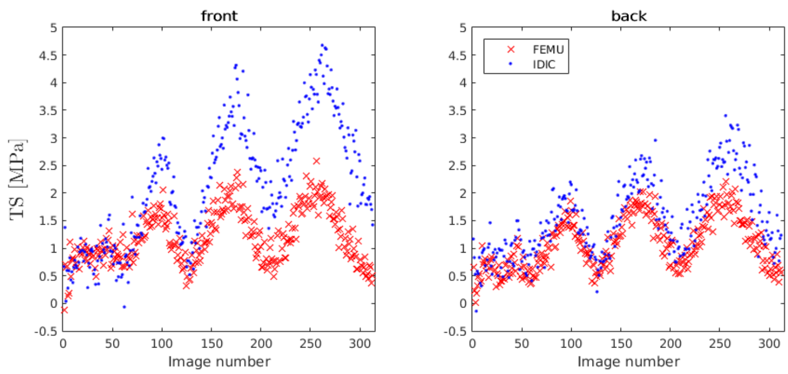

Figure 10: T-stresses measured with both methodologies for both faces.

In order to have an absolute evaluation of the quality of both approaches $\overline{\rho}_{\text{FEMU}}$ and $\overline{\rho}_{\text{IDIC}}$ are reported. This type of analysis is no longer an inter comparison, but probes the individual merit of each technique with respect to the pictures acquired during the experiment with the same number of pixels. The

RMS gray level residuals are reported in Figure 11. The overall levels remain very small for the whole sequence, which validates the reported results. For both cases, increasing residuals occur with crack propagation. The longer the crack, the bigger the fracture process zone and the assumption of an elastic medium is presumably less true. Further, 3D effects may also be more pronounced [45], which make the 2D assumptions used in Williams' series and FE calculations less accurate.

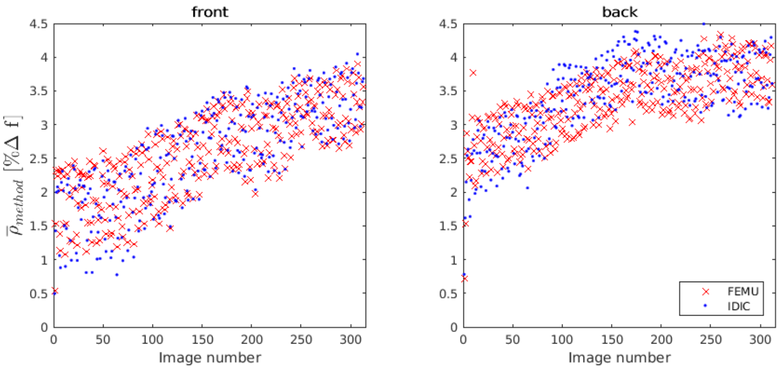

Figure 11: Dimensionless residuals for the two methods (FEMU and IDIC) and both faces.

To compare in a more quantitative way the two procedures the residual difference, $\Delta\overline{\rho}$, is computed

$$\Delta\overline{\rho} = \overline{\rho}_{\mathrm{IDIC}} - \overline{\rho}_{\mathrm{FEMU}} \tag{20}$$

Plots of $\Delta\overline{\rho}$ for both faces of the sample are shown in Figure 12. The differences are in 0.2% range, which is lower than the acquisition noise for these images (*i.e.*, ≈ 0.6%). However, IDIC shows lower residuals at the beginning the test. The crack tip position is better captured (Figure 8), even though the SIF levels are rather consistent with both approaches (Figure 9). The fact that IDIC becomes less accurate than FEMU at the end of the propagation step may be related to the Williams' series not describing the boundary effects as the crack tip approaches the sample edge.

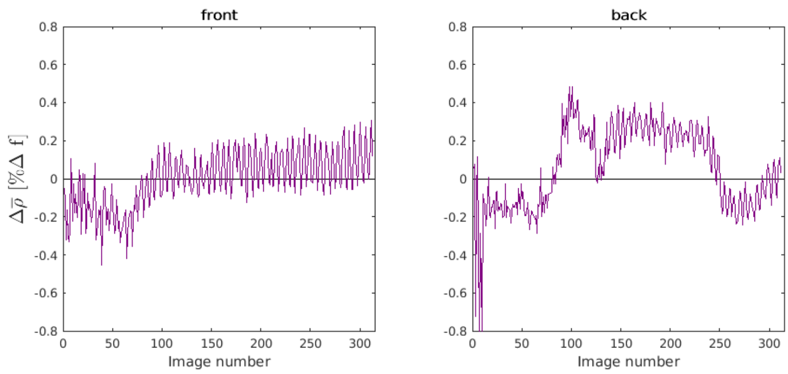

Figure 12: Residual difference for both faces. A negative (resp. positive) value corresponds to a more faithful evaluation via IDIC (resp. FEMU).

The residuals reported in Figure 11 and 12 were calculated for the same ROI size but centered about different crack tip positions (Figure 8). In a virtual experiment $\overline{\rho}^{\mathrm{T3}}_{\mathrm{method}}$ does not change considerably in different regions as reported in Table 1. In an actual experiment, not only slightly different image features at each ROI but also images artifacts such as lighting changes and lens focus may affect $\overline{\rho}^{\mathrm{T3}}_{\mathrm{method}}$. The residual difference $\Delta\overline{\rho}^{T3}_{\mathrm{method}}$ (see Equation (19)) is shown in Figure 13 and indicates how close each *method* was close to T3DIC. IDIC residuals are closer to T3DIC than FEMU. Small negative values seen for IDIC and FEMU in some images indicate that they outperformed T3DIC, which can be explained by the non-optimal T3DIC mesh. Although the residuals for both methodologies are in the same range (Figure 12), the ROIs in which FEMU converged were presumably less affected by image artifacts and the residuals were farther from T3DIC residuals.

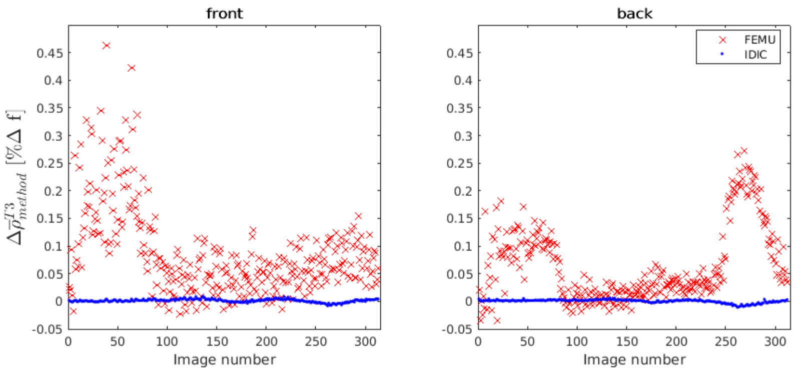

Figure 13: Differences from IDIC and FEMU residuals in comparison with T3DIC. Positive values are related to smaller residuals measured with T3DIC.

The main conclusion when considering different regions separately (Figure11 and 12) is that IDIC was performing better at the very beginning and then FEMU would be preferred for the rest of the test. However, using $\overline{\rho}_{\text{method}}^{\text{T3}}$ as a reference (Figure 13) in order to account for image artifacts and textures on different regions, the conclusion is that, for the present case, IDIC is more accurate for the whole analysis.

Last, even though very small, K_{II} is considered to analyze the R-curve behavior defined as

$$R = \frac{K_I^2 + K_{II}^2}{E}(1 - \nu^2) \tag{21}$$

in a plane strain state, as considered in FEMU and IDIC. It is worth noting that although some deviation from linear elasticity may occur, the effective crack tip is measured with full-field approaches accounting for elasticity. In such cases, with the effective instead of visible crack tips, Equation (21) can be applied [46].

The R-curve is then plotted as a function of crack tip position in Figure 14. It shows that energy consumption increases as the crack propagates (with a steeper slope for FEMU), which is related to extrinsic toughening mechanisms such as crack branching, microcracking or bridges between aggregates [47]. In the present case, it was checked that crack branching was not occurring out of the groove in the photographed surface of sample, at the scale of DIC measurements (see Figure 3), namely, of the order of the element length (*i.e.,* ≈ 0.5 mm).

With the chosen magnification, the main purpose of DIC was to analyze the macroscopic fracture mechanics parameters, *i.e.,* R-curve behavior , and could resolve the effect of the toughening mechanisms occurring at lower scales. The observed R-curve behavior may indicate crack branching, and although not seen on the strain fields reported in Figure 3, it may take place in the bulk of the material. For checking such mechanisms, in situ tomographies analyzed with Digital Volume Correlation would be a suitable approach [48].

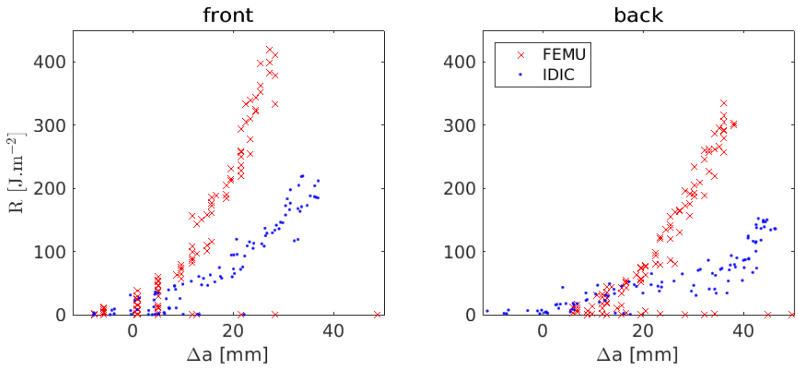

Figure 14: R vs. crack length for both faces with both approaches. Images taken during unloading steps are not accounted for the computation of R.

The present study enables to assess uncertainties associated with the use of two different identification techniques. The latter ones provided results that were both considered as realistic and may be used when comparing crack propagation in different materials compositions, for instance. However, they led to significant differences in the crack propagation resistance curve of the investigated material (Figure 14). Thanks to the use of gray level residuals, the merit of both techniques could be assessed, but more importantly it could be decided which one was more trustworthy (*i.e.,* IDIC in the present case).

In order to validate the R-curves reported in Figure 14, a last study is performed. First, the loading history shown in Figure 2 may be integrated to estimate the fracture energy, $\gamma_{wof(v)}$

$$\gamma_{wof(v)}^{\text{method}} = \frac{1}{2A^{\text{method}}} \int_{\Delta h_0}^{\Delta h_f} F_v \; d(\Delta h) \tag{22}$$

where the interval $[\Delta h_0, \Delta h_f]$ corresponds to the loading envelope and the final unloading, Δh is the vertical displacement of the actuator, F_v the vertical force, and method is substituted by IDIC or FEMU for the evaluation of the cracked area A. The latter is considered as the maximum crack length (Δa_{max} for last point before final unloading) obtained for the method (IDIC or FEMU) multiplied by the thickness t_g of the specimen inside the groove (*i.e.,* 65 mm). It is worth noting that $\gamma_{wof(v)}$ corresponds to an *upper bound* since it includes dissipated energy through friction of the loading parts.

The splitting force F_h vs. displacement $\Delta\delta$ curves are shown in Figure 15, in which the splitting displacement $\Delta\delta$ is measured from T3DIC results at the locations shown in Figure 1, namely, at the same height as the splitting forces are applied.

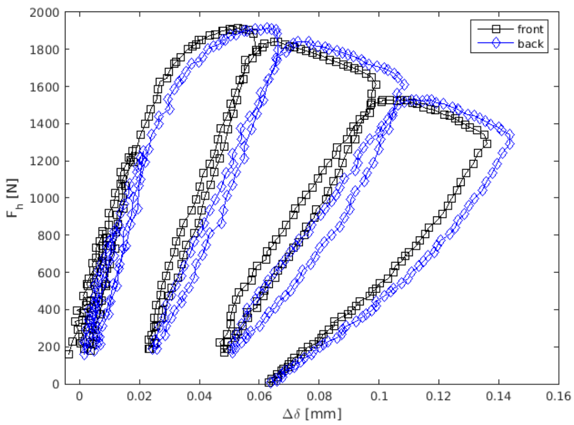

Figure 15: Splitting force (*i.e.,* 5.715 times the vertical force) versus splitting displacement $\Delta\delta$ measured at the locations shown in Figure 1.

By integrating the data shown in Figure 15, the fracture energy γ_{wof} reads

$$\gamma_{wof}^{\text{method}} = \frac{1}{2A^{\text{method}}} \int_{\Delta\delta_0}^{\Delta\delta_f} F_h \; d\left(\Delta\delta\right) \tag{23}$$

where the interval $[\Delta\delta_0, \Delta\delta_f]$ corresponds to the loading envelope and the final unloading. In the present case, the DIC extensometry only accounts for the work performed on the specimen itself, thus is more representative of the work of fracture of the studied material.

To calculate the average of R, which is denoted by $\overline{R}$, for IDIC and FEMU the R-curves shown in Figure 14 are integrated

$$\overline{R}^{\text{method}} = \frac{1}{\Delta a_{max}} \int_{\Delta a_0}^{\Delta a_{max}} R^{\text{method}} \, d\left(\Delta a^{\text{method}}\right) \tag{24}$$

Since the dissipated energy is consumed to create two cracked surfaces, $\overline{R} = 2\gamma_{wof(h)}$ [49].

The calculated energies are listed in Table 2. All reported values are expected to underestimate the fracture energy measured for the full crack propagation (with same methodology), which is not accessible in the experiment reported herein. The fracture energies have the same order of magnitude, which is a further validation of the R-curves predicted with IDIC and FEMU. However, IDIC predicts values that are closer to those obtained with DIC extensometry than FEMU. FEMU even provides estimates above the upper bound (*i.e.*, $\gamma_{wof(v)}$).

Table 2: Fracture energies (expressed in J/m^2) calculated with different approaches.

	Fract. energy	front	back	mean
FEMU	$2\gamma_{wof(v)}$	114	83	99
	$2\gamma_{wof}$	92	71	82
	$\overline{R}$	162	97	130
IDIC	$2\gamma_{wof(v)}$	85	69	77
	$2\gamma_{wof}$	69	60	64
	$\overline{R}$	84	52	68

Even though FEMU and IDIC results are in the same range for the various quantities reported in the present section, IDIC results are more consistent with experimental data in terms of gray level residuals, but even more importantly when compared with independent estimates of fracture energies. For the latter ones, it is shown that about 20% is dissipated by friction when the upper bound estimate is compared with that derived from the splitting force vs. displacement data, or equivalently by R-curves provided by IDIC.

5. Conclusions

The FEMU methodology [30] was adapted to analyze WSTs. An automated procedure was implemented to create an FE model with Dirichlet boundary conditions measured via T3DIC analyses. The crack tip position was identified, among several tested positions, as the one that provided the best kinematic fit. Interaction integrals of the FE code were used to estimate fracture-related properties (*i.e.,* SIFs and T-stress). This approach was compared with IDIC when applied to a WST [27]. First, a virtual experiment was analyzed, then followed by experimental analyses for both faces of a refractory castable specimen.

FEMU allows for better T-stress estimates, while IDIC is more trustworthy for estimating the crack tip position and mode I SIF in the virtual experiment. Gray level residuals were used to check the merit of each technique directly with experimental pictures. FEMU residuals were farther from T3DIC than IDIC when considering T3DIC as the reference to check the quality of measurements, proving that IDIC is slightly more trustworthy than FEMU in the present case.

IDIC provides longer crack lengths coupled with lower SIFs in comparison with FEMU. Consequently, the R-curve behavior is less steep for the former. Different levels of properties on each side and measured by each method highlights the importance of such analyses performed on *both* sample faces. These differences are related to experimental imperfections such as the fine alignment of the wedge and microstructural heterogeneities.

Accessing gray level residuals is a powerful tool to check analyses with the experimental data when the actual solution is not known. It is of utmost importance to consider the measurement regions in such analyzes. IDIC residuals were closer to T3DIC resulting in more reliable measurements.

The evaluations of fracture energies were consistent with both discussed methods, namely, the same order of magnitude of the R-curves was obtained via IDIC and FEMU. When compared with FEMU, IDIC estimates were closer to those based on DIC extensometry. While IDIC was comparable to conventional methods, FEMU resulted in fracture energies greater than the experimental upper bound. All these differences show that the estimation of the crack tip location, which was different for both investigated approaches, has to be very accurate. The use of the first supersingular field in Williams' series for estimating the crack tip location via IDIC is further validated thanks to the present study.

Acknowledgments

JAR thanks CNPq for the productivity scholarship, grant #307127/2013-3. RV's stay at LMT was supported through an RIA scholarship, grant #2017/20911-9, São Paulo Research Foundation (FAPESP).

References

[1] Lee WE, Vieira W, Zhang S, Ghanbari Ahari K, Sarpoolaky H, Parr C. Castable refractory concretes. International Materials Reviews 2001;46(3):145–67.

[2] Luz AP, Braulio MAL, Pandolfelli VC. Refractory Castable Engineering; vol. 1. 1 ed.; São Carlos, SP: Göller Verlag; 2015.

[3] Lee WE, Moore RE. Evolution of in situ refractories in the 20th century. Journal of the American Ceramic Society 1998;81(6):1385–410.

[4] Studart AR. Bioinspired ceramics: Turning brittleness into toughness. Nature materials 2014;13(5):433–5.

[5] Wachtman J. Materials and Equipment - Whitewares - Refractory Ceramics - Basic Science: Ceramic Engineering and Science Proceedings, Volume 16. No. 1 in Ceramic Engineering and Science Proceedings; Wiley; 2009. ISBN 9780470316306.

[6] Tschegg E. Prüfeinrichtung zur Ermittlung von bruchmechanishen Kennwerten sowie hiefür geeignete, Prüfkörper, Austrian Pat. AT 390328B, registered. 1986.

[7] Brühwiler E, Wittmann FH. The wedge splitting test, a new method of performing stable fracture mechanics tests. Engineering Fracture Mechanics 1990;35(1-3):117–25.

[8] Harmuth H. Stability of crack propagation associated with fracture energy determined by wedge splitting specimen. Theoretical and Applied Fracture Mechanics 1995;23:103–8.

[9] Ribeiro S, Rodrigues JA. The influence of microstructure on the maximum load and fracture energy of refractory castables. Ceramics International 2010;36(1):263–74.

[10] Grasset-Bourdel R, Alzina A, Huger M, Chotard T, Emler R, Gruber D, et al. Tensile behaviour of magnesia-spinel refractories: Comparison of tensile and wedge splitting tests. Journal of the European Ceramic Society 2013;33(5):913–23.

[11] Liao N, Li Y, Wang Q, Zhu T, Jin S, Sang S, et al. Synergic effects of nano carbon sources on thermal shock resistance of Al_2O_3-C refractories. Ceramics International 2017;43(16):14380–8.

[12] Long B, Xu G, Buhr A, Jin S, Harmuth H. Fracture behaviour and microstructure of refractory materials for steel ladle purging plugs in the system Al_2O_3-MgO-CaO. Ceramics International 2017;43(13):9679–85.

[13] Zhu T, Li Y, Sang S, Xie Z. Fracture behavior of low carbon MgO–C refractories using the wedge splitting test. Journal of the European Ceramic Society 2017;37(4):1789–97.

[14] Zhu T, Li Y, Sang S, Xie Z. Mechanical behavior and thermal shock resistance of MgO-C refractories: Influence of graphite content. Ceramics International 2017;43(9):7177–83.

[15] Jin S, Gruber D, Harmuth H. Determination of Youngs modulus, fracture energy and tensile strength of refractories by inverse estimation of a wedge splitting procedure. Engineering Fracture Mechanics 2014;116:228 –36.

[16] Sutton MA. Computer vision-based, noncontacting deformation measurements in mechanics: A generational transformation. Applied Mechanics Reviews 2013;65(AMR-13-1009, 050802).

[17] McNeill S, Peters W, Sutton M. Estimation of stress intensity factor by digital image correlation. Engineering Fracture Mechanics 1987;28(1):101–12.

[18] Abanto-Bueno J, Lambros J. Investigation of crack growth in functionally graded materials using digital image correlation. Engineering Fracture Mechanics 2002;69:1695–711.

[19] Forquin P, Rota L, Charles Y, Hild F. A method to determine the toughness scatter of brittle materials. International Journal of Fracture 2004;125(1):171–87.

[20] Roux S, Hild F. Stress intensity factor measurements from digital image correlation: post-processing and integrated approaches. International Journal of Fracture 2006;140(1-4):141–57.

[21] Mathieu F, Hild F, Roux S. Identification of a crack propagation law by digital image correlation. International Journal of Fatigue 2012;36(1):146–54.

[22] Saracura RGM, Canto RB, Pandolfelli VC, Schmitt N, Hild F. Surface crack network detection on MgO-based refractory castable by digital image correlation. China's Refractories 2015;24(1):32–7.

[23] Belrhiti Y, Pop O, Germaneau A, Doumalin P, Dupré JC, Harmuth H, et al. Investigation of the impact of micro-cracks on fracture behavior of magnesia products using wedge splitting test and digital image correlation. Journal of the European Ceramic Society 2015;35(2):823–9.

[24] Dai Y, Gruber D, Harmuth H. Observation and quantification of the fracture process zone for two magnesia refractories with different brittleness. Journal of the European Ceramic Society 2017;37(6):2521–9.

[25] Dai Y, Gruber D, Harmuth H. Determination of the fracture behaviour of MgO-refractories using multi-cycle wedge splitting test and digital image correlation. Journal of the European Ceramic Society 2017;37(15):5035–43.

[26] Dupré JC, Doumalin P, Belrhiti Y, Khlifi I, Pop O, Huger M. Detection of cracks in refractory materials by an enhanced digital image correlation technique. Journal of Materials Science 2018;53(2):977–93.

[27] Vargas R, Neggers J, Canto RB, Rodrigues JA, Hild F. Analysis of wedge splitting test on refractory castable via integrated DIC. Journal of the European Ceramic Society 2016;36(16):4309–17.

[28] Williams ML. On the stress distribution at the base of a stationary crack. Journal of Applied Mechanics 1957;24(1):109–14.

[29] Rieder KA, Tschegg EK, Harmuth H. Notch sensitivity of ordinary ceramic refractory materials. Journal of Materials Science Letters 1998;17(8):675–8.

[30] Mathieu F, Aimedieu P, Guimard JM, Hild F. Identification of interlaminar fracture properties of a composite laminate using local full-field kinematic measurements and finite element simulations. Composites Part A: Applied Science and Manufacturing 2013;49:203–13.

[31] Affagard JS, Mathieu F, Guimard JM, Hild F. Identification method for the mixed mode interlaminar behavior of a thermoset composite using displacement field measurements and load data. Compos Part A 2016;91:238–49.

[32] Grédiac M, Hild F. Full-field measurements and identification in solid mechanics. John Wiley & Sons; 2012.

[33] Roux S, Réthoré J, Hild F. Digital image correlation and fracture: An advanced technique for estimating stress intensity factors of 2D and 3D cracks. Journal of Physics D: Applied Physics 2009;42:214004.

[34] Henninger C, Roux S, Hild F. Enriched kinematic fields of cracked structures. International Journal of Solids and Structures 2010;47(24):3305–16.

[35] Diógenes HJF, Cossolino LC, Pereira AHA, El Debs MK, El Debs ALHC. Determination of modulus of elasticity of concrete from the acoustic response. Revista IBRACON de Estruturas e Materiais 2011;4(5):803–13.

[36] Pereira AHA, Miyaji DY, Cabrelon MD, Medeiros J, Rodrigues JA. A study about the contibution of the α-β phase transition of quartz to thermal cycle damage of a refractory used in fluidized catalytic cracking units. Cerâmica 2014;60:449–56.

[37] Miyaji DY, Otofuji CZ, Cabrelon MD, Medeiros J, Rodrigues JA. The coke effect on the fracture energy of a refractory castable for the petrochemical industry. In: Proceedings of the Unified International Technical Conference on Refractories (UNITECR 2013). Wiley Online Library; 2014, p. 1111–6.

[38] Hild F, Roux S. Digital image correlation. In: Rastogi P, Hack E, editors. Optical Methods for Solid Mechanics. A Full-Field Approach. Weinheim (Germany): Wiley-VCH; 2012, p. 183–228.

[39] Besnard G, Hild F, Roux S. "Finite-Element" displacement fields analysis from digital images: Application to Portevin-Le Chatelier bands. Experimental Mechanics 2006;46(6):789–803.

[40] Leclerc H, Périé J, Roux S, Hild F. Integrated digital image correlation for the identification of mechanical properties; vol. LNCS 5496. Berlin (Germany): Springer; 2009, p. 161–71.

[41] Simulia . Contour integral evaluation (section 11.4.2). 2010,.

[42] Mathieu F, Leclerc H, Hild F, Roux S. Estimation of elastoplastic parameters via weighted FEMU and integrated-DIC. Experimental Mechanics 2015;55(1):105–19.

[43] Réthoré J, Muhibullah , Elguedj T, Coret M, Chaudet P, Combescure A. Robust identification of elasto-plastic constitutive law parameters from digital images using 3D kinematics. International Journal of Solids and Structures 2013;50(1):73–85.

[44] Hild F, Roux S. Digital Image Correlation. Weinheim (Germany): Wiley-VCH; 2012, p. 183–228.

[45] Réthoré J, Roux S, Hild F. Optimal and noise-robust extraction of fracture mechanics parameters from kinematic measurements. Eng Fract Mech 2011;78(9):1827–45.

[46] Bornhauser A, Kromp K, Pabst RF. R-curve evaluation with ceramic materials at elevated temperatures by an energy approach using direct observation and compliance calculation of the crack length. Journal of Materials Science 1985;20(7):2586–96.

[47] Launey ME, Ritchie RO. On the fracture toughness of advanced materials. Advanced Materials 2009;21(20):2103–10.

[48] Hild F, Bouterf A, Roux S. Damage measurements via DIC. International Journal of Fracture 2015;191(1-2):77–105.

[49] Sakai M, Bradt RC. Fracture toughness testing of brittle materials. International Materials Reviews 1993;38(2):53–78.

APPENDIX B: paper dealing with FEMU-F (Section 3.3.3)

Analysis of a castable refractory using the wedge splitting test and cohesive zone model

R. Vargas[a,], J. Neggers[b], R. B. Canto[a], J. A. Rodrigues[a], F. Hild[b]

[a] *Federal University of Sao Carlos (UFSCar)*
Graduate Program in Materials Science and Engineering
Rodovia Washington Luis, km 235, 13565-905, São Carlos-SP, Brazil
[b] *Laboratoire de Mécanique et Technologie (LMT)*
ENS Paris-Saclay, CNRS, Université Paris-Saclay
61 avenue du Président Wilson, 94235 Cachan, France

Abstract

A cohesive zone approach is applied to the Wedge Splitting Test (WST) using the finite element code Abaqus to obtain the tensile strength, the fracture energy and insight about the crack wake region. A Finite Element Model Updating (FEMU) method, with a cost function based on the measured load (FEMU-F), is used to calibrate the sought parameters. Digital Image Correlation (DIC) provided the kinematic boundary conditions, and the images were also used to define the geometry for the finite element analysis. Besides the fracture energy analysis and the experimental load, gray level images and displacement fields are analyzed in order to validate the results. The cohesive region is active in the whole analyzed test as confirmed by estimates using the cohesive length.

Keywords: Cohesive zone model, digital image correlation, finite element model updating, wedge splitting test, castable refractory

1. Introduction

Refractory castables are ceramic materials with a fine matrix and coarser aggregates, which are utilized in transformation industries such as steel making and oil refineries [1, 2, 3]. Their main goal is to ensure functional properties

*Corresponding author
Email address: hild@lmt.ens-cachan.fr (F. Hild)

at high temperatures and corrosive environments, thereby calling for complex processing of various materials [3]. In these environments with considerable thermal shocks between processing cycles, it is not optimal to prevent crack initiation [4]. The applied approach consists in tailoring the microstructure with suitable compositions to make crack propagation difficult. The most important toughening mechanisms are extrinsic resulting from the interaction of the crack with the microstructure. Some examples [5, 6] are crack branching, microcrack formation to alleviate stresses at the crack tip, bridging and phase transformations (*e.g.,* tetragonal to monoclinic zirconia transformation).

To study these toughening mechanisms, stable crack propagation tests may be performed in laboratory conditions. The Wedge Splitting Test (WST) allows such fracture tests to be conducted, even on quasi-brittle materials, by decreasing the elastic energy stored in the testing machine thanks to a wedge and cylinders to apply an opening (mode I) load [7, 8]. This test is commonly used for obtaining the fracture energy of these materials, which is a key property for understanding the thermal shock resistance of refractories [9, 10]. The advantage of this test includes a high fracture surface area to specimen volume ratio, which is needed for obtaining representative results if big aggregates are used for toughening purposes [8].

The WST may be combined with Digital Image Correlation (DIC) for studying crack propagation. DIC is based on tracking material points during the loading of the sample [11, 12, 13]. It is a full-field measurement technique instead of providing local data points obtained by, say, conventional extensometry. Recently, several studies have reported on how to treat such results and obtain further information from WSTs [14, 15, 16, 17, 18, 19].

If toughening mechanisms are activated during fracture, it is hard to define a "binary" crack, with either a fully broken or fully intact material. A Fracture Process Zone (FPZ) is usually defined, where some damage has already occurred but some tractions between the crack surfaces remain [20, 21]. In that case, a Cohesive Zone Model (CZM) can be used [22]. The CZMs define the traction-separation law, which accounts for the fracture process. Several studies use

CZMs in Finite Element Analyses (FEA) for simulating fracture in quasi-brittle materials [21, 23, 24, 25, 26].

The calibration of cohesive zone properties with DIC measurements was addressed in various studies, mostly for modeling composites and/or adhesives. Measured displacements were used as Boundary Conditions (BCs) and inner nodal displacements in the objective function to identify the cohesive properties of fiber-reinforced metallic laminate. Discussions about how to obtain elastic and cohesive properties by minimizing the gap between measured and calculated displacements were also reported for a fiber-reinforced cementitious material [27], and for plastic and PMMA with adhesive [28]. Reference [29] presents a sensitivity analysis in order to analyze the most relevant region for identifying a CZM with full-field measurements. The sensitivity for the identification of cohesive parameters for an adhesive bonded structure is discussed in Ref. [30]. The authors concluded that higher sensitivity for the cohesive strength may be reached at pre-peak, and for the fracture energy with post-peak data. Traction-separation laws could be accessed directly with the kinematics of a Double Cantilever Beam test for composite materials [31]. The importance of using load data to identify a mixed-mode CZM for a composite was highlighted in another study [32]. Conversely, mixed-mode CZMs were calibrated without the need for force data, only using the images of the experiment on a microelectronic device [33].

Some studies also showed the feasibility of combining DIC and CZM for other materials. In Ref. [34], a multiscale setup is introduced for analyzing a photodegradable copolymer. Elastic and cohesive properties for concrete materials were identified with the Boundary Element Method coupled with DIC measurements [35]. Failure in metals was modeled with a CZM, which was calibrated with DIC data [36]. Micrometer-scale mechanisms in PMMA could be related to a traction-separation law using images taken close to the crack tip [37]. No study on castable refractories was found with such approaches.

In the present work, the parameters of a macroscale CZM for mode I fracture are calibrated with a single WST by coupling DIC measurements, load data and

FEAs performed with the commercial code Abaqus [38] for a castable refractory. First, the identification framework is introduced, then followed by the methods and definition of the parameters to be calibrated. Last, the results are shown and compared with previously reported data on different methodologies.

2. Calibration procedure

2.1. Experiment

The WST analyzed herein was performed on a class C, anti-erosive commercial refractory, with ultra low cement content. The detailed chemical composition and heat treatment of the material are reported in Ref. [15]. Its processing and microstructure may lead to an increasing R-curve behavior with weakly bonded grains and initiated microcracks due to anisotropic phases and differential thermal expansions. The sample size was 100 mm in length, 100 mm in height and 72.5 mm in thickness. The geometry is shown in Fig. 1 along with the mesh introduced in Section 2.3. It is possible to see the sample and the loading devices (*i.e.,* wedge, cylinders and blocks). Two grooves (i.e., vertical notches, evidenced in the right image in Figure 1) are machined on the two opposite faces of the sample to reduce the local thickness and guide the crack propagation vertically [19].

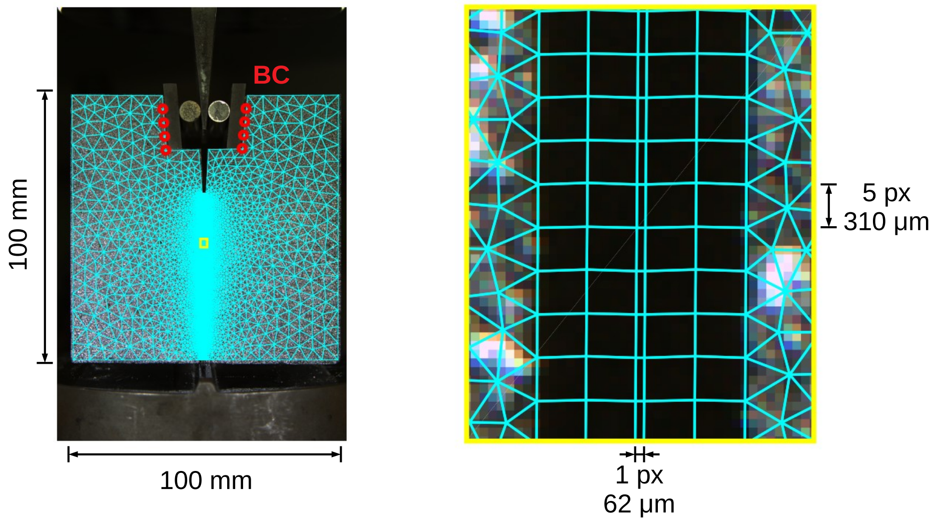

Figure 1: Sample geometry, with the FE mesh superimposed (left). The loading parts are visible at the top of the image. The red circles mark the nodes where the BCs are applied (see Section 2.3). The yellow box is zoomed (right), showing the mesh aligned with the groove edges. Triangular elements are used out of the groove, and Q4 quadrilaterals inside. The thin strip of elements in the middle of the groove shows the cohesive elements, which are collapsed to zero thickness for the present analyses.

The Young's modulus (E) and Poisson's ratio (ν) used for the investigated methods are equal to 17 GPa (measured by the bar resonance method [39]), and 0.2, respectively. The fracture energy calculated as the mean R-curve value (obtained by Integrated-DIC) is of the order of 68 J/m^2 [19]. The test was driven by setting the velocity of the machine actuator to 1.3 µm/s, and 313 pictures (reference + 312) were taken for both faces of the specimen at a rate of one picture each 8 s. The images were simultaneously acquired with two Canon T5 cameras with 28–135 mm lenses, with the illumination provided by LEDs. The 14-bit images captured at a definition of 2601×1733 pixels are up-sampled to 16-bit images with a dynamic range of approximately 60,000 gray levels. The imaged physical size of one pixel was 62 µm. A random speckle pattern was sprayed onto the specimen surfaces to increase the image contrast and improve the DIC resolution.

The horizontal force versus the splitting displacement, averaged from DIC measurements on opposite sides of the groove, is shown in Figure 2. The red circles mark the envelope of the curve that will be used by the identification routine with always increasing opening displacements. Let us note that since the test was interrupted before final failure of the sample, only a lower bound to the work of fracture, and to the fracture energy can be obtained [19].

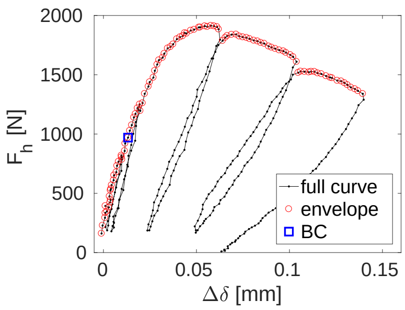

Figure 2: Horizontal force (*i.e.,* 5.715 times the vertical force) versus splitting displacement $\Delta\delta$ averaged on both sides of the sample. The images corresponding to the displacement envelope used in the identification are marked as red circles. Image no. 39 used for the BC_c parameter as explained in Section 2.6 is shown as a blue square.

Given the fact that the first picture was not acquired at zero load and a nonlinear model will be used, the displacement field accounting for this load offset is an additional unknown when calibrating constitutive parameters [40]. This is in particular true for cohesive zone models [32]. Image no. 39, highlighted with a blue square, is chosen for the BC corrections (see Section 2.6) since it is considered to be in the linear elastic regime (*i.e.,* 50% of the maximum force) and with higher displacement levels than the first images, thus being less affected by acquisition noise. Further details on the same experiment can be found in Refs. [15, 19].

2.2. Digital Image Correlation

In global DIC, the displacement field $\mathbf{u}_{DIC}$ is measured by considering that every pixel $\mathbf{x}$ within the Region Of Interest (ROI) in the reference image f is present in the deformed (*i.e.,* in a loaded state) image g but has moved by

$\mathbf{u}_{DIC}$ so that the displacement field globally minimizes the gap to gray level conservation

$$\phi^2 = \sum_{\text{ROI}} \left[f(\mathbf{x}) - g(\mathbf{x} + \mathbf{u}_{DIC}(\mathbf{x})) \right]^2 , \tag{1}$$

which is the L2-norm of the gray level residuals $\rho(\mathbf{x})$. In order to ensure a good conditioning of this minimization and its robustness to noise, one more consideration is added to regularize the kinematics of a group of pixels, namely, it consists in expressing the sought displacement field as

$$\mathbf{u}_{DIC}(\mathbf{x}) = \sum_{i=1}^{N} \upsilon_i \mathbf{\Psi}_i(\mathbf{x}), \tag{2}$$

in which υ_i are the degrees of freedom, and $\mathbf{\Psi}$ selected vector fields. In such a framework, the measured displacements are obtained as

$$\{\boldsymbol{\upsilon}_{\text{DIC}}\} = \arg\min_{\{\boldsymbol{\upsilon}\}} \phi^2(\{\boldsymbol{\upsilon}\}), \tag{3}$$

where $\{\upsilon_{\text{DIC}}\}$ is the column vector gathering all amplitudes υ_i. A robust solution that works in most cases is choosing $\mathbf{\Psi}_i$ as finite element shape functions [41]. In this paper, the DIC procedure is performed with 3-noded linear elements in a finite element discretization [42] and will be referred to as T3DIC.

In the method presented herein, the first step is to run T3DIC since it will provide the necessary Boundary Conditions (BC) as explained in Section 2.3, and also displacement fields that can be compared with FE results. The mesh used for T3DIC and one displacement field (for image no. 263, *i.e.,* the last of the envelope, see Figure 2) is shown in Figure 3. The average element length is 37 pixels. This relatively large element size is chosen in order to reduce uncertainties due to acquisition noise. Care was taken to properly get the contour of the sample for avoiding identification artifacts and fully exploiting the image contrast as shown in the zoomed yellow rectangle. The central grooves are designed to guide the crack propagation along the center plane. However, castable refractories are prone to crack branching. For this experiment, it was shown that no major side branches were formed and only a single macrocrack had propagated in the groove [19].

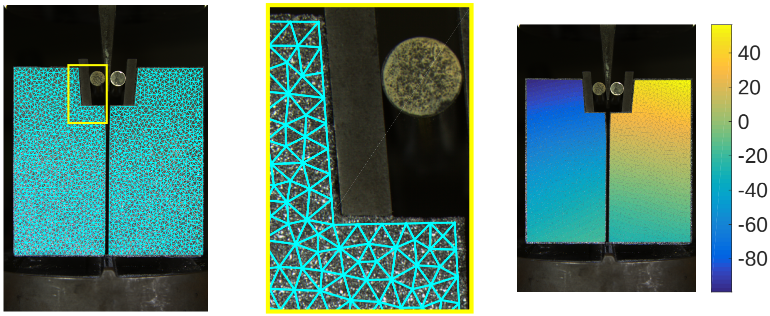

Figure 3: Sample geometry with superimposed T3DIC mesh (left). A zoom of the yellow rectangle is presented in the middle to show the contour of the mesh close to the loading plate. Horizontal displacement field expressed in μm for the last analyze image.

2.3. Numerical model

The FEA is performed with the commercial code Abaqus [38]. The geometry is taken from the image for ensuring that the measurement by T3DIC is performed exactly on the same region. The mesh is generated with GMSH [43] and shown in Figure 1, in which the nodes where the Dirichlet BCs are prescribed are shown with red circles. The corner node is not considered due to higher measurement uncertainty [44]. Since the exact same contours are used for the DIC and FE meshes in this region, a linear interpolation is performed to get the BCs. The groove (see Figure 1) has a reduced out-of-plane thickness. The yellow box corresponds to a zoom in the groove to show the mesh details. In the middle of the groove, a single strip of zero thickness cohesive elements (200 in the height) is added. Each face of the sample will be analyzed independently as a 2D model under plane strain hypothesis.

2.4. Identification strategy

The chosen identification scheme is based upon the Finite Element Model Updating (FEMU [45]) method. It is chosen to update the material parameters by reducing the difference between the calculated reaction force F_c and the experimentally measured force F_m. It is worth noting that the unload/reload cycles are excluded from the identification since more complex CZMs would be necessary to accurately describe them [46]. Consequently, only the envelope of the curve is kept (*i.e.,* 100 out of the 312 images for which the crack is propagating, see Figure 2). It is chosen to have a continuous displacement of the actuator.

The identification methodology (*i.e.,* Newton-Raphson scheme) consists in a nonlinear least squares minimization of χ_F^2

$$\chi_F^2(\{\mathbf{p}\}) = \frac{1}{n_t \sigma_F^2} \sum_t \left(F_m(t) - F_c(t, \{\mathbf{p}\})\right)^2 , \tag{4}$$

in which σ_F is the standard load uncertainty (on F_m), n_t the number of time steps, and F_c is the computed resultant of the reaction forces, which depends on unknown material parameters gathered in the column vector $\{\mathbf{p}\}$. If the only difference between the measured load levels $F_m(t)$ and $F_c(t, \{\mathbf{p}\})$ is acquisition noise, then χ_F will approach unity. Conversely, if there is a model error, then $\chi_F > 1$. By considering a given starting set of parameters $\{\mathbf{p}_n\}$ at iteration n, the minimization is performed by evaluating the correction $\{\delta\mathbf{p}\}$ on the linearized F_c

$$F_c(t, \{\mathbf{p}_n\} + \{\delta\mathbf{p}\}) \approx F_c(t, \{\mathbf{p}_n\}) + \frac{\partial F_c}{\partial\{\mathbf{p}\}}(t, \{\mathbf{p}_n\})\{\delta\mathbf{p}\}, \tag{5}$$

about the current estimate $\{\mathbf{p}_n\}$ of the sought parameters. The minimized quantity then becomes

$$\frac{1}{n_t \sigma_F^2} \sum_t \left(F_m(t) - F_c(t, \{\mathbf{p}_n\}) - \frac{\partial F_c}{\partial\{\mathbf{p}\}}(t, \{\mathbf{p}_n\})\{\delta\mathbf{p}\} \right)^2 . \tag{6}$$

In Equation (6), the quantity to be minimized is quadratic in terms of $\{\delta\mathbf{p}\}$. Its minimization with respect to $\{\delta\mathbf{p}\}$ then leads to a linear system

$$[\mathbf{H}] \cdot \{\delta\mathbf{p}\} = \{\mathbf{h}\} \tag{7}$$

where $[\mathbf{H}]$ is the Hessian

$$[\mathbf{H}] = \sum_t \left(\frac{\partial F_c}{\partial\{\mathbf{p}\}}(t, \{\mathbf{p}_n\}) \right)^\top \frac{\partial F_c}{\partial\{\mathbf{p}\}}(t, \{\mathbf{p}_n\}) \tag{8}$$

and $\{\mathbf{h}\}$ the right hand member

$$\{\mathbf{h}\} = \sum_t \left(F_m(t) - F_c(t, \{\mathbf{p}_n\})\right) \frac{\partial F_c}{\partial \{\mathbf{p}\}}(t, \{\mathbf{p}_n\}). \tag{9}$$

Convergence is deemed successful when the root mean square (RMS) of the relative variation of the parameters is less than 10^{-2} between two subsequent iterations. The sensitivity fields $\frac{\partial F_c}{\partial \{\mathbf{p}\}}$ are computed via finite differences in which the perturbation with respect to each parameter is set to 1%. The framework of the identification methodology may be further discussed by the sensitivity analysis presented in Section 3.1 using the Hessian $[\mathbf{H}]$.

2.5. Cohesive law

In this work, the selected cohesive law is the so-called PPR (Park, Paulino and Roesler) model [47, 48]. It was considered since the built-in cohesive models may give unrealistic responses for mixed mode propagations [49]. It is implemented in Abaqus with a User ELement (UEL) subroutine[1] [48]. Apart from the groove where the crack propagates and the cohesive model is implemented, the remaining part of the specimen has a linear elastic behavior. The information about mode II propagation or compressive damage was not considered, but care was taken in the implementation so that it did not interfere with the reported results. Figure 4 shows the two parameters to be calibrated for the cohesive zone model used herein, namely, the cohesive strength σ_{max}, and the fracture energy J_c.

[1] https://paulino.ce.gatech.edu/PPR_tutorial.html

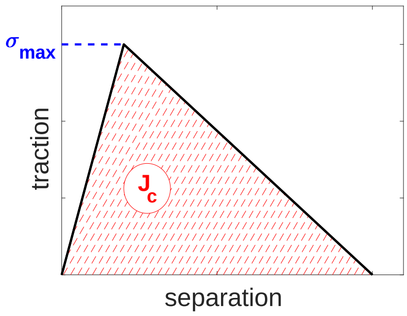

Figure 4: Schematic traction separation law highlighting the main parameters ($\sigma_{\max}$ and J_c) to be calibrated.

For the PPR model, the constitutive behavior for mode I includes the cohesive strength σ_{max}, and the fracture energy J_c. Two additional parameters are considered, namely, the initial slope λ_n and the shape parameter α. These last two parameters are chosen to be constant in the identification scheme. λ_n is kept equal to 0.005 for both cases [48], and considered as a small value within the stability limits [47]. The sensitivity to λ_n was tested and did not significantly affect the results. The parameter α however does change the softening response of the cohesive law. For the first case, its value is taken as 2 in order to approach a bilinear law [47] as shown in Figure 4. The second analyzed case considers $\alpha = 7$ to change the shape of the curve (Figure 11) to check if it better describes the considered test. Two built-in CZMs, namely, a bi-linear traction-separation law and the so-called Concrete Damaged Plasticity model, were also tested with parameters to replicate the studied case with $\alpha = 2$ and yielded very similar results [46]. For the sake of brevity, they are not discussed herein.

2.6. Boundary condition correction

One additional parameter is related to the non-zero load associated with the acquisition of the first image (Figure 2). It calls for a BC correction [32, 40] and will be designated as BC_c. In the experiment, the reference image was taken with a pre-load in order to remove any slack in the loading configuration.

Thus, the reference image of the unloaded state is unknown, and all measured displacements are performed with respect to the pre-load configuration.

The parameter BC_c introduced herein thus has to correct the kinematics from the unloaded state to the pre-loaded state. It is chosen to define BC_c as a multiplicative scalar of the displacement field related to a specific time step in the elastic regime of the experiment, and add it to the displacement fields for all time steps. The logical choice would be to consider the displacements of the very first images but they are small and consequently more affected by acquisition noise. Image 39 (*i.e.,* the 24th of the envelope, see Figure 2), which corresponds to approximately half of the maximum load, is chosen as a compromise of remaining in the linear part of the load but not too close to the noisier beginning. The corrected displacement fields $\mathbf{u}_{BC_c}$ read

$$\mathbf{u}_{BC_c} = (BC_c - 1) \cdot \mathbf{u}_{39}, \tag{10}$$

When BC_c is equal to 1, no correction is performed. It is expected that $BC_c > 1$ for the correction of the reference state with an opening displacement field, *i.e.,* a fraction of the displacement field measured in image 39. In the case of $BC_c < 1$, a contraction displacement field would be considered in the correction.

2.6.1. Initial parameters

The properties used for initializing the identification scheme are listed in Table 1. The cohesive strength σ_{max} was selected as the maximum T-stress measured in Ref. [19] with the method that provided more trustworthy results for the T-stress (*i.e.,* FEMU). The initial fracture energy J_c corresponds to its estimate based upon Integrated-DIC results [19]. The last parameter, BC_c, has its initial value set to one (*i.e.,* no BC correction would be needed).

Table 1: Initial parameters for the identification scheme.

σ_{max} [MPa]	J_c [J/m^2]	BC_c [-]
2	68	1

3. Results

3.1. Sensitivity analysis

Before performing the calibration of material parameters, a sensitivity analysis is performed [50]. Only the case $\alpha = 2$ is reported since the sensitivities are very close to those when $\alpha = 7$. The load sensitivities are defined as

$$S_F(t, \{\mathbf{p}_0\}) = \frac{\partial F_c}{\partial \{\mathbf{p}\}}(t, \{\mathbf{p}_0\}), \tag{11}$$

and approximated using a forward difference approach with a perturbation factor $\epsilon = 10^{-2}$ of each parameter. Figure 5 shows the computed load sensitivity S_F, indicating the influence of each parameter as a function of time. The influence of the parameter BC_c is very important at the beginning of the test. The peak influence of the cohesive strength σ_{max} occurs in the middle of the sequence of images, which is related to the part of the test where the measured force is high. The fracture energy J_c has higher sensitivity at the end of the test, which is to be expected since the crack has propagated a significant distance [15, 19]. For all parameters, the load sensitivities are significant (in comparison with the load uncertainty) for a one percent variation of each parameter. This result indicates that the parameters are expected to be identifiable with the considered test and identification procedure.

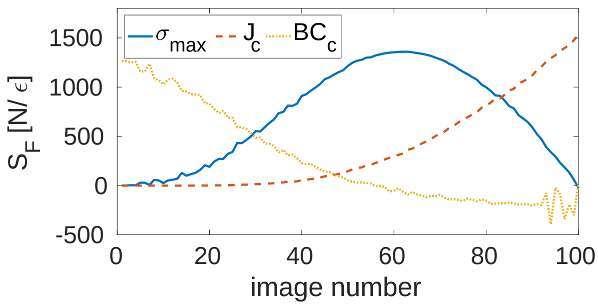

Figure 5: Force sensitivity to the parameters of the $\alpha = 2$ case. The blue solid line is the sensitivity to the cohesive strength σ_{max}, with a maximum sensitivity close to the middle of the test, *i.e.,* near the maximum splitting load. The red dashed line is related to the fracture energy J_c with a maximum sensitivity to the end of the test, after many elements are already damaged. The yellow dotted line corresponds to the BC correction BC_c, with maximum sensitivity at the beginning of the test where the displacements are very small.

Figure 6(a) shows the decimal logarithm of the values of the 3×3 Hessian ([**H**], see Equation (8)). The diagonal terms indicate the sensitivity to each property considered independently, and the off-diagonal members the cross influences between parameters. In the case of fully independent parameters, only the diagonal terms would be different from zero. As expected from the previous analysis, all parameters have very high sensitivities, and the conditioning of the system is very good (*i.e.,* less than 10). From this sensitivity analysis, it is confirmed that all parameters can be calibrated with the selected test and identification procedure.

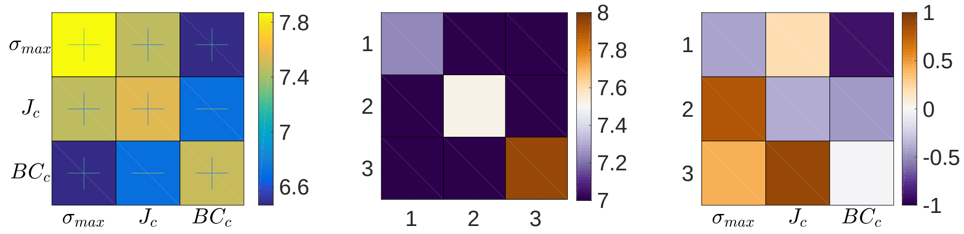

(a) (b) (c)

Figure 6: (a) Hessian of the identification procedure for the $\alpha = 2$ case shown as decimal logarithm. The diagonal terms show the sensitivity of each independent parameter. The off-diagonal terms show the cross influence between the parameters. (b) Decimal logarithm of the diagonalized Hessian. (c) Eigen column vectors associated with the diagonalization of the Hessian.

The decimal logarithm of the diagonalized Hessian is shown in Figure 6(b). Given the fact that the minimum eigen value of the Hessian is very high, there was no need for regularizing the Newton-Raphson scheme to ensure the definiteness of [**H**]. The first eigen value is dominant in BC_c and is almost independent of the other parameters. The second and the third eigen values are dominant in $\sigma_{\max}$ and J_c, in the same order of magnitude, showing that they are more correlated. Such conclusion is drawn from the eigen vectors reported in Figure 6(c).

3.2. Calibration results

Figure 7 shows the experimental and computed resultant forces for the two analyzed cases, *i.e.,* with the PPR model and for $\alpha = 2$ and $\alpha = 7$. The identified parameters give a very good fit of the experimental curve, which is a first validation of the model. The differences between both cases are very small.

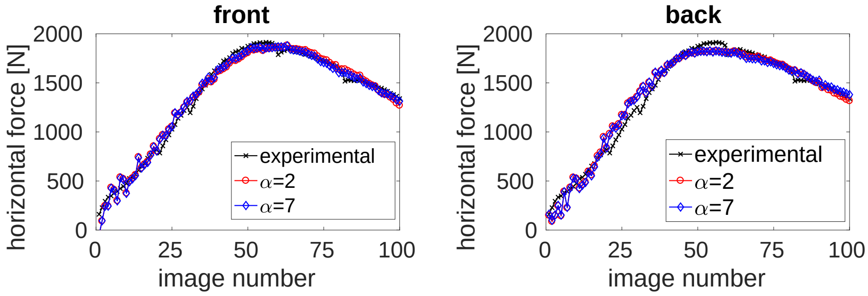

(a) (b)

Figure 7: Experimental and computed reaction forces on the converged state for the two analyzed cases, for the front (a) and back (b) faces of the experiment.

For easier comparison, the difference between the calculated and experimental forces, which have been normalized by the standard load uncertainty[2], are shown in Figure 8. Although some oscillations are seen, the mean value is plotted in dashed lines, showing that on average the error was of the order of twice the acquisition noise. This level is sufficiently small [32] to validate both cases. For the front face, $\alpha = 7$ provided slightly better results (RMS error of 1.5 as opposed to 1.8 when $\alpha = 2$), and for the back face $\alpha = 2$ was a bit better (RMS error of 2.0 against 2.1). Overall, considering only the force residuals, it is concluded that $\alpha = 7$ is (a bit) more suitable for the test studied herein. However, a bilinear model should not be excluded since its performance is also very good.

[2]The load uncertainty is equal to 0.1 % of the 5 kN load cell capacity, *i.e.*, 5 N for the vertical force, namely, of the order of 30 N for the horizontal force.

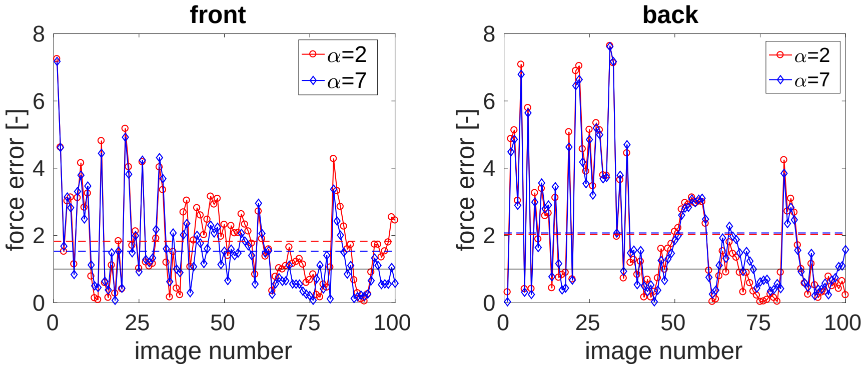

(a) (b)

Figure 8: Absolute reaction force residuals for the two cases normalized by the standard load uncertainty (solid lines), for both faces of the sample. The temporal average is shown as dashed lines.

The displacement fields were not used in the identification routine except at very few points as BCs in the FEA. The measured and computed displacement fields can thus be compared at any other location provided the computed displacement field corresponding to the reference image cancels out. For the calibrated parameters, the relative displacements (with respect to the pre-load configuration) are computed and then compared to the T3DIC kinematics at each time step of the test. These corrected FE results (whose mesh is shown in Figure 1) are interpolated onto the T3DIC mesh (Figure 3) and the RMS difference normalized by the standard displacement uncertainty is shown in Figure 9. The differences between front and back faces are mostly related to experimental inaccuracies, which are higher for the back face. The increasing trend shows that the numerical assumptions (*i.e.*, the constitutive law) are less true as the test goes on. However, the average error is of the order of 2.5 times the displacement uncertainty for the front face, and about 1.5 times for the back face. This level is sufficiently low [32] to give confidence in the model considered herein. The differences of the mean value between both cases is negligible (*i.e.*, of the order of 10^{-3}).

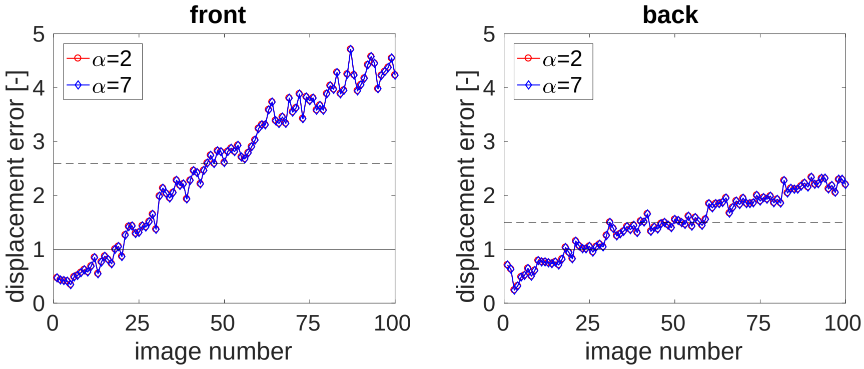

(a) (b)

Figure 9: RMS residual between computed and experimental displacements normalized by the T3DIC displacement uncertainty (solid lines). The temporal average is shown as dashed lines.

With the proposed framework, the gray level residuals from the FE results can also be checked. This is possible because measured displacements were prescribed as BCs in the numerical model, and the computed displacement fields were corrected to account for the fact that the reference configuration corresponds to the pre-loaded sample. The gray level residuals read

$$\rho_{FEA}(\mathbf{x}, t) = f(\mathbf{x}) - g_t(\mathbf{x} + \mathbf{u}_{FEA}(\mathbf{x}, t)) \tag{12}$$

where $\mathbf{u}_{FEA}$ is the computed displacement field, after taking out the pre-load kinematics related to BC_c, interpolated onto the T3DIC mesh. The same framework used for performing T3DIC may then be used to evaluate the gray level residuals. The RMS level of $\rho_{FEA}(\mathbf{x}, t)$ performed over all pixel location $\mathbf{x}$ of the ROI normalized by the corresponding T3DIC residual $\rho_{DIC}(\mathbf{x}, t)$

$$\frac{\mathrm{rms}_{\mathrm{ROI}}[\rho_{FEA}(\mathbf{x}, t)]}{\mathrm{rms}_{\mathrm{ROI}}[\rho_{DIC}(\mathbf{x}, t)]} \tag{13}$$

for each image is shown in Figure 10, where

$$\rho_{DIC}(\mathbf{x}, t) = f(\mathbf{x}) - g_t(\mathbf{x} + \mathbf{u}_{DIC}(\mathbf{x}, t)) \tag{14}$$

The former is only 50 to 60 % higher than the latter in which no hypothesis was made on the constitutive behavior. This observation further validates the overall trends of both cases. As reported for the displacement residual, the mean value of the normalized gray level residual between both cases is of the order of 10^{-3}.

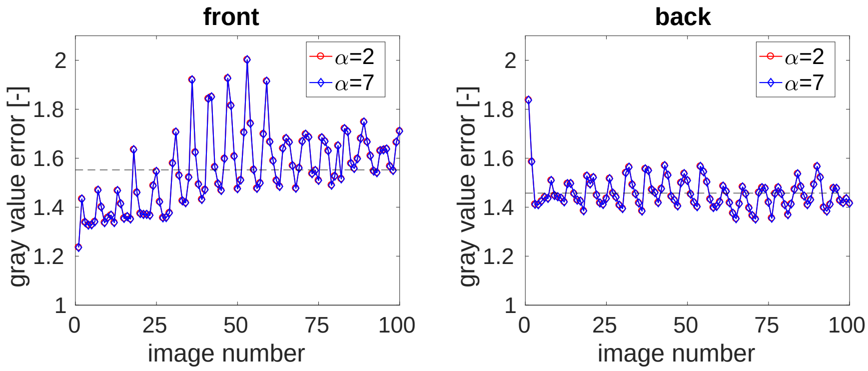

(a) (b)

Figure 10: Gray level residuals using FEA kinematics (ρ_{FEA}) normalized by the gray level residuals obtained from T3DIC (ρ). The temporal average is shown as dashed lines.

Figure 11 shows the traction vs. separation responses for each calibrated model. The curves represent the response of the most damaged element, *i.e.*, the closest element to the pre-crack, showing that no element was fully damaged (*i.e.*, the maximum level is equal to ≈ 0.85 and 0.75 when $\alpha = 2$ and $\alpha = 7$, respectively). It is worth remembering that complete propagation was not achieved since the experiment was performed until 70 % of the peak load (Figure 2).

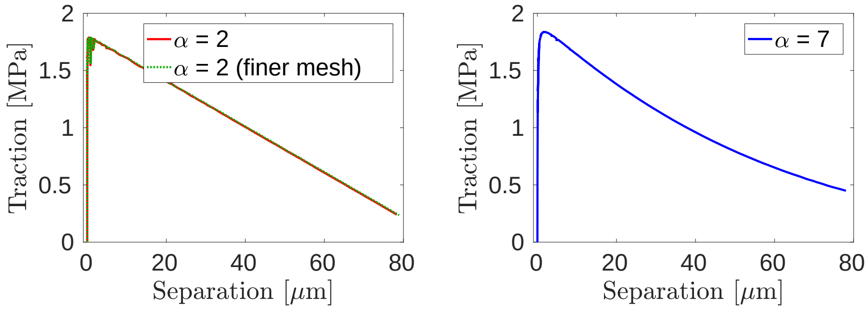

(a) (b)

Figure 11: Traction vs. separation responses of the most damaged element for the two cases calibrated with the front face data. The response for the mesh sensitivity analysis (discussed at the end of this section) is shown when $\alpha = 2$, where the main difference at the end of the curve is of the order of 0.01 MPa.

Table 2 gathers the calibrated parameters for each studied case when initialized with the set given in Table 1. The traction vs. separation curves (Figure 11) are similar for both cases, close to a bilinear response when $\alpha = 2$, and with a nonlinear softening when $\alpha = 7$. They all converged after at most five iterations of the FEMU-F procedure. It is possible to see that σ_{max} varies in the range 1.70 ± 0.15 MPa for the two cases; J_c has a difference of almost 20 % from $\alpha = 2$ to $\alpha = 7$, with a smaller difference if the same case is considered and both faces are compared. The BC_c difference highlights that the wedge was not fully aligned. It is possible to conclude that the wedge was applying more force on the back face of the specimen at the beginning of the test. It is worth noting that the cohesive strengths σ_{max} are of the same order of magnitude as the maximum T-stresses reported in Ref. [19].

Table 2: Converged parameters on the identification scheme for the two studied cases.

face	α	σ_{max} [MPa]	J_c [J/m^2]	BC_c [-]
front	2	1.79	82	1.314
	7	1.84	100	1.320
back	2	1.58	89	0.897
	7	1.59	115	0.906

Although the mesh is finer than classical guidelines for cohesive elements [51, 52, 53, 54] (*i.e.,* 200 elements in the total length of the propagation path, which will be shown to be less than the process zone length in Section 3.3.2), a mesh sensitivity analysis was performed with a finer mesh having more than 3 times the number of cohesive elements (*i.e.,* 620). When the subsequent FEMU-F procedure was initialized with the parameters calibrated with the coarser mesh, only one iteration was needed to reach convergence (*i.e.,* the parameter differences were less than 0.5 %). This observation proves that the two solutions are very close, which is confirmed in Figure 11(a) in terms of the traction separation law. From this analysis it is concluded that mesh convergence was achieved with the 200-cohesive element mesh. All the results of the next section were also checked for the two mesh densities and no tangible differences were observed. For the sake of brevity, they will not be presented.

3.3. Discussion

3.3.1. Fracture energy

In order to better understand the simulated fracture behavior, one last analysis is proposed. The displacements of the nodes of each cohesive element on the identification analysis are applied as BCs in a zip-like model, namely, only using the cohesive elements. With this approach, it is ensured that the same experimental kinematics is applied. It follows that the reaction forces at each node can be extracted. From the reaction forces, the tractions in each element and each time step are available. Using the traction / separation of each element, the dissipated energy can be computed. The vertical (mode II) displacements and corresponding reaction forces are insignificant and are thus not accounted for hereafter.

The mode I tractions T_I are shown in Figure 12 for the front face. The image number on the x-axis is related to the time step for the envelope images (Figure 2). The y-axis is the vertical position of each node along the groove, *i.e.*, $y = 0$ is the node closest to the pre-crack and $y = 60$ mm the one at the bottom of the sample. A compressive zone develops after image no. 40, which hinders the propagation but does not stop the crack. Even though the color bar is fixed from -2 to 2 MPa for easier visualization, the minimum level is approximately -9 MPa. Similar figures are generated for the back face, which are reported in Appendix A (Figure 17).

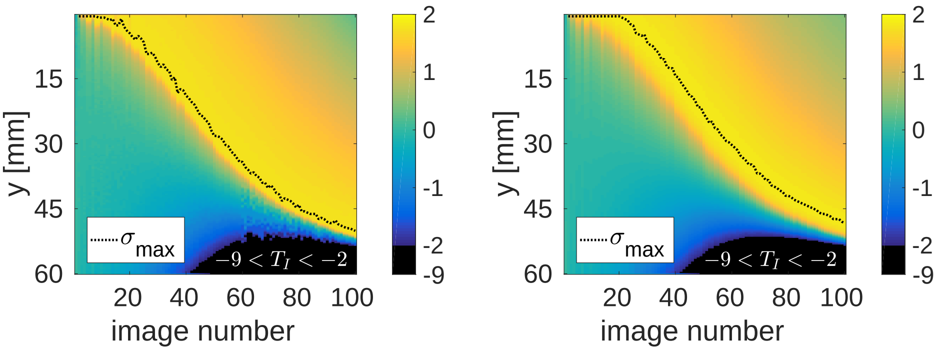

(a) (b)

Figure 12: Normal traction (expressed in MPa) history for the front face when $\alpha = 2$ (a) and $\alpha = 7$ (b). The black dotted line shows the location for which the cohesive strength $\sigma_{\max}$ was reached.

It is worth noting that σ_{max} was not reached for the last elements since the test was not performed until final failure. For the same reason, non-vanishing tractions are still observed in the first elements. The region where the energy is being dissipated is large (*i.e.,* many damaged cohesive elements), with remaining cohesion even close to the pre-crack. Only the elements closest to the initial notch experience small traction levels, which indicates that their damage level is high. To determine the fractured surface, it is possible to consider an equivalent damage variable for any CZM. For each node, the damage parameter is defined as

$$D = 1 - \frac{\sigma_I}{\sigma_{max}} \quad \text{when} \quad 0 < [\![u_I]\!] < \delta_c \tag{15}$$

where σ_I is the mode I traction (whose spacetime history is shown in Figures 12 and 17), $[\![u_I]\!]$ the mode I opening displacement, δ_c the maximum separation, and σ_{max} the cohesive strength. The damage variable history calculated with Equation (15) for the front face and both analyzed α is shown in Figure 13. Although the material is quasi-brittle, Figure 13 shows that the damage grows slowly. About two thirds of the sample have been damaged at the end of the reported test. Some cohesion remains along the whole propagation path (as already discussed above). However, there is a ligament in which no damage at all has occurred. The same trends are observed for the back face, as reported in Appendix A (Figure 18).

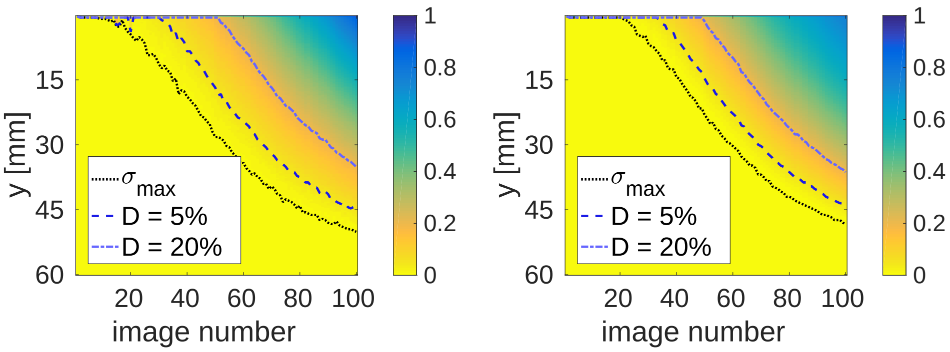

(a) (b)

Figure 13: Damage history for the front face when $\alpha = 2$ (a) and $\alpha = 7$ (b). The black dotted line shows the location for which the damage variables starts to grow (*i.e.,* when the cohesive strength $\sigma_{\max}$ was reached).

The elementary fracture energy corresponds to the area under the cohesive response. It is obtained by integrating the opening displacement vs. traction responses of each cohesive element. At a given step, the dissipated energy is calculated by removing the elastic energy from the total work of each element. Figure 14 shows the dissipated energy for each cohesive element of the front face of the analyzed cases. The maximum possible dissipated energy is equal to J_c (*i.e.*, 82 J/m^2 for $\alpha = 2$ and 100 J/m^2 for $\alpha = 7$). Not a single element reached this value, since the maximum level is found equal to 71 J/m^2 and 64 J/m^2, respectively. The same tendencies are observed for the back face (Figure 19).

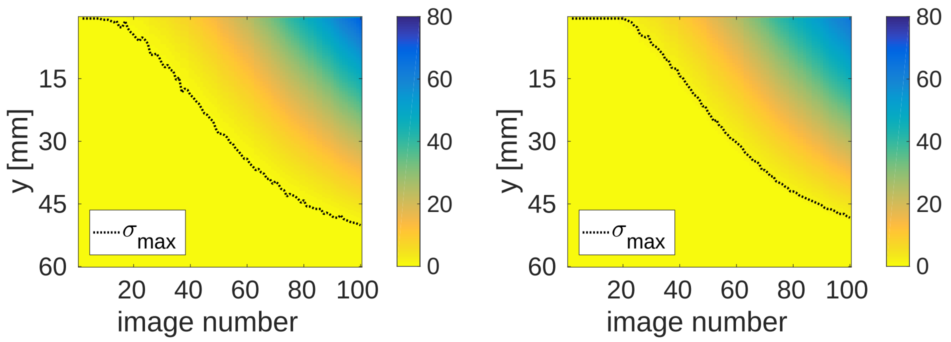

(a) (b)

Figure 14: Elementary dissipated energy (expressed in J/m^2) for the front face, with $\alpha = 2$ (a) and $\alpha = 7$ (b). The black dotted line shows the location for which the cohesive strength $\sigma_{\max}$ was reached.

Let us consider the cracked surface as the damaged area, *i.e.*, the region from the first to the last cohesive elements that reached σ_{max}. The total dissipated energy is calculated by multiplying the elementary dissipated energy (see Figure 14) by the element area, and summing the contributions of every element at each time step. The total dissipated energy is shown as a function of the "crack" length (as defined above) in Figure 15. An exponential interpolation describes the observed trends, which means that as the damaged zone grows, a bigger energy increment is needed to further propagation. Overall, the crack propagated a little farther and dissipated more energy in the back face, as seen in Figure 15. This result was expected from the conclusions analyzing the BC_c parameter (*i.e.*, tilted wedge applying more force on the back side). When $\alpha = 2$ case, the crack propagated a little farther and more energy was dissipated on both faces of the sample.

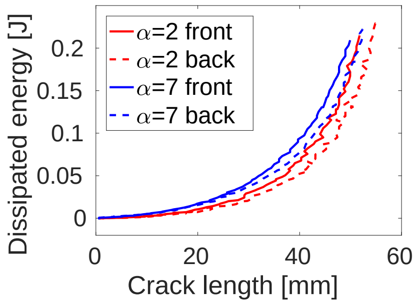

Figure 15: Dissipated energy in the analyzed test for the studied parameters. Solid lines represents the front face results, and the back face ones are in dashed lines.

To evaluate the global fracture energy, $\mathcal{G}_c$, let us consider E_{diss} as the total dissipated energy in the specimen during crack propagation

$$\mathcal{G}_c = \frac{\partial E_{\mathrm{diss}}}{\partial A} \tag{16}$$

where the derivative describes how much energy is dissipated for each unitary increment of cracked area. Before taking the derivative, an exponential fit is considered to suppress the amplification of measurement uncertainties. The corresponding results are shown in Figure 16. Both cases lead to consistent results with small differences on the curvature, maximum crack length, and $\mathcal{G}_c$ level for a given face. Longer cracks are seen at the back of the specimen when the results of the two faces are compared. It is worth noting that the curve reported in Figure 16 is not physically allowed to start from $\mathcal{G}_c = 0$, since there is a minimum energy to break chemical bounds. However, this works aims to analyze propagating macrocracks, and at this scale, the resolution was not sufficient to check for the very beginning of this curve.

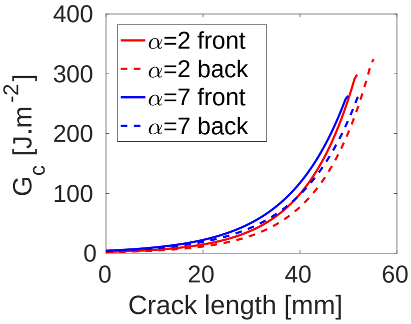

Figure 16: Global fracture energy $\mathcal{G}_c$ predicted by the studied CZMs, which are calculated from the exponential fit of the total dissipated energy. The results from the front face are in solid lines and for the back face in dashed lines.

To check these results and compare them with earlier estimates [15, 19], the mean level $\overline{\mathcal{G}}_c$ is calculated

$$\overline{\mathcal{G}}_c = \frac{1}{\Delta a_{\max}} \int_0^{\Delta a_{\max}} \mathcal{G}_c(a) \, \mathrm{d}a \tag{17}$$

where $\Delta a_{\max}$ denotes the maximum length of the damaged area. The values of $\overline{\mathcal{G}}_c$ are reported in Table 3. A good agreement is observed with the values reported in Refs. [15, 19] when integrated DIC is considered. The values are father apart with FEMU-U [19] (*i.e.*, with a cost function using displacement measurements) is used instead. With the present case, it is not possible to clearly distinguish which α is better since both yielded very low residuals and consistent results.

Table 3 compares the fracture energy predicted the proposed approach with two other independent methods applied to the same experiment. Although the methodologies reported in Refs. [15, 19] do not use CZMs, the energetic approach allows such comparisons. The fracture energies obtained with the PPR model are very close for the front and back faces, while those reported before had more significant differences. It is believed that it may related to the BC_c parameter, which corrects for the unknown fully unloaded state and was not accounted for with the other methods [15, 19]. For the finer mesh and $\alpha = 2$, the average fracture energy is found equal to 62.2 J/m^2, which is very close to the level found with the coarser mesh (Table 3). This observation further confirms the quasi mesh independence of the results reported herein.

Table 3: Average fracture energy $\overline{\mathcal{G}}_c$ expressed in J/m^2 for the two CZMs applied to the back and front faces separately. These predictions are compared with earlier results obtained by two independent approaches (*i.e.*, integrated DIC [15] and FEMU-U [19])

model	front face	back face
PPR ($\alpha = 2$)	61.3	62.4
PPR ($\alpha = 7$)	63.5	62.2
IDIC$^\sharp$	84	52
FEMU-U$^\sharp$	162	97

$^\sharp$ according to Refs. [15, 19]

In order to improve the proposed methodology, the identification could be coupled for both faces, or even based on 3D simulations. Implementation of cohesive elements with similar approaches for cases where the crack bifurcates on the surfaces is also an interesting outlook. Last, 4D analyses via in-situ tests in x-ray tomographs may elucidate further the crack paths and fracture mechanisms taking place in such materials.

3.3.2. FPZ size

Since nonzero tractions are still predicted even close to the precrack at the end of the test, a final discussion about the FPZ size and its relationship with the material is discussed. With the identified parameters, the so-called Hillerborg size ℓ_H [20] is evaluated

$$\ell_H = \frac{EJ_c}{\sigma_{\max}^2} \tag{18}$$

and reported in Table 4. The length of the process zone is generally a fraction of ℓ_H [55]. In the present case, the FPZ length is of the order of ca. 50 mm (see Figures 12 to 16, for instance), which is one order of magnitude smaller than ℓ_H.

Table 4: ℓ_H for the studied cases in millimeters.

model	front face	back face
PPR ($\alpha = 2$)	434	604
PPR ($\alpha = 7$)	500	773

The estimate of the FPZ length leads to the conclusion that the FPZ was not yet fully developed, which is proven by the remaining stresses close to the pre-crack. This also explains the increasing energy release rate curve [56]. To further analyze the FPZ, the test should be continued until the end of the propagation, or in the case of materials with high ℓ_H as the one studied herein, a longer sample would be preferable.

The obtained fracture parameters and the FPZ length are consistent with the material microstructure and its processing. The analyzed composition is suitable for fluidized catalytic cracking units that operate in temperature ranges of 550 to 800 °C. Such materials are not sintered in situ as other refractories, and thus, their resistance strongly depends on the hydraulic bindings and packing of the raw material [57]. As this specimen was fired at low temperature (*i.e.,* 500 °C [19]), it is expected to have aggregates weakly bonded to the matrix and microcracks related to the anisotropy of the phases [57]. The initiation of a crack is easy in such materials, which explains the low level of the cohesive strength σ_{max}. Since the specimen cannot store much elastic energy prior to crack initiation (*i.e.,* the elastic energy is proportional to σ_{max}^2), the latter is easy and occurs very early on, and subsequent crack branches and bridging are possible, thereby dissipating more energy through friction and leading to a considerably higher J_c. In the present case, it is believed that crack bridging is the most likely mechanism since no branches were detected macroscopically on the investigated faces [19]. All these effects result in a large FPZ that in the case investigated herein spans over all the propagation path.

4. Conclusions

A FEMU-F methodology was applied to calibrate cohesive properties, *i.e.*, the cohesive strength (σ_{max}) and the fracture energy (J_c), of the so-called PPR model. Only the reaction forces were considered in the cost function to be minimized. By using the geometry seen on digital images to build the FE mesh, T3DIC results were directly used as boundary conditions to drive the simulations. The same region being used in T3DIC and FE analyses also allowed the experimental displacements to be compared with the simulated kinematics. The Hessian matrix was directly analyzed to infer the conditioning and sensitivity of the identification scheme to the sought parameters. It was also proposed to add a third parameter related to the correction of the applied boundary conditions.

The two studied softening regimes of the cohesive law resulted in similar material properties. Both σ_{max} and J_c were identified in the range of castable refractories, with values close to identifications obtained via integrated DIC [15, 19]. The cohesive strengths were very close on both analyzed faces of the sample, while some deviation of the order of 20 % was reported for the fracture energy. However, the dissipated energy was similar for both sides of the sample. The parameters identified for the cohesive law allowed the Hillerborg length to be calculated. When coupled with the traction space-time history of the cohesive elements, it gives insight into FPZ length. The boundary condition corrections were significantly different for both analyzed faces, thereby emphasizing that the wedge was slightly tilted at pre-load. It is worth noting that the thickness of the specimen combined with the presence of aggregates on the composition makes it difficult to perfectly align the wedge. However, the proposed approach showed robustness to tackle this misalignment.

The present study shows the feasibility of modeling crack propagation of castable refractories tested in the WST with cohesive elements. Cohesive parameters were calibrated with good correlations to previously reported fracture parameters for the same experiment. The residuals in force, displacement and gray level were very close to the noise level, which validates the methodology *and* the investigated model. Given the fact that damage did not reach its maximum value explains why an ever increasing R-curve response was observed. This means that the extent of the process zone spans over most of the crack surface. The rather long fracture process zone is related to a low tensile strength (*i.e.*, easy crack initiation) and high fracture energy. It is believed that most of the energy is dissipated through friction by aggregate bridging in the present case, since they are weakly bonded to the matrix after low temperature firing.

Acknowledgments

JAR thanks CNPq for the productivity scholarship, grant #307127/2013-3. RV's stay at LMT was supported through an RIA scholarship, grant #2017/20911-9, São Paulo Research Foundation (FAPESP).

References

[1] Lee WE, Vieira W, Zhang S, Ghanbari Ahari K, Sarpoolaky H, Parr C. Castable refractory concretes. International Materials Reviews 2001;46(3):145–67.

[2] Wachtman J. Materials and Equipment - Whitewares - Refractory Ceramics - Basic Science: Ceramic Engineering and Science Proceedings, Volume 16. No. 1 in Ceramic Engineering and Science Proceedings; Wiley; 2009. ISBN 9780470316306.

[3] Luz AP, Braulio MAL, Pandolfelli VC. Refractory Castable Engineering; vol. 1. 1 ed.; São Carlos, SP: Göller Verlag; 2015.

[4] Lee WE, Moore RE. Evolution of in situ refractories in the 20th century. Journal of the American Ceramic Society 1998;81(6):1385–410.

[5] Steinbrech RW. R-curve behavior of ceramics. In: Bradt R, Hasselman D, Munz D, Sakai M, Shevchenko V, editors. Fracture Mechanics of Ceramics; vol. 9 of Fracture Mechanics of Ceramics. Springer US. ISBN 978-1-4613-6477-1; 1992, p. 187–208.

[6] Launey ME, Ritchie RO. On the fracture toughness of advanced materials. Advanced Materials 2009;21(20):2103–10.

[7] Tschegg E. Prüfeinrichtung zur Ermittlung von bruchmechanishen Kennwerten sowie hiefür geeignete, Prüfkörper, Austrian Pat. AT 390328B, registered. 1986.

[8] Brühwiler E, Wittmann FH. The wedge splitting test, a new method of performing stable fracture mechanics tests. Engineering Fracture Mechanics 1990;35(1-3):117–25.

[9] Ribeiro S, Rodrigues JA. The influence of microstructure on the maximum load and fracture energy of refractory castables. Ceramics International 2010;36(1):263–74.

[10] Miyaji DY, Tonnesen T, Rodrigues JA. Fracture energy and thermal shock damage resistance of refractory castables containing eutectic aggregates. Ceramics International 2014;40(9, Part B):15227–39.

[11] Sutton MA, McNeill SR, Helm JD, Chao YJ. Advances in two-dimensional and three-dimensional computer vision. In: Photomechanics; vol. 77 of Topics in Applied Physics. 2000, p. 323–72.

[12] Sutton MA, Orteu JJ, Schreier H. Image correlation for shape, motion and deformation measurements: basic concepts, theory and applications. Springer Science & Business Media; 2009.

[13] Sutton MA. Computer vision-based, noncontacting deformation measurements in mechanics: A generational transformation. Applied Mechanics Reviews 2013;65(AMR-13-1009, 050802).

[14] Belrhiti Y, Pop O, Germaneau A, Doumalin P, Dupré JC, Harmuth H, et al. Investigation of the impact of micro-cracks on fracture behavior of magnesia products using wedge splitting test and digital image correlation. Journal of the European Ceramic Society 2015;35(2):823–9.

[15] Vargas R, Neggers J, Canto RB, Rodrigues JA, Hild F. Analysis of wedge splitting test on refractory castable via integrated DIC. Journal of the European Ceramic Society 2016;36(16):4309–17.

[16] Dai Y, Gruber D, Harmuth H. Observation and quantification of the fracture process zone for two magnesia refractories with different brittleness. Journal of the European Ceramic Society 2017;37(6):2521–9.

[17] Dai Y, Gruber D, Harmuth H. Determination of the fracture behaviour of MgO-refractories using multi-cycle wedge splitting test and digital image correlation. Journal of the European Ceramic Society 2017;37(15):5035–43.

[18] Dupré JC, Doumalin P, Belrhiti Y, Khlifi I, Pop O, Huger M. Detection of cracks in refractory materials by an enhanced digital image correlation technique. Journal of Materials Science 2018;53(2):977–93.

[19] Vargas R, Neggers J, Canto RB, Rodrigues JA, Hild F. Comparison of two full-field identification methods for the wedge splitting test on a refractory. Journal of the European Ceramic Society 2018;38(16):5569 –79.

[20] Hillerborg A, Modéer M, Petersson PE. Analysis of crack formation and crack growth in concrete by means of fracture mechanics and finite elements. Cement and Concrete Research 1976;6(6):773–82.

[21] Elices M, Guinea G, Gómez J, Planas J. The cohesive zone model: advantages, limitations and challenges. Engineering Fracture Mechanics 2002;69:137–63.

[22] Dugdale DS. Yielding of steel sheets containing slits. Journal of the Mechanics and Physics of Solids 1960;8(2):100 –4.

[23] Song SH, Paulino GH, Buttlar WG. Simulation of crack propagation in asphalt concrete using an intrinsic cohesive zone model. Journal of Engineering Mechanics 2006;132(11):1215–23.

[24] Aure T, Ioannides A. Simulation of crack propagation in concrete beams with cohesive elements in abaqus. Transportation Research Record: Journal of the Transportation Research Board 2010;(2154):12–21.

[25] Su X, Yang Z, Liu G. Finite Element Modelling of Complex 3D Static and Dynamic Crack Propagation by Embedding Cohesive Elements in Abaqus. Acta Mechanica Solida Sinica 2010;23(3):271 –82.

[26] Evangelista F, Roesler JR, Proença SP. Three-dimensional cohesive zone model for fracture of cementitious materials based on the thermodynamics of irreversible processes. Engineering Fracture Mechanics 2013;97:261–80.

[27] Shen B, Paulino GH. Identification of cohesive zone model and elastic parameters of fiber-reinforced cementitious composites using digital image correlation and a hybrid inverse technique. Cement and Concrete Composites 2011;33(5):572–85.

[28] Shen B, Paulino GH. Direct extraction of cohesive fracture properties from digital image correlation: a hybrid inverse technique. Experimental Mechanics 2011;51(2):143–63.

[29] Fedele R, Sessa S, Valoroso N. Image correlation-based identification of fracture parameters for structural adhesives. Technische Mechanik 2012;32(2):195–204.

[30] Alfano M, Lubineau G, Paulino GH. Global sensitivity analysis in the identification of cohesive models using full-field kinematic data. International Journal of Solids and Structures 2015;55:66–78.

[31] Blaysat B, Hoefnagels JPM, Lubineau G, Alfano M, Geers MGD. Interface debonding characterization by image correlation integrated with double cantilever beam kinematics. International Journal of Solids and Structures 2015;55:79–91.

[32] Affagard JS, Mathieu F, Guimard JM, Hild F. Identification method for the mixed mode interlaminar behavior of a thermoset composite using displacement field measurements and load data. Composites Part A: Applied Science and Manufacturing 2016;91:238–49.

[33] Ruybalid AP, Hoefnagels JPM, van der Sluis O, van Maris MPFHL, Geers MGD. Mixed-mode cohesive zone parameters from integrated digital image correlation on micrographs only. International Journal of Solids and Structures 2018;.

[34] Abanto-Bueno J, Lambros J. Experimental determination of cohesive failure properties of a photodegradable copolymer. Experimental Mechanics 2005;45(2):144–52.

[35] Ferreira M, Venturini W, Hild F. On the analysis of notched concrete beams: From measurement with digital image correlation to identification with boundary element method of a cohesive model. Engineering Fracture Mechanics 2011;78(1):71 – 84.

[36] Richefeu V, Chrysochoos A, Huon V, Monerie Y, Peyroux R, Wattrisse B. Toward local identification of cohesive zone models using digital image correlation. European Journal of Mechanics-A/Solids 2012;34:38–51.

[37] Rethore J, Estevez R. Identification of a cohesive zone model from digital images at the micron-scale. Journal of the Mechanics and Physics of Solids 2013;61(6):1407–20.

[38] Abaqus 6.14 Documentation. Dassault Systèmes Simulia Corp.; Providence, RI, USA.; 2014.

[39] Diógenes HJF, Cossolino LC, Pereira AHA, El Debs MK, El Debs ALHC. Determination of modulus of elasticity of concrete from the acoustic response. Revista IBRACON de Estruturas e Materiais 2011;4(5):803–13.

[40] Hild F, Bouterf A, Chamoin L, Leclerc H, Mathieu F, Neggers J, et al. Toward 4D mechanical correlation. Advanced Modeling and Simulation in Engineering Sciences 2016;3(1):17.

[41] Besnard G, Hild F, Roux S. "Finite-Element" displacement fields analysis from digital images: Application to Portevin-Le Chatelier bands. Experimental Mechanics 2006;46(6):789–803.

[42] Leclerc H, Périé J, Roux S, Hild F. Integrated digital image correlation for the identification of mechanical properties; vol. LNCS 5496. Berlin (Germany): Springer; 2009, p. 161–71.

[43] Geuzaine C, Remacle JF. Gmsh: A 3-D finite element mesh generator with built-in pre-and post-processing facilities. International Journal for Numerical Methods in Engineering 2009;79(11):1309–31.

[44] Hild F, Roux S. Comparison of local and global approaches to digital image correlation. Experimental Mechanics 2012;52(9):1503–19.

[45] Pagnacco E, Caro-Bretelle AS, Ienny P. Parameter Identification from Mechanical Field Measurements using Finite Element Model Updating Strategies; chap. 9. Wiley-Blackwell; 2012, p. 247–74.

[46] Maginador RV. Analysis of crack propagation in the Wedge Splitting Test via Digital Image Correlation and Finite Element Analyses. Master's thesis; Federal University of São Carlos (UFSCar) - Brazil; 2019.

[47] Park K, Paulino GH, Roesler JR. A unified potential-based cohesive model of mixed-mode fracture. Journal of the Mechanics and Physics of Solids 2009;57(6):891–908.

[48] Park K, Paulino GH. Computational implementation of the PPR potential-based cohesive model in ABAQUS: educational perspective. Engineering Fracture Mechanics 2012;93:239–62.

[49] Park K, Choi H, Paulino GH. Assessment of cohesive traction-separation relationships in ABAQUS: A comparative study. Mechanics Research Communications 2016;78:71–8.

[50] Fedele R, Raka B, Hild F, Roux S. Identification of adhesive properties in GLARE assemblies using digital image correlation. Journal of the Mechanics and Physics of Solids 2009;57(7):1003–16.

[51] Falk ML, Needleman A, Rice JR. A critical evaluation of cohesive zone models of dynamic fracture. In: Proceedings of the 5th European mechanics of materials conference on scale transitions from atomistics to continuum plasticity. 2001, p. 43–50.

[52] Davila C, Camanho P, de Moura M. Mixed-mode decohesion elements for analyses of progressive delamination. In: 19th AIAA Applied Aerodynamics Conference. 2001, p. 1486.

[53] Moës N, Belytschko T. Extended finite element method for cohesive crack growth. Engineering Fracture Mechanics 2002;69(7):813–33.

[54] Moslemi M, Khoshravan M. Cohesive zone parameters selection for mode-I prediction of interfacial delamination. Strojniski Vestnik/Journal of Mechanical Engineering 2015;61(9):507–16.

[55] Saucedo L, Rena CY, Ruiz G. Fully-developed FPZ length in quasi-brittle materials. International Journal of Fracture 2012;178(1-2):97–112.

[56] Dong W, Zhou X, Wu Z. On fracture process zone and crack extension resistance of concrete based on initial fracture toughness. Construction and Building Materials 2013;49:352–63.

[57] Pereira AHA, Miyaji DY, Cabrelon MD, Medeiros J, Rodrigues JA. A study about the contibution of the α-β phase transition of quartz to thermal cycle damage of a refractory used in fluidized catalytic cracking units. Cerâmica 2014;60:449–56.

Appendix A

The space-time history of the cohesive tractions for the back face is shown for the two analyzed cases in Figure 17. When $\alpha = 7$, the damaged zone is smaller and develops later on. At the end of the test, the extent of the damaged zones is similar in both cases.

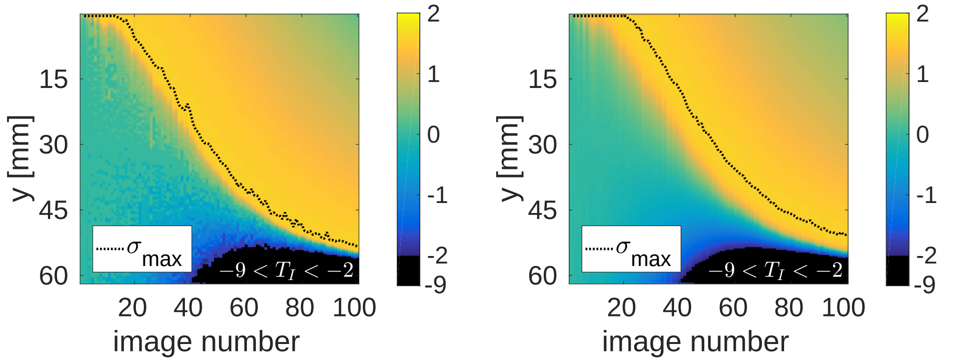

(a) (b)

Figure 17: Normal traction (expressed in MPa) history for the back face, with $\alpha = 2$ (a) and $\alpha = 7$ (b). The black dotted line shows the location for which the cohesive strength $\sigma_{\max}$ was reached.

The damage history for the back face is shown in Figure 18. Although the most damaged element reaches a level less than 0.9, most of the specimen is damaged at the end of the test. This observation applies in both cases.

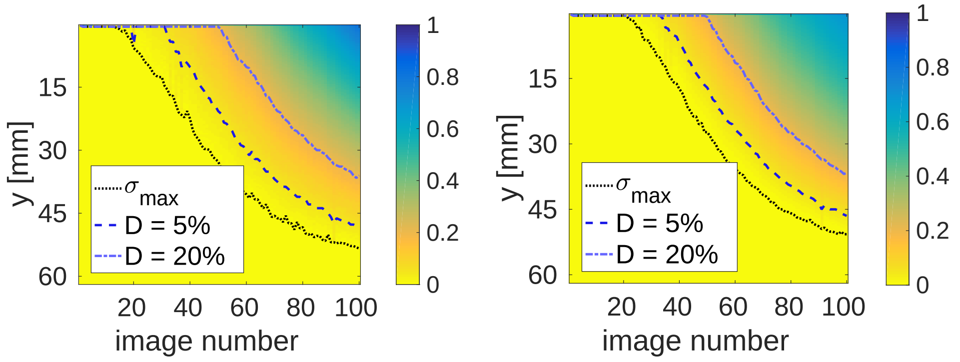

(a) (b)

Figure 18: Damage history for the back face with $\alpha = 2$ (a) and $\alpha = 7$ (b). The black dotted line shows the location for which the cohesive strength $\sigma_{\max}$ was reached.

The spacetime history of elementary dissipated energy for the back face is shown in Figure 19. The maximum level that can be reached is equal to J_c, but no element has achieved such dissipation in both cases.

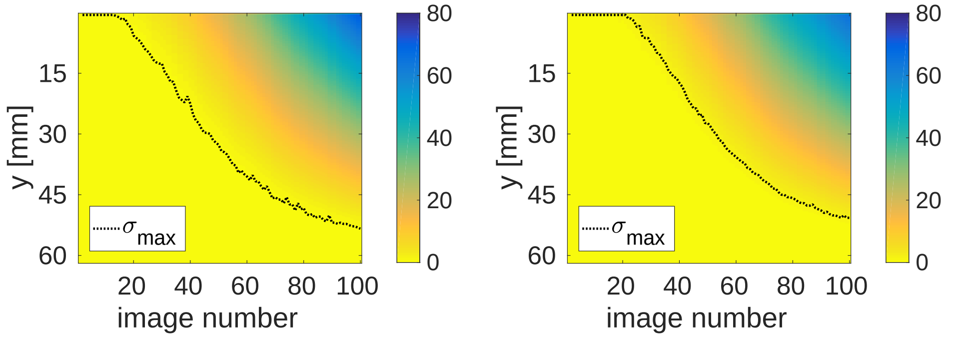

(a) (b)

Figure 19: Elementary dissipated energy (in J/m^2) history for the back face when $\alpha = 2$ (a) and $\alpha = 7$ (b). The black dotted line shows the location for which the cohesive strength $\sigma_{\max}$ was reached.